SUSPENDED CARBON NANOWIRE BIOSENSOR FOR RAPID AND LABEL-FREE *SALMONELLA* DETECTION

AUNG THIHA

FACULTY OF ENGINEERING
UNIVERSITY OF MALAYA
KUALA LUMPUR

2020

University of Malaya

SUSPENDED CARBON NANOWIRE BIOSENSOR FOR RAPID AND LABEL-FREE *SALMONELLA* DETECTION

AUNG THIHA

THESIS SUBMITTED IN FULFILMENT OF THE REQUIREMENTS FOR THE DEGREE OF DOCTOR OF PHILOSOPHY

FACULTY OF ENGINEERING
UNIVERSITY OF MALAYA
KUALA LUMPUR

2020

University of Malaya

UNIVERSITY OF MALAYA

ORIGINAL LITERARY WORK DECLARATION

Name of Candidate: AUNG THIHA

Matric No: KHA120138

Name of Degree: Doctor of Philosophy

Title of Thesis: SUSPENDED CARBON NANOWIRE BIOSENSOR FOR RAPID AND LABEL-FREE *SALMONELLA* DETECTION

Field of Study: BioMEMS

I do solemnly and sincerely declare that:

(1) I am the sole author/writer of this Work;
(2) This Work is original;
(3) Any use of any work in which copyright exists was done by way of fair dealing and for permitted purposes and any excerpt or extract from, or reference to or reproduction of any copyright work has been disclosed expressly and sufficiently and the title of the Work and its authorship have been acknowledged in this Work;
(4) I do not have any actual knowledge nor do I ought reasonably to know that the making of this work constitutes an infringement of any copyright work;
(5) I hereby assign all and every rights in the copyright to this Work to the University of Malaya ("UM"), who henceforth shall be owner of the copyright in this Work and that any reproduction or use in any form or by any means whatsoever is prohibited without the written consent of UM having been first had and obtained;
(6) I am fully aware that if in the course of making this Work I have infringed any copyright whether intentionally or otherwise, I may be subject to legal action or any other action as may be determined by UM.

Candidate's Signature Date:

Subscribed and solemnly declared before,

Witness's Signature Date:

Name:

Designation:

University of Malaya

SUSPENDED CARBON NANOWIRE BIOSENSOR FOR RAPID AND LABEL-FREE SALMONELLA DETECTION

ABSTRACT

Carbon, the building block life, is rapidly becoming the building block of next-generation electronics and sensor materials. Of many ways to handle nanocarbon materials, Carbon Microelectromechanical Systems (C-MEMS) emerges as a unique way for top-down fabrication of three-dimensional carbon micro to nanostructures. In this work, the use of C-MEMS techniques in nanowire biosensor fabrication is explored. Two main hindrances in the use of C-MEMS carbon structures for biosensing lie in miniaturization to nanoscale sensor material and inertness of as-fabricated carbon. This dissertation presents ways to overcome these limitations. First, miniaturization to patterned sub-100 nm carbon nanowires was achieved by optimization of electrospinning properties and integration of electrospinning photoresist polymer with photolithographic patterning. Secondly, a microplasma direct writing technique was developed as a novel non-destructive technique for selective surface functionalization of C-MEMS manufactured carbon electrodes. This method uses a simple setup to pattern carboxylic functional groups on the carbon surface at atmospheric conditions. Surface oxygen percentage as high as 27% has been observed. The fabricated suspended carbon nanowires were integrated with microfluidics and immobilized with biomolecular probes for biosensing. Nanowire biosensing was demonstrated by developing an aptamer-based assay that can detect whole-cell *Salmonella*. The carbon nanowire biosensor used chemiresistive biosensing to achieve rapid detection of the pathogen with high sensitivity and specificity with a detection limit of 10 CFU/mL, which is more sensitive than conventional methods of detecting bacteria.

University of Malaya

BIOSENSOR NANOWAYAR KARBON TERGANTUNG UNTUK PENGESANAN *SALMONELLA* YANG CEPAT DAN BEBAS LABEL

ABSTRAK

Karbon, salah satu unsur asas kehidupan, semakin diguna-pakai secara meluas sebagai bahan asas dalam pembangunan bahan sensor dan elektronik. Antara teknik-teknik yang sedia ada untuk menyediakan bahan nanokarbon, *Carbon Microelectromechanical Systems* (C-MEMS) adalah cara "*top-down*" yang unik untuk fabrikasi struktur tiga dimensi mikro- dan nanokarbon. Dalam disertasi ini, teknik pengunaan C-MEMS dalam fabrikasi pengesanbio dirungkaikan. Dua cabaran utama dalam pengunaan struktur karbon C-MEMS untuk *biosensor* adalah proses pengecilan bahan pengesan ke skala nano dan sifat karbon yang tidak reaktif. Disertasi ini juga membentangkan cara-cara untuk mengatasi cabaran-cabaran ini. Pertama, proses pengecilan kepada nanowayar karbon sub-100nm dicapai dengan mengintegrasikan *electrospun polymer photoresist* dengan pencorakan (*patterning*) menggunakan teknik fotolitografi. Cara kedua ialah melalui pembangunan alat penulisan-terus plasma (*direct plasma writing*) untuk pengfungsian permukaan elektrod karbon C-MEMS secara terpilih. Cara ini mengunakan plasma untuk menghasilkan corak kumpulan berfungsi karboksilik atas permukaan karbon. Nanowayar karbon yang dihasilkan diintegrasikan dengan perangkat mikrofluidik dan dilitupi dengan unsur biorekognisi untuk *biosensor*. Fungsi *biosensor* dibuktikan melalui pembangunan prosedur ujian aptamer untuk pengesanan sel Salmonella. *Biosensor* nanowayar karbon ini mengunakan kaedah *biosensor* secara elektrokimia untuk mencapai pengesanan pathogen dengan kepekaan yang tinggi dan pantas. *Biosensor* yang dibangunkan dapat mencapai had pengesanan sebanyak 10 CFU/mL, iaitu lebih peka berbanding dengan teknik pengesanan bakteria konvensional.

University of Malaya

ACKNOWLEDGEMENTS

This thesis is dedicated to my dear parents, Naing Win and Khin Hla Win for their unconditional love and support; to my beloved wife, Thinzar Oo who has been with me in every steps of this journey through good times and bad times; and to our daughter, Yumna who has given me a new meaning to life.

I would like to thank my advisor Prof. Fatimah Ibrahim for giving me opportunity to work on this exciting topic and for guiding me through this research. I want to thank Prof. Marc Madou for sharing his vast expertise and providing directions during this research. I want to thank Prof. Jongman Cho for teaching us how to make instruments from sketch.

Special thanks go to my friends, Karunan Joseph, Shah Mukim, Lina , Bashar, Mehdi, Julian and Shalini, without them this journey would have been much harder.

I would like to acknowledge Ministry of Science Technology and Innovation (MOSTI) Science Fund (SF-020-2014), Transdisciplinary Research Grant Scheme (TR002A-2014B), and University of Malaya Flagship Grant (FL001A-14AET) for providing funding for equipment and materials. I want to thank Department of Biomedical Engineering and University of Malaya for giving me opportunity and facilities to conduct this research.

University of Malaya

TABLE OF CONTENTS

University of Malaya

University of Malaya

University of Malaya

University of Malaya

University of Malaya

LIST OF FIGURES

University of Malaya

University of Malaya

University of Malaya

University of Malaya

University of Malaya

LIST OF TABLES

University of Malaya

LIST OF SYMBOLS AND ABBREVIATIONS

BS4	:	Tetrabutylammonium tetrafluoroborate
C-MEMS	:	Carbon-Microelectromechanical Systems
C-NEMS	:	Carbon Nanoelectromechanical Systems
CNT	:	Carbon nanotubes
DNA	:	Deoxyribonucleic acid
EBL	:	Electron beam lithography
EDS	:	Energy dispersive X-Ray spectroscopy
EMS	:	Electromechanical spinning
FESEM	:	Field emission scanning electron microscopy
FFES	:	Far-field electrospinning
FIB	:	Focused ion beam
LAMP	:	Loop-mediated isothermal amplification
MEMS	:	Microelectromechanical Systems
NFES	:	Near-field electrospinning
PMMA		Poly(methyl methacrylate)
PCR	:	Polymeric chain reaction
PEO	:	Polyethylene oxide
POC	:	Point-of-care
RNA	:	Ribonucleic Acid
S. Typhimurium	:	*Salmonella* Typhimurium
SEM	:	Scanning electron microscopy
SMU	:	Source measurement unit
XPS	:	X-ray photoelectron spectroscopy
XRD	:	X-ray powder diffraction

University of Malaya

CHAPTER 1: INTRODUCTION

1.1 Overview

Nanowire biosensors have become one of the most intensive research areas due to their extreme sensitivity derived from their one-dimensional electron transport properties. In this class of biosensors, nanowires form major sensing components and are usually coated by biological molecules such as DNA fragments, aptamer, and polypeptides, which act as transducer probes. As target molecules bind to transducer probes, they trigger changes in the electronic conductivity of nanowires due to their high surface-to-volume ratio and electron transport proprieties. Hence, target molecules capture-events can be easily detected in real-time by monitoring changes in conductivity. Currently, nanowires in electronic sensors are mainly fabricated by nanolithography techniques such as focused ion beam (Fujii, Sudoh, & Sakakihara, 2017) and electron beam lithography (Cui, Wei, Park, & Lieber, 2001; Juhasz, Elfström, & Linnros, 2005). While these techniques are capable of high-resolution patterns down to tens of nanometers, they are relatively expensive and slow for mass-manufacturing. The research presents the fabrication of highly defined suspended carbon nanowires by a simple electrospinning process combined with standard Carbon-Microelectromechanical Systems (C-MEMS) techniques for cost-effective, rapid, ultrasensitive, and label-free electronic biosensor application.

In this study, on-site suspended carbon nanowires were fabricated by the integration of electrospinning and photolithography. By electrospinning a photoresist polymer, the resulting mat can be photopatterned and crosslinked selectively in the desired area. Thus, electrospinning can be integrated with standard photolithography methods for suspended nanowire sensor fabrication. By converting the resulting electrospun photoresist nanowires to carbon by the C-MEMS fabrication, wafer-scale photo patternable fabrication of carbon nanowires can be achieved while pushing C-MEMS forward into

University of Malaya

nanodomain as Carbon Nanoelectromechanical Systems (C-NEMS). These polymers suspended nanowires undergo size reduction during pyrolysis in the C-MEMS process, reducing the diameter of electrospun photoresist fibers up to 70 percent. This shrinkage results in much thinner nanowires with a higher surface to volume ratio, making them more sensitive to electrical changes on the surface.

In biosensing applications, it is usually necessary to immobilize desired biomolecules on the carbon surface. The first step in biomolecules immobilization is the modification of the carbon electrode surface with hydroxyl (-OH) and carboxyl (-COOH) functional groups. Recently, Hirabayashi *et al.* have evaluated surface functionalization techniques of pyrolyzed carbon surfaces with various chemical and plasma treatments (Hirabayashi, Mehta, Khosla, & Kassegne, 2013; Hirabayashi, Mehta, W. Vahidi, Khosla, & Kassegne, 2013). However, the standard plasma treatment method results in the carboxylation of the whole area, not only the sensing component. Unlike conventional surface functionalization techniques, water microplasma direct writing, introduced in this study, enables site-selective mask-less functionalization of carbon surfaces at the microscale in atmospheric conditions. Hence, this technique was used for selective surface functionalization of carbon nanowire with carboxylic groups. The oxidation degree of SU-8 derived pyrolyzed carbon surfaces was measured in terms of their carbon to oxygen (C/O) ratios from Energy-dispersive X-ray spectroscopy (EDS) elemental mapping and X-ray photoelectron spectroscopy (XPS). The presence of carboxyl groups on plasma written surfaces was evaluated using XPS. The effects of surface functional groups on electrochemical characteristics were also investigated for the purpose of electrochemical bio-sensing applications.

After the functionalization of the carboxyl groups, sensing probes such as antigen/antibody probes or DNA/RNA nucleic acid probes can be immobilized via cross-

University of Malaya

linking with carboxyl molecules. In this research, aptamers were used as bio-transducer probes that bind with target membrane proteins of bacteria, capturing the bacteria in the process. The performance of the sensor platform was evaluated for the label-free detection of *Salmonella* Typhimurium (*S.* Typhimurium).

The rationale behind this work involves two main factors: (1) to develop a facile method for wafer-scale producing suspended carbon nanowire sensor by top-down fabrication technique that is compatible with conventional photolithography and wafer processing techniques (2) to investigate surface functional groups on as-produced carbon structures from C-MEMS and to develop suitable surface functionalization method for C-MEMS manufactured carbon electrodes. The C-MEMS fabrication of carbon nanowire sensors with aptamer probes for *Salmonella* detection has advantages in terms of higher sensitivity, potential lower-cost and simpler fabrication for mass-production, label-free detection, and whole-cell bacteria detection.

1.2 Objectives

The main objective of this research is to develop an all-carbon suspended carbon nanowire biosensor chip for chemiresistive *Salmonella* detection. Below are three sub-objectives:

I. To fabricate suspended carbon nanowires with C-MEMS and electrospinning techniques.
II. To investigate surface properties of C-MEMS manufactured carbon structures and to perform carboxyl surface functionalization.
III. To develop a chemiresistive *Salmonella* sensing assay using an aptamer-based carbon nanowire sensor.

University of Malaya

1.3 Scope of work

This research entails the development of carbon nanowire for biosensing. This research work focuses on top-down fabrication carbon, specifically, fabrication of carbon nanowires by C-MEMS and electrospinning techniques. Here, electrospinning parameters were optimized for the fabrication of sub-100 nm diameter nanowires. In addition, the investigation of carbon nanowire as a biosensor will be limited to aptamer-based bacterial sensing based on the chemiresistive sensing mechanism. In this work, bacterial sensing is demonstrated on *Salmonella* Typhimurium bacteria by immobilizing *Salmonella* specific aptamer probes on the nanowire.

1.4 Thesis Outline

This dissertation is organized into five chapters describing essential components of the thesis.

This chapter, Chapter 1, serves as a general introduction to the thesis explaining the rationale and objectives of the thesis while also outlining the structure of the thesis organization.

Chapter 2 introduces the background of this research work overviewing the C-MEMS technology, carbon nanowire fabrication methods, and applications of carbon nanowire as sensors. In particular, it focuses on the use of electrospinning for nanowire fabrication and history of suspended nanofiber fabrication in C-MEMS. Surface functionalization techniques for C-MEMS structures are also discussed for sensor applications. The chapter is then concluded with current and future applications for nanowire sensors with an emphasis on the detection of pathogenic bacteria.

Chapter 3 discusses research methods for sensor development. Experimental methods for nanowire fabrication and optimization are presented while exploring different electrospinning techniques and parameters to achieve thinnest and most uniform fibers possible from the photoresist polymer solution. C-MEMS processing steps and its

University of Malaya

integration with nanowire electrospinning are described in detail. Then, the functionalization of C-MEMS derived carbon structures were explored by various surface characterization methods. In particular, microplasma direct writing will be introduced as a new method for selective surface functionalization. Then, biofunctionalization and evaluation method of the biosensor in bacterial sensing are also outlined.

In Chapter 4, the characterization results of the various experiments are discussed. Electrospinning parameters and their effects on fiber morphology are explored. This chapter also describes the effect of C-MEMS pyrolysis on the thinning of nanowire and electrical and chemical characterization of pyrolyzed carbon nanowires. Surface properties of as-pyrolyzed and functionalized carbon structures characterized by various investigations were discussed. Then, functionalized nanowire microchips were demonstrated and evaluated as a biosensor in detection of whole-cell *Salmonella* Typhimurium.

Chapter 5 serves as a conclusion to the thesis while exploring future works on the subject.

University of Malaya

CHAPTER 2: LITERATURE REVIEW

2.1 Background

Carbon, the building block life, is now poised to become the building block of next-generation electronics. Carbon nanomaterials such as graphene and carbon nanotubes (CNT) offer superior electrical, thermal, and mechanical properties as well as energy efficiency than current silicon-based electronics (Peng, Zhang, & Wang, 2014; Shulaker et al., 2013). Furthermore, their fast electron transfer kinetics, excellent conductivity, and ease of biofunctionalization give rise to numerous sensor applications (M. M. Barsan, Ghica, & Brett, 2015; Hernández et al., 2014; Qiu et al., 2015). However, these two allotropes of carbon, graphene, and CNTs, are hard to handle and heterogeneous (Yang et al., 2010). Moreover, they are difficult to fabricate into any desired shapes, for instance, a suspended nanowire for electronic sensors. Graphene and CNT based bio transistor sensors have been synthesized by chemical vapor deposition or chemical reduction methods, which are still hard to integrate with established large-scale manufacturing techniques for electronics (Akinwande et al., 2019; Peng, Zhang, & Qiu, 2019). Currently, nanowires in electronic sensors are mainly fabricated by focused ion beam (Fujii et al., 2017) and electron beam lithography (Cui et al., 2001; Juhasz et al., 2005). While these techniques are capable of high-resolution patterns down to tens of nanometers, they are relatively expensive and slow for mass-manufacturing. In this report, highly defined suspended carbon nanowires were fabricated by a simple electrospinning process combined with standard Carbon-Microelectromechanical Systems (C-MEMS) techniques for rapid, ultrasensitive, label-free electronic biosensor application.

C-MEMS offers a way to control fabrication of carbon materials in desired shapes from macro to nanoscale dimensions. A typical C-MEMS fabrication involves patterning polymer structures and subsequent carbonization to convert them into carbon structures.

University of Malaya

Patterning can be performed by standard photolithography techniques on photosensitive polymers with high carbon content. SU-8 photoresist is a typical polymer used in C-MEMS because they are patternable to high aspect ratio and 3-dimensional structures (Martinez-Duarte, 2014). Carbonization is performed by pyrolysis of patterned polymer structures in an inert atmosphere at an elevated temperature ranging from 800 to 1200 °C. This process converts polymer patterns to conductive carbon while retaining their shape. Carbon structures obtained from this technique have glassy carbon like properties (Martinez-Duarte, 2014) and have glassy carbon like microstructures consisting of graphene fragments in various folding arrangements(S. Sharma, Shyam Kumar, Korvink, & Kübel, 2018). Glassy carbon is a widely used electrode material for electrochemical analysis because of its inert nature, stability and wide electrochemical windows (Bollella, Gorton, Ludwig, & Antiochia, 2017). Using C-MEMS fabrication techniques, researchers have fabricated high aspect ratio carbon micro 3D electrodes for various applications. These include next-generation battery electrodes (Long, Dunn, Rolison, & White, 2004), electrochemical sensors (Kamath & Madou, 2014), gas sensors (S. Sharma & Madou, 2012) and glucose sensors (Y. Wu, Lin, & Zhang, 2013).

While photolithography in C-MEMS offers a way to fabricate high aspect ratio microstructures, electrospinning provides a simple and cost-effective way to fabricate nanostructures. In electrospinning, a high voltage is applied between syringe tip and collector. The electric field stretches polymer droplet to nanoscale as it ejects from syringe tip towards collector and deposits as a nanofiber mat. Electrospinning has been very widely explored in a variety of applications such as filtrations (Gopal et al., 2006), tissue engineering scaffolds (W. J. Li, Laurencin, Caterson, Tuan, & Ko, 2002) to polymer field-effect transistors (FET) (Babel, Li, Xia, & Jenekhe, 2005; Manuelli, Persano, & Pisignano, 2014). However, a major obstacle of integrating electrospinning into electronics and sensor fabrication is that electrospinning inherently is a random

University of Malaya

process. Thus, improving control of the electrospinning process, with the focus on positioning single nanowires and integrating with support structures, is an active research area. Recently, Prakash et al. electrospun multi-walled carbon nanotubes (MWCNT) embedded SU-8 polymer fibers on micro copper poles for biosensing (Prakash, Vanjari, Sharma, & Singh, 2016). The authors reported controlling electrospinning time for the deposition of a single fiber on the support structure. This way of controlling, however, tends to require mostly manual observation of resultant fibers (S. Sharma, Sharma, Cho, & Madou, 2012). In a more recent study, Paul et al. have reported the deposition of electrospun MWCNTs-zinc oxide nanofibers as stretchable biosensors deposited between gold electrodes (Paul K, Panigrahi, Singh, & Singh, 2017). Fibers were fabricated by electrospinning and fiber mats were collected by dissolving in a solvent and subsequent drop-casting of the solution on support structures.

In this study, the suspended carbon nanowire sensor chips were fabricated by the integration of electrospinning and photolithography. Support structures were fabricated by the C-MEMS process and electrospinning was used to deposit fiber mats on the silicon wafer. Second step photolithography was used to selectively crosslink carbon nanowires on the support structures. By converting the resulting electrospun photoresist nanowires to carbon by the C-MEMS fabrication, carbon nanowires can be produced at defined sites. This combination of C-MEMS and electrospinning techniques can advance low-cost wafer-scale fabrication carbon nanostructures as sensors.

2.2 Carbon-Micro Electromechanical Systems

Microelectromechanical Systems (MEMS) are device systems that have microscale mechanical and electromechanical components. MEMS devices are generally fabricated by semiconductor device manufacturing technology, such as photolithography, physical and chemical deposition. They have been widely used as microsensors, microactuators,

University of Malaya

and microelectronics components. MEMS devices can be seen in a large variety of consumer applications from accelerometers in smartphones to inkjet printer nozzles.

Carbon microelectromechanical system (C-MEMS) is defined as both a set of fabrication methods used in making carbon microstructures from pre-patterned precursor polymers and the resulting carbon based microdevices (Martinez-Duarte, 2014). As carbon has become a material of choice for next-generation mechanical and electronic applications lead by wonder materials such as graphene and carbon nanotubes, C-MEMS offers a way to realize a scalable manufacturing of carbon based micro/nano components. The C-MEMS process takes advantage of the easy fabrication of polymer structures and convert them into carbon structures by pyrolysis. The micro and nano polymer precursor structures can be fabricated by a large variety of methods including photolithography, electrospinning, electron beam lithography, focused ion beam lithography and nano imprint lithography.

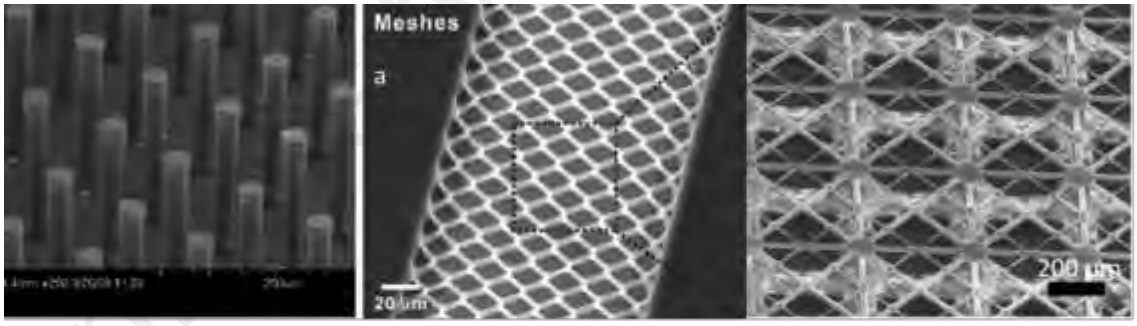

Figure 2.1: Examples of the C-MEMS structures (a) Micropillars for 3D battery electrodes (Chunlei Wang et al., 2004) (b) Suspended carbon meshes for sensors (Y. Lim, J. Heo, M. J. Madou, & H. Shin, 2013) (c) Multilayer suspended carbon structures (Tan et al., 2018).

The first-ever fabrication of carbon microstructures by pyrolysis was reported by Schueller *et al.* in 1997 (Schueller, Brittain, & Whitesides, 1997). In their study, precursor polymer structures were fabricated by micro-molding and then pyrolyzed to form carbon microstructures. These microstructures were used as components in MEMS

University of Malaya

microreactors. Photolithographic patterning of precursor polymer was reported shortly after this research to fabricate carbon films for electrochemical electrodes to be used in batteries, sensors, and capacitors (Kim, Song, Kinoshita, Madou, & White, 1998; Ranganathan, Mccreery, Majji, & Madou, 2000). Singh *et al.* first fabricated C-MEMS structures by the pyrolysis of photo-patterned epoxy based negative photoresists (SU-8 and polyimide) on silicon wafers (Singh, Jayaram, Madou, & Akbar, 2002). Since then, a variety of complex C-MEMS structures have been fabricated, from micropillars to suspended carbon beams and resonators (Heo, Lim, Madou, & Shin, 2012; Chunlei Wang & Madou, 2005).

2.2.1 C-MEMS fabrication

The standard MEMS technology uses photolithography of photoresist polymers to define the structures of metal and semiconductor materials. But in C-MEMS, patterned photoresist polymer is converted to carbon by pyrolysis to achieve micro carbon structures. Hence, a standard C-MEMS fabrication starts with SU-8 photolithography and followed by carbonization. SU-8 photolithography generally involves the following processing steps: photoresist deposition, soft bake, exposure, post-exposure bake, and development.

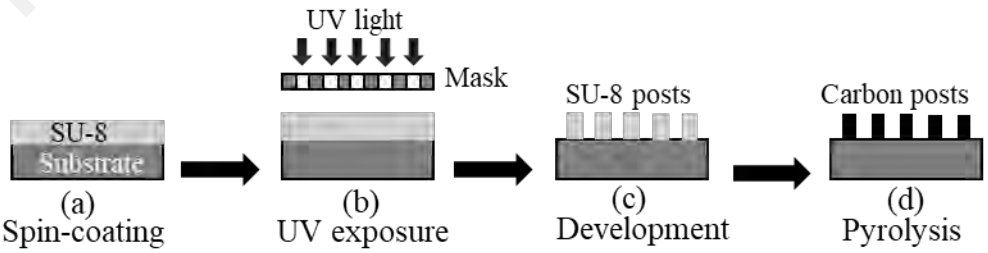

Figure 2.2: Typical process for fabricating carbon-based MEMS microstructures. (a) Spin-coating of SU-8 photoresist. (b) Patterning the photoresist structures by UV exposure. (c) Development of SU-8 structures. (d) Pyrolyzing the photoresist structures and converting to carbon.

University of Malaya

SU-8 is an epoxy-based, near-UV, negative photoresist developed by IBM for micromachining. It is composed of SU-8 resin dissolved in an organic solvent such as gamma-butyrolactone or cyclopentanone. The SU-8 2000 series used in this research uses cyclopentanone as the solvent. The ratio of SU-8 to solvent determines the viscosity and the range of thicknesses that can be manufactured, which can range from sub micrometers to thousands of micrometers. The photoresist also consists of triarylsulfonium salt that acts as a photoinitiator for SU-8 crosslinking. Figure 2.3 shows the crosslinking process of the SU-8 photoresist presented by researchers at IBM, the developer of SU-8 (Teh, Duerig, Drechsler, Smith, & Guentherodt, 2005). Triarlsulfonium salt absorbs the UV light and generates acid which then opens the epoxy bonds of SU-8 monomers. Opened epoxy bonds undergo chain propagating crosslinking reaction, as shown in Figure 2.3 (d). The end result is a high degree of crosslinked SU-8 network that retains UV exposed design and has high chemical and thermal resistances.

The crosslinked SU-8 structures are converted to carbon structures when pyrolyzed in an inert atmosphere (such as nitrogen, argon, forming gas) at high temperature in a controlled heating rate. Wang et al. reported complex chemical processes involved in converting polymer photoresist to carbon during the pyrolysis (Chunlei Wang, Zaouk, & Madou, 2006). This process includes degassing and multistage decomposition. The degassing process mainly occurs at temperatures below 600 °C (B. Y. Park, Taherabadi, Wang, Zoval, & Madou, 2005). Upon decomposition, epoxylated resins like SU-8 produces mostly phenolic compounds (such as phenol, cresols, isopropylphenol, isopropenylphenol, and bisphenol-A) (Chunlei Wang et al., 2006). At a temperature higher than 450 °C, carbon oxides and water vapor are released and solid carbon starts forming. When the temperature is about 800 °C, ring scission starts to occur and methane

University of Malaya

and more carbon oxides are released. At 900–1000 °C almost all the hydrocarbon will be completely decomposed into hydrogen and carbon (Chunlei Wang et al., 2006).

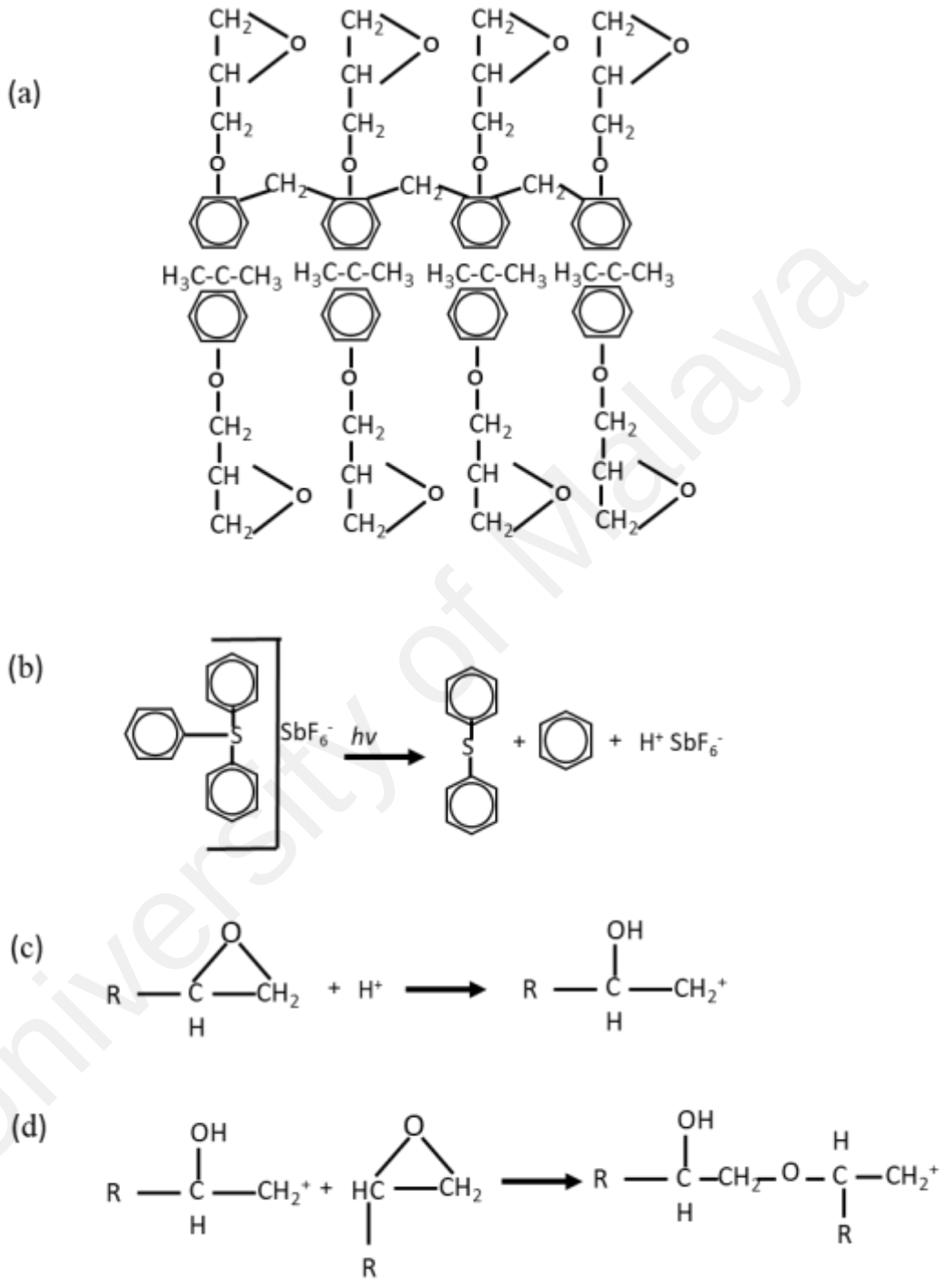

Figure 2.3: Crosslinking of SU-8: (a) Non crosslinked SU-8 monomer. (b) Generation of photoacid upon UV exposure due to protolysis of triarylsulfonium hexafluorantimonium, the cationic photoinitiator. (c) Initiation of polymerization via ring opening of the epoxy group. (d) Chain propagation of the crosslinking process. Adapted from(Teh, Duerig, Drechsler, Smith, & Guentherodt, 2005).

University of Malaya

More recently, evolution of carbon microstructures during pyrolysis was studied using high resolution transmission electron microscopy in carbon nanofibers (S. Sharma et al., 2018). Graphene fragments form during pyrolysis and they will either fold in fullerene-like structures or organized into multilayered graphene fragments. During the pyrolysis, tensile stress between the photoresist and substrate adhesion developed due to their different thermal expansion characteristics and shrinking of photoresist structures due to decomposition. This can lead to failures such as cracking of carbon structures and peeling-off i.e. total failure of adhesion between carbon and substrate. Hence, the temperature control during pyrolysis is important for the success of Carbon MEMS fabrication. Also, different structural heights and width of the photoresist structures and different photoresist compositions result in different shrinkage during pyrolysis. Negative photoresist (such as SU-8 photoresist) structures have vertical shrinkage of less than 30% (Chunlei Wang, Jia, Taherabadi, & Madou, 2005) with varying literal shrinkage depending on height. The adhesion between photoresist structures and substrates can be enhanced by a controlling post-bake process, increasing de-gassing time, and multistep pyrolysis process.

2.2.2 C-MEMS to C-NEMS: fabrication of suspended nanowires

The first SU-8 derived suspended carbon nanowires were fabricated by Chunlei Wang et al. in 2005 using standard UV photolithography and pyrolysis by carefully adjusting the SU-8 composition, exposure and development parameters (Chunlei Wang et al., 2005). The same group further improved the feature size of the suspended carbon nanofibers by incorporating electron beam lithography (EBL) writing on UV patterned carbon posts (Malladi, Wang, & Madou, 2006). They reported the sub-micron suspended carbon nanowires with a feature size of 500 nm while noting the difficulty in controlling resolution. Independently, EBL was also used to fabricate carbon nanowires with 50 to

University of Malaya

100 nm diameters using an ultrathin SU-8 layer (Du, Ssenyange, Aktary, & McDermott, 2009).

Sharma *et al.* pioneered an alternative approach of suspended carbon nanofiber fabrication by incorporating electrospinning. They fabricated carbon nanofibers with diameters down to 200 nm by electrospinning carbon precursors on micropillars made of organic xerogel (C. S. Sharma, Katepalli, Sharma, & Madou, 2011). This far-field electrospinning based approach was improved by using a rotating drum collector to fabricate 42 nm diameter carbon nanowires (S. Sharma et al., 2012). The researchers fabricated support structures through the standard C-MEMS process, and each chip with support structures was attached to a rotating drum collector. This electrospun fiber collection method dramatically improves mechanical stretching and the resultant fibers were found to be more graphitic with higher electrical conductivity while reducing wire diameters to sub-100 nm domain.

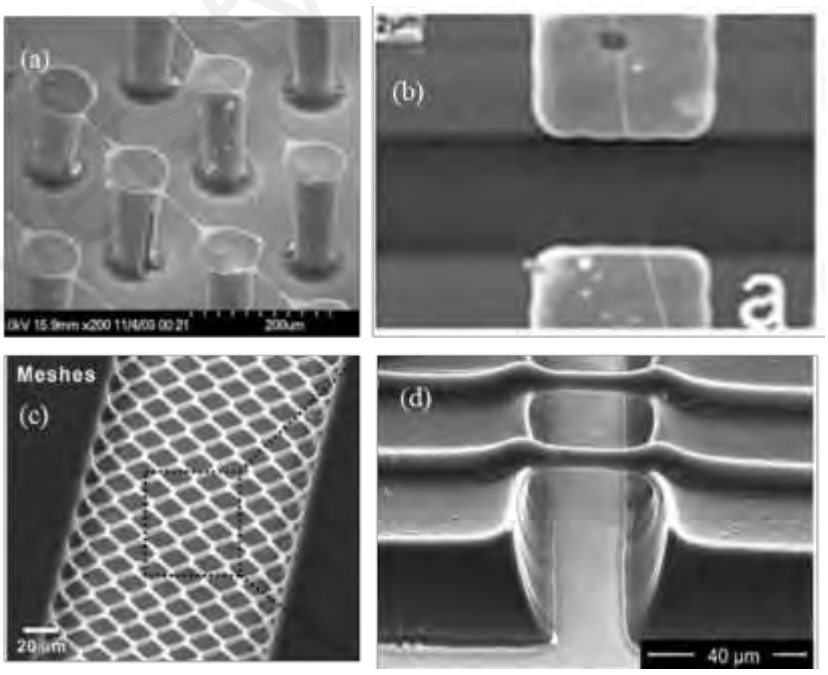

Figure 2.4: Suspended carbon structures fabricated by (a) standard photolithography (Chunlei Wang et al., 2005), (b) far-field electrospinning (C. S. Sharma et al., 2011), (c) two-step photolithography (Heo et al., 2012), and (d) electromechanical spinning (Giulia Canton, 2014).

University of Malaya

Due to hard to control nature of far-field electrospinning depositions, Canton *et al.* have invented an electro-mechanical spinning (EMS) method for precision deposition of SU-8 fibers across photolithographic-defined SU-8 structures (Giulia Canton, 2014). This approach enables patterning of the carbon nanowires at desired locations. The thinnest reported carbon fibers deposited by the electro-mechanical spinning have diameters of 200 nm (Giulia Canton, 2014). More recently, two-photon polymerization of SU-8 was used in fabricating suspended carbon nanofibers in C-MEMS (Cardenas-Benitez et al., 2019). Using femtosecond two-photon absorption, researchers successfully pattern suspended microwire with width in the range of 1250–1800 nm, which were then reduced to 300–550 nm suspended carbon structures through pyrolysis (Cardenas-Benitez et al., 2019).

Table 2.1: Suspended carbon nanowire produced by C-MEMS process and their diameters

Fabrication method	Carbon nanofiber diameter	Reference
Electron beam lithography of SU-8	50-100 nm	Du, Ssenyange, Aktary, & McDermott, 2009
Far-field electrospinning of SU-8/ PAN	198 nm	C. S. Sharma et al., 2011
Far-field electrospinning with rotating drum collector	42 nm	S. Sharma et al., 2012
Near field electrospinning of SU-8	200 nm	Giulia Canton, 2014
Two-photon lithography	300–550 nm	Cardenas-Benitez et al., 2019

2.3 Electrospinning

Electrospinning has been established as a simple, versatile and cost-effective method to fabricate polymer nanowires. In electrospinning, polymer fibers with micro to nanometre dimensions are electrically drawn from polymer solution through the syringe nozzle. A typical electrospinning setup includes a syringe pump, a conductive needle

University of Malaya

nozzle, a conductive collector substrate, and a power source to supply high voltage between needle and substrate, as demonstrated in Figure 2.5.

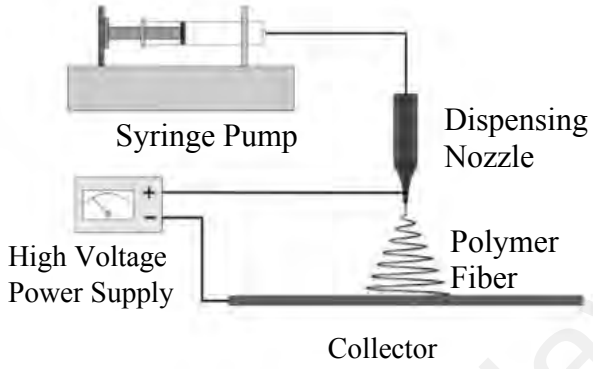

Figure 2.5: Schematic of an electrospinning setup.

Hence, a basic electrospinning system can be set up relatively cheap compared to other nanowire fabrication methods such as electron beam lithography, dip-pen lithography and chemically growth methods. Electrospinning has been employed in various polymers and polymer composites for specific applications. Currently, electrospinning is already widely in use for the fabrication of nanowire mats in applications such as filters and fabrics. This conventional electrospinning can be termed far-field electrospinning (FFES) as it applies the far-field region of polymer jet. However, this method has limited control over the patterning of nanowires. Improving precision controlling and patterning of nanowires leads to the development of near field electrospinning (NFES) and electromechanical spinning (EMS).

In a far field electrospinning setup, a high DC voltage of 10-20kV is applied between the nozzle and substrate which are physically separated by 10-15cm distance. Fibers of diameters ranging from tens to hundreds of nanometers have been fabricated in this scheme. Polymer droplet at the nozzle will form Taylor cone because of electrostatic forces. At high voltage, electrical charge will overcome polymer surface tension and a

University of Malaya

thin polymer jet will be discharged. This polymer jet undergoes a whipping motion due to electrostatic charges repealing in the jet. This motion causes thinning of polymer jet and solvent evaporation resulting in solidified polymer nanowires. Because of the whipping process, the far-field electrospinning is hard to control and fibers are randomly deposited on the collector substrate as a nanowire mat. Nonetheless, there have been efforts to align nanofibers obtained for far-field electrospinning. Rotating drum collector, for example, mechanically strengthen and align deposited fibers (S. Sharma et al., 2012). Alignment of fibers has also been demonstrated by using auxiliary electrodes (Stankus, Guan, & Wagner, 2004; Viswanadam & Chase, 2013) and using AC potentials instead of conventional DC electric field (Kessick, Fenn, & Tepper, 2004).

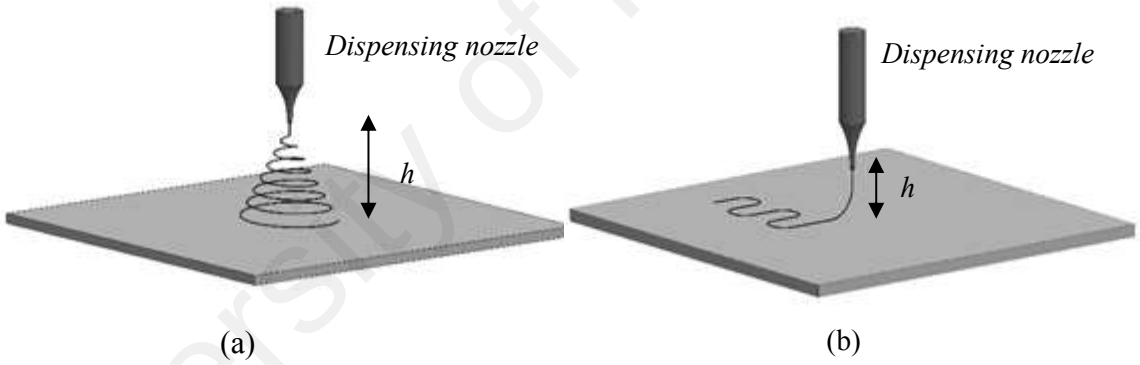

Figure 2.6: (a) Far Field of electrospinning where needle to collector distance h is 10-15cm (b) near-field electrospinning and electromechanical spinning where the distance h is less than 5mm.

Even with these techniques, far-field electrospinning fails to deliver precise and continuous patterning of nanofibers. Near-field electrospinning improves patterning capability by bringing the nozzle close to the substrate, and thus reducing the whipping moment during the flight of polymer jet (Sun, Chang, Li, & Lin, 2006). In that study, the near field electrospinning was performed voltage as low as 600V, and polymer fibers of diameters ranging from 50−150 nm have been achieved with viscoelastic polymer ink of polyethylene oxide.

University of Malaya

Electromechanical spinning is a further improvement upon near field electrospinning by adding mechanical movement of the collector stage. This mechanical pulling of polymer fiber added a new dimension in electrospinning resulting in thinner wires (G. Bisht et al., 2011; G. Bisht, Nesterenko, Kulinsky, & Madou, 2012; G. S. Bisht, Canton, Madou, Mirsepassi, & Dunn-rankin, 2012; G. S. Bisht et al., 2011). Electromechanical spinning can be performed by voltage as low as 200 V and polymer wires in sub 20 nm range have been obtained by this method when polyethylene oxide is used as polymer ink. However, in both near-field and electromechanical spinning, polymer jet cannot initiate itself because the use of low voltage decreases electric forces to overcome the surface tension. Hence, artificial disturbance of surface tension is required to initiate the polymer jet release from the nozzle. Control patterning of nanowires with electromechanical spinning would allow the creation of nanoscale polymer structures at very high resolution. Hence, it can be applied in conjunction with lithography methods to integrate novel nanostructures in microelectronics and MEMS.

2.3.1 Fundamentals of Electrospinning

Although electrospinning is a simple process to obtain nanowires with minimal equipment setup, the science behind electrospinning is far from being comprehended completely. It involves the understanding of electrostatics, electrohydrodynamics and fluid rheology. This section will explore the current theoretical understanding and modeling of polymer jet behavior during electrospinning.

As shown in Figure 2.5, a simple electrospinning system can be set up by four key components:

i. A conductive dispensing needle (also called spinneret or nozzle);
ii. A syringe pump with a controllable flow rate to supply the polymer to the needle;
iii. A high-voltage generator to supply voltage potential to the needle.

University of Malaya

iv. A conductive substrate as a grounded collector for electrospun fibers

In this setup, a polymer solution is fed to the needle by the syringe pump with a low flowrate, and it will form the droplet at the tip of the needle. When a high-voltage is provided between the needle and grounded collector, the droplet will deform from spherical to conical shape due to electrostatic forces on the surface of the droplet. At a certain high voltage and high enough molecular weight and viscosity (parameters that will be discussed later), a polymer jet is issued from the droplet. This jet flows away from the needle initially in straight movement and at a certain distance, bending instabilities will cause the jet into whipping movement. The initial section can be termed as near field regime region and the whipping section can be termed far field regime region (Giulia Canton, 2014).

2.3.1.1 Stages of far-field electrospinning process

Andrady A.L presented the key stages of the polymer jet in electrospinning process as (a) Droplet formation, (b) Taylor cone formation, (c) Launching of the jet, (d) Elongation of straight segment, (e) Whipping instability, and (f) Solidification into nanofiber (Andrady, 2008).

(a) ***Droplet formation***

Droplet formation is the first step towards nanofiber formation in the electrospinning process. When the polymer solution is pumped to the needle at a low flowrate, a droplet will form at the tip of the needle. In the absence of the electric field, the only two forces acting on the droplet are gravitational force (F_G) upon polymer and surface tension of the droplet (γ). For the solution of low viscosity, surface tension is not high enough to hold the droplet and it will drop off under the influence of gravity. Also, at the higher flowrate through the needle, droplets by will merge and continuous flow will be formed. However, at very low flowrate and at the equilibrium of gravitational and surface tension forces, the

University of Malaya

droplet will assume a spherical shape with radius r_0 for the needle tip radius of R (Andrady, 2008)

$$r_0 = (3R\gamma/2\rho g)^{1/3}, \tag{2.1}$$

where ρ is the density of solution and g is gravitational constant.

When the electric field is applied to the needle, electric force (F_E) and gravitational force will act against surface tension and sustainable droplet size at the needle tip become smaller. The electric field causes the ionization of the solution in which the positive and negative ions in the polymer solution are moving in opposite directions. For the positively charged needle, positive electric charges will move to the surface of the droplet and negative charges will move towards the interior. The electric charges on the surface act against surface tension and for the stability of the droplet, inward surface tension must exceed the outward electrostatic repulsion forces between surface charges (Andrady, 2008).

$$F_E \leq g\rho\left[\left(\frac{r^2}{\beta}\right) - V\right], \tag{2.2}$$

where F_E is electric force, ρ is the density of solution and g is gravitational constant, r is radius of the droplet, β is shape factor of droplet and V is volume of the droplet.

Electric force F_E in the system of voltage V held at the needle to collector distance L has been developed as in equation 3.3 (Andrady, 2008; Bugarski, Amsden, Goosen, Neufeld, & Poncelet, 1994; DeShon & Carson, 1968).

$$F_E = (4\pi\varepsilon V^2)/\left[ln\left(\frac{4L}{R}\right)^2\right], \tag{2.3}$$

where ε is the permittivity of the medium which in most cases is air and R is the radius of the needle tip.

University of Malaya

With increasing voltage potential, exceeding electric force will deform the droplet for increased surface area for electric charges. For the polymer solution with low molecular weight, this will cause electrospraying in which droplet degenerates into smaller droplets for increased surface area. However, for the polymer solution with sufficient molecular weight and viscosity, polymer chain entanglements will prevent breaking up and instead stretch into polymer jet.

(b) ***Taylor cone formation***

Surface electric charges cause the polymer droplet to elongate and will result in a characteristic conical shape called Taylor's cone. At a critical voltage V_C, a polymer jet is issued from the cone as electric forces overcome surface tension (Taylor, 1964, 1969).

$$V_C^2 = \left(\frac{2L}{h}\right)^2 \left(\ln\left(\frac{2h}{R}\right) - 1.5\right)(0.117\pi RT), \qquad (2.4)$$

where h and R are length and inner diameter of the needle respectively.

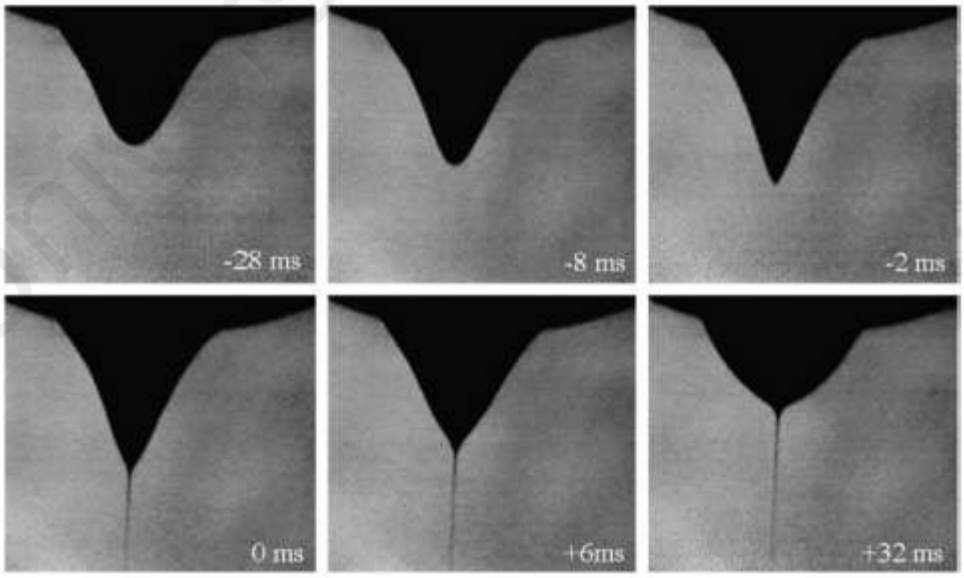

Figure 2.7: Taylor cone formation and polymer jet discharge during electrospinning process. Adapted from (Darrell H. Reneker & Yarin, 2008)

University of Malaya

(c) ***Launching of the jet***

As the electric force and surface charges stretch the droplet to increase the surface area resulting in Taylor cone as shown in Figure 2.7, the polymer chain entanglement in the concentrated polymer solution prevents the droplet from breaking up. Instead, the surface area is increased by stretching which results in a polymer fiber jet. The mass and charge in the system are conserved as polymer jet leaving the droplet (Andrady, 2008; Hohman, Shin, Rutledge, & Brenner, 2001).

(d) ***Elongation of the straight segment***

As the jet leaves the droplet, the external electric field and the columbic repulsion of surface charges cause the jet to elongate in a straight passage towards the collector (Darrell H. Reneker & Yarin, 2008). Those forces are counteracted by viscoelastic forces within the polymer solution. The jet diameter decreases due to elongation as well as evaporation of the solvent in polymer jet. The elongation of polymer jet during electrospinning has been modeled by several groups (Feng, 2002, 2003; Darrell H Reneker, Yarin, Fong, & Koombhongse, 2000).

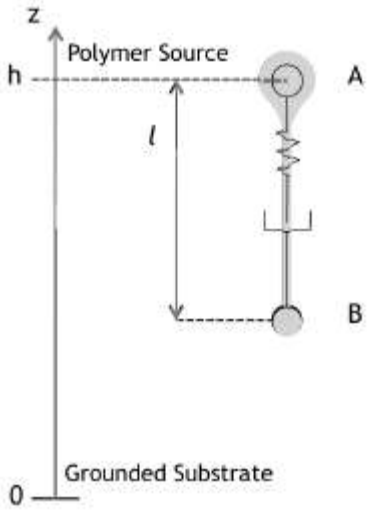

Figure 2.8: Model of a rectilinear segment of the electrospinning jet represented as a viscoelastic dumbbell. Adapted from (Giulia Canton, 2014).

University of Malaya

In the model developed by Reneker *et al.*, polymer jet emerging from the needle is divided into segments and each segment is considered as charge bead for computation. Beads are connected to each other in terms of the viscoelastic dumbbell as shown in Figure 2.8.

Equation 2.5 describes the momentum (v) balance of the bead being stretched by the external electric field and the Coulombic repulsion force while viscoelastic forces are counteracting them.

$$\mathrm{m}\frac{dv}{dt} = \frac{e}{l^2} - \frac{eV_0}{h} + \pi a^2 \sigma \qquad (2.5)$$

where m is mass of the bead, e is electrical charge, V_0 is applied voltage, l is distance between beads, h is distance between bead A to ground and a is radius of the bead.

(e) ***Whipping instability***

This polymer jet moves toward the grounded collector as a relatively linear straight line. Then inherent electrostatic instabilities cause the jet into whipping movement. During this movement, the fiber becomes thinner as the solvent evaporates and the jet is mechanically stretched. There have been several studies that try to model the complex whipping motion of polymer during the electrospinning process (Feng, 2002; Hohman et al., 2001; Ramakrishna, Fujihara, Teo, Lim, & Ma, 2005; Darrell H Reneker et al., 2000). In modeling, various forces acting on polymer jet during the flight and whipping process have to be considered. These forces are described below (Andrady, 2008; Wannatong, Sirivat, & Supaphol, 2004).

1. Gravitational force F_G which is dependent on the density of the solution. The force acts vertically downwards towards the collector
2. The electrostatic force F_E, which stretches the polymer jet towards the collector. The force is produced by the applied electric field.

University of Malaya

3. Columbic repulsion forces F_C on the surface of the jet, which introduce bending instability and whipping motions. It depends on the electrical characteristics of the polymer and its solvent.

4. Viscoelastic forces, which act against stretching of the jet. The force is dependent on the polymer molecular weight, the solvent, and the type of polymer.

5. Surface tension forces, which act against the stretching of the jet. These forces depend on polymer solution, solvent type and any additives such as a surfactant.

6. Frictional forces between the surface of the jet and the surrounding medium.

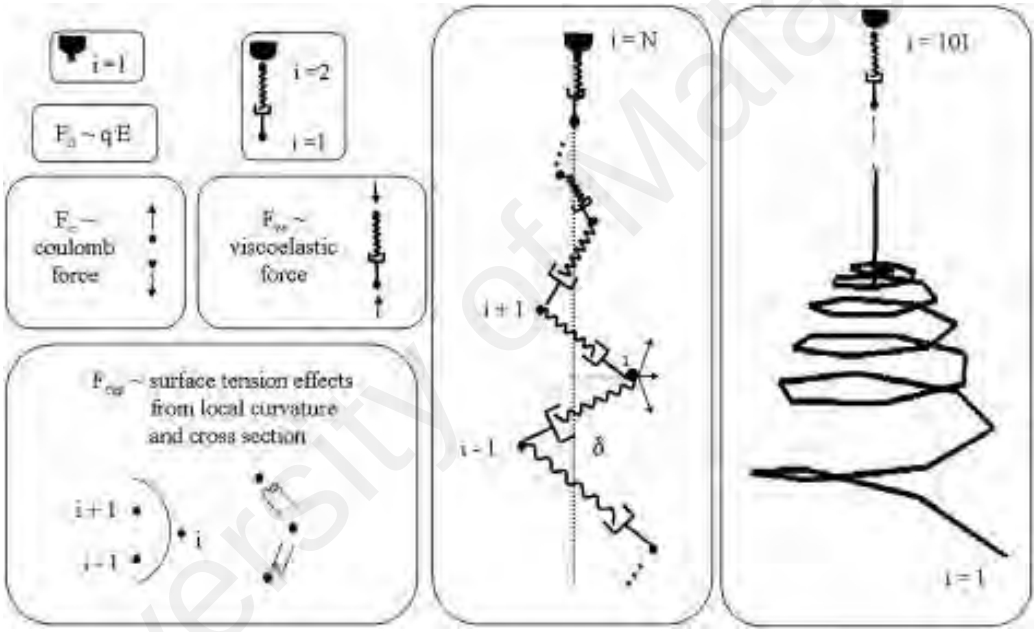

Figure 2.9: The forces used in Reneker et al. model for calculation of the path of the jet, the onset of bending, and the coiled path of the jet. δ is the radial distance of bead i. Adapted from (Darrell H Reneker et al., 2000)

The electrospinning process is the interplay between these forces and hence consideration of these parameters is important in modeling. Although existing models only consider some of the parameters affecting the process, their approximation results are experientially varied to be close and can be used to predict the outcome of electrospinning (Andrady, 2008).

University of Malaya

*(f) **Solidification into nanofiber***

During the polymer jet's flight and while undergoing the whipping instability, evaporation of the solvent will occur, leading to solidification into nanofibers. Solvent vitality is the important parameter in this process as volatile solvents may evaporate before thinning in the whipping movement could happen. This may result in thicker nanofibers (Andrady, 2008). The solidified nanofibers are deposited randomly on the collector plate. Under the optimum conditions, these fibers are generally circular, continuous and bead free. However, fibers with other morphology may be desired for certain applications.

2.3.2 Parameters affecting Electrospinning

A number of factors can affect the above-described electrospinning process and determines the outcome of the polymer fiber. Factors affecting electrospinning can be divided into polymer solution parameters and processing conditions (Ramakrishna et al., 2005).

2.3.2.1 Polymer solution parameters

*(a) **Polymer viscosity***

The solution of sufficient viscosity is required to form fine polymer fibers. Polymer chain entanglements in viscous polymer solution is required for fiber-forming and it can be achieved by increasing molecular weight or increasing concentration. At low viscosity, polymer jet either break or form beads along the deposited fiber. However, high viscosity would result in thicker fibers.

*(b) **Surface tension***

High surface tension will result in beaded fibers. Certain solvent or surfactants can be added to the solution to decrease surface tension for uniform smooth fibers.

University of Malaya

(c) ***Polymer solution conductivity***

Electrospinning depends on the stretching of the polymer by ionized electric charges. Hence, the increased conductivity of the solution will result in thinner wires. Solution conductivity may be increased by adding salt or polyelectrolyte.

(d) ***Dielectric property of the solvent***

The increasing dielectric of the solvent reduces fiber diameter and bead formation.

2.3.2.2 Processing conditions

(a) ***Voltage***

Polymer solution droplet needs to reach critical voltage to form Taylor cone and release of the jet. Higher voltage will typically result in increased stretching due to increased columbic repulsion and will result in thinner wires. However, the higher voltage favors the forming of beads.

(b) ***Feedrate***

Polymer supply rate to needle also determines fiber diameter, typically resulting in thinker wires at a higher rate.

(c) ***Needle-to-collector distance***

The distance determines the electric field strength and flight time of the polymer jet. Long flight time is necessary for polymer jet to stretch and dry the fiber. Hence, a long distance is required to achieve finer, thinner nanowires.

(d) ***Diameter of needle tip***

The inner diameter of needle tips affects the polymer jet. The smaller diameter of the tip results in thinner fibers.

University of Malaya

Besides the above parameters, ambient parameters such as humidity and ambient temperature can affect the electrospinning process. Understanding of these parameters and how they interplay are essential to fine-tune the electrospinning process for fibers with the desired diameter and morphological properties. As described above, in a traditional electrospinning setup, thinning of fiber jet mainly occurs during the whipping of fiber. Since this whipping movement only occurs within the far-field regime, only far-field electrospinning has the advantage of thinning wire in this way. Bringing the needle to near field regime increases the controllability, however, results in thicker wires.

2.3.3 Electromechanical spinning

In electromechanical spinning, the fiber jet is not only stretched by the electric field but also by mechanical pulling of the collector substrate. In this way, nano-scale fibers could be produced at a very short needle to collector distances. A schematic of electromechanical spinning setup is shown in Figure 2.10.

Besides the processing parameters discussed in the preceding section, mechanical stretching plays an important role in electro-mechanical spinning. This stretching of fiber in the collector plate results in thinner wire and increased crystal alignment of polymer chains within the wire. Fine-tuning of the fiber diameter can be achieved by changing the relative speed between the moving substrate and the needle. Faster speed usually results in thinner wires. However, polymer ink with high viscoelasticity is required to withstand mechanical stretching. With viscoelastic high molecular weight polymer ink, long polymer chains slide parallel to each other without losing their entanglement during mechanical pulling and maintain a continuous polymer fiber. Low viscoelastic polymer solution will result in the breaking of nanofibers during electromechanical spinning leading to non-continuous fiber deposition (He, Xu, Wu, & Liu, 2007; Wan, He, Yu, & Wu, 2007; S. Q. Wang, He, & Xu, 2008).On the other hand, polymers with very high

University of Malaya

viscoelasticity will result in thicker wires. They require higher electric and mechanical forces to stretch into nanofibers compromising precision control of nanofiber deposition (Deitzel, Kleinmeyer, Hirvonen, & Beck Tan, 2001). Hence, a fine balance between these two extremes has to be strived for in developing polymer ink for the electromechanical spinning process.

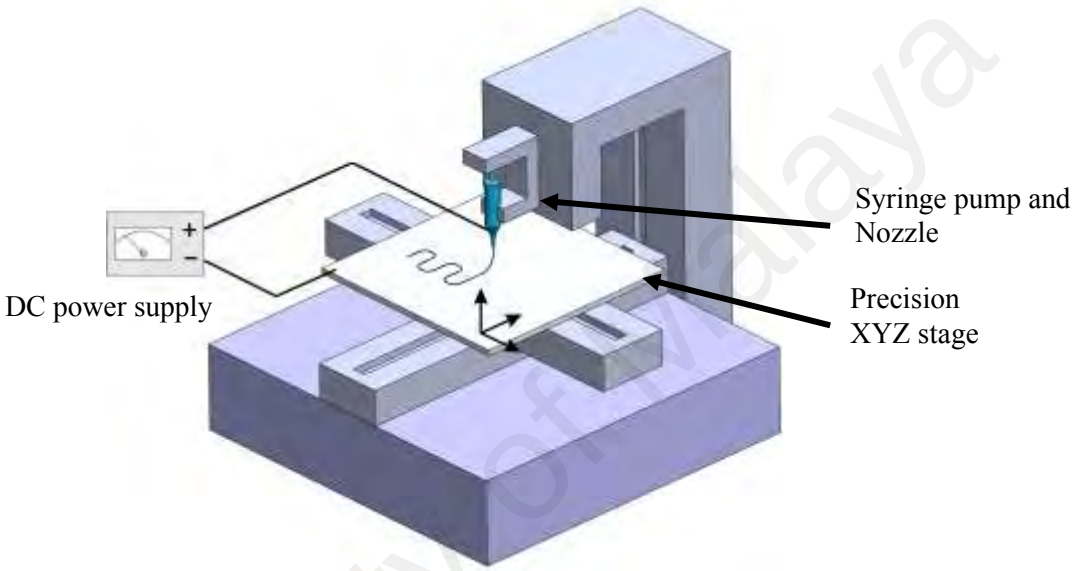

Figure 2.10: Electromechanical spinning (EMS) system setup; showing necessary components of DC power supply, syringe pump, dispensing nozzle and precision XYZ stage for patterning. The system can be controlled by a computer.

Another important parameter to control diameter in electro-mechanical spinning is by the applied electric field. Electromechanical spinning allows for the continuous and controlled deposition of nanofibers at much lower applied voltages as low as to 200V. This is lower than with NFES where voltages as high as 800V were reported (Chang, Limkrailassiri, & Lin, 2008; Sun et al., 2006; Y. Zhang, He, Li, Miao, & Huang, 2008). Low operation voltages minimize electrical instabilities and reduce the jet ejection rate, leading to more controllable and thinner fibers (G. S. Bisht et al., 2011; G. Canton, Do, Kulinsky, & Madou, 2014; S. Sharma et al., 2012; Theron, Zussman, & Yarin, 2001; F.-L. Zhou, Hubbard, Eichhorn, & Parker, 2011).

University of Malaya

2.3.4 Polymeric precursors for carbon nanowires

Although electrospinning can be performed on a large range of polymers and polymer composites, not all the polymers are convertible to carbon. To be able to carbonize by pyrolysis, the polymer precursor should contain less oxygen groups and have molecular structures that can form graphitic ring structures. Polyacrylonitrile (PAN) and SU-8 are examples of well-known carbon carbonizable polymers used to achieve carbon nanostructures. These carbonizable polymers can be electrospun and the resulting nanofibers can be converted to carbon by pyrolysis at 900°C in an inert environment. Another way to fabricate carbon nanofibers is to combine the carbonizable polymer with carrier ink polymers. It can be done by the homogenous blending of polymers or heterogeneous core-shell electrospinning. The carrier ink can be sacrificed at a later stage by solvent dissolution or by thermal decomposition. However, blending could dilute the effect of functional polymer components and may induce porosity after sacrificial processing.

Although SU-8 and PAN have been used to get carbon nanofibers in the far-field electrospinning, in their pure form, their viscoelastic properties are not sufficient for the electromechanical spinning process (Giulia Canton, 2014). Bisht et al. first reported the blending of SU-8 with high molecular weight polyethylene oxide (PEO) to increase viscoelasticity for EM. In this study, SU-8 is mixed with PEO in γ-butyrolactone solvent. This polymer ink could easily be deposited by electromechanical spinning with high patterning control. The fibers can still be pyrolyzed to carbon nanowire. The drawback, however, is the ink can only achieve micron-sized fibers instead of nanoscale fibers. Resulting carbon fiber surface also exhibited high porosity. Further development of SU-8/PEO ink has been done by Canton (Giulia Canton, 2014). It was shown that the addition of Na_3PO_4 salt increases the conductivity of the solution and allows the continuous

University of Malaya

deposition of carbon nanofibers. Optimal formulation of ink is found to be (0.5%wt. PEO, 0.5wt% of Na_3PO_4 in SU-8 2002), at which carbon nanofibers as thin as 200nm has been obtained by EMS process (Giulia Canton, 2014). The thickness of the fibers resulting from this formulation can be reduced from the micro to the nanoscale by controlling the applied voltage. The diameter decreases from 6μm to 200nm by decreasing the voltage from 800 V to 100 V. The further development of this polymer ink is needed to obtain thinner fibers in electromechanical spinning.

2.4 Surface functionalization of C-MEMS structures

As with other carbon-based electrodes such as those based on carbon nanotubes (CNT) or graphene, surface modification of the electrode surface is often necessary to activate the Carbon MEMS electrode surface. The possible oxygen-containing functional groups on a carbon surface include epoxyl, carboxyl, carbonyl, phenol, quinone and lactone groups in various C=O, O-C=O and C-OH bond arrangements. For biofunctionalization and better electrochemical performance, oxygen functional groups can be introduced to the carbon surface. Even though surface modification of CNT, graphene has been widely studied, the treatment of carbon MEMS structures has been limited to very few studies. Treatment with strong acid has been the standard surface functionalization route for CNT and graphene. However, these treatments were found to compromise the structural integrity of C-MEMS electrodes.

The first surface functionalization study of C-MEMS electrodes was done by Hirabayashi et al. (Hirabayashi, Mehta, Khosla, et al., 2013). In this study, the carboxyl group functionalization of C-MEMS electrodes was performed for further biofunctionalization with DNA. Researchers performed comparisons of various surface treatments such as nitric, sulfuric, 4-amino benzoic acids, and oxygen plasma treatment at various times. Oxygen plasma surface treatment was shown to be more reliable and

University of Malaya

less damaging to the carbon electrode while producing more oxygen functionals in significantly less time than acid treatment methods. Researchers improved C/O ratio from approximately 19 to 5. Oxygen plasma treatment of carbon creates hydrophilic carboxyl and hydroxyl bonds with accompanying improved wettability (S. C. Wang, Chang, & Yuan, 2009) and surface potential (Conway, 1999).

An alternative form of surface functionalization of C-MEMS structures for biosensor was performed using UV treatment (Penmatsa, Rahim, Kawarada, & Wang, 2015). In this study, microarrays of carbon micropillars were functionalized with aptamers for fluorescence detection of HIV-Tat peptide. Vacuum- ultraviolet (VUV) treatment was used to oxidize carbon surface with carboxyl functionals for aptamer functionalization. Researchers improve O/C ratio from 7% to 24%, of which the carboxyl group made up 15% of total carbon to oxygen bonds after treatment. In terms of C/O ratio, this translates to improvement from 14 to 4 approximately.

In biosensing, carboxylation of carbon electrodes plays an essential role as carboxylic groups can be crosslinked with amine ending from biomolecules through carbodiimide crosslinker chemistry. Moreover, hydroxyl and carboxyl groups on carbon electrodes were found to significantly improve the specific capacitance and electron transfer rate for supercapacitors and energy storage applications (Cao et al., 2018; Lai & Lo, 2015; L.-x. Li & Li, 2011; C.-C. Lin & Liao, 2011; Xiong et al., 2015).

2.4.1 Plasma treatment and microplasma direct writing

In a typical conventional plasma treatment, a low-pressure plasma is created by a radio frequency power source in a vacuum chamber. Ions from the plasma react with the target placed on the cathode in a low-pressure chamber resulting in the desired surface functional groups. This plasma setup comprises a low-pressure environment in a large and high-cost setup. In addition, a conventional plasma treatment is not able to target

University of Malaya

specific spots on a surface without using photoresist masking techniques that require more complex photolithography and lift-off steps. Hence, atmospheric pressure microscale plasma (microplasma) jets are increasingly used for localized chemical treatment and targeted nanomaterial synthesis in a wide range of applications (Belmonte, Arnoult, Henrion, & Gries, 2011; L. Lin & Wang, 2015; Shimizu, Fukunaga, Tatematsu, & Blajan, 2012). Unlike in conventional plasma treatment, a microplasma jet setup is lightweight, lower-cost, low power and operates in atmospheric conditions (L. Lin & Wang, 2015).

The most common microplasma jets described in the literature feature high-voltage electrodes in a nozzle to generate a plasma from a feed gas. A plasma jet is then emitted from a microsized opening to a target a few millimeters downstream (Dey et al., 2019; Gandhiraman et al., 2014; L. Lin & Wang, 2015). The feed gas generally involves noble gases mixed with a desired precursor gas (e.g., a mixture of argon and oxygen). In contrast, the plasma direct-writing set-up introduced in this paper uses a direct microplasma discharge created between a conductive microelectrode tip in the nozzle and the conductive surface of a target material. Hence, this configuration eliminates both the need for a microscale orifice and of noble gases. This type of direct-writing with plasma has been used, for example, to reduce metallic ions on the surface (S. W. Lee, Liang, Gao, & Sankaran, 2011).

The physics behind the plasma ignition and its propagation from the needle to the plane surface is well established (Komuro, Matsuyuki, & Ando, 2018; Wormeester, Pancheshnyi, Luque, Nijdam, & Ebert, 2010; S. Wu et al., 2018). When the electric field at the sharp tip of the needle electrode is large enough, air near the tip becomes ionized and conductive. As the electric field accelerates the ions and free electrons, they collide with gas molecules in their path multiplying ions and electrons in a process known as Townsend avalanche. The resulting corona discharge propagates from the needle tip to

University of Malaya

the plane electrode. Under high current conditions, the corona streamer discharge can evolve into an electric arc.

By integrating the plasma needle electrode in a 3-axis motion platform, an automated plasma direct-writing system can be constructed. In this work, plasma direct writing was used to pattern oxygen functional groups on carbon MEMS electrode surfaces by feeding water vapor into the plasma discharge. It has been shown that a water plasma contains various active species such as H_2O^+, OH^+, H^+, OH^-, O^- and H^- ions which can be useful for the carboxylation of carbon electrode surfaces (Nakamura, Koizumi, Nakano, & Takao, 2019; Smyth & Mueller, 1933). The ability to pattern carboxyl functional groups is suitable for the site-selective surface functionalization of carbon micro/nanoelectrodes with biomolecules e.g. to make protein or DNA arrays.

2.5 Applications of nanowires

Polymeric nanofibers from electrospinning has been applied in many advanced fields such as tissue engineering (Dvir, Timko, Kohane, & Langer, 2011), filtration (Barhate & Ramakrishna, 2007), sensors (Meng et al., 2011), energy storage systems (Y. Chen et al., 2013; Z. Zhou, Wu, & Fong, 2012), smart textiles (Rożek, Kaczorowski, Lukáš, Louda, & Mitura, 2008) and optoelectronics (Di Benedetto et al., 2008). Controllable deposition of nanowire has important applications in nanowire sensing and nanoelectronics applications. Here, current and potential applications of carbon nanowires from the C-MEMS process are briefly discussed.

2.5.1 Nanowires heaters

An interesting application of suspended conductive carbon nanowire is their use as nano-heaters in gas sensors. When direct current is applied to suspended carbon nanowire, Joule heating occurs in the nanowire as there is high resistance in nanowire's cross-sectional area compared to the support structure. Carbon nanostructures can withstand

University of Malaya

very high temperatures due to their high sublimation temperature. Suspended carbon nanowire heaters can be used as thermal deposition of materials or as nanoscale heater element in gas sensors (S. Sharma, 2013). An example of thermal deposition is tungsten oxide (WO_3) film deposition on carbon nanowire for gas sensing applications. WO_3 was deposited by decomposition of its precursor tungsten hexacarbonyl [$W(CO)_6$] by carbon nanowire Joule heating (S. Sharma, 2013).

2.5.2 Nanoelectronics

EMS patterning of conductive and semiconductive polymer nanowires could allow large scale fabrication of nanoelectronics components (Min et al., 2013; Sun et al., 2006). Min el al. has demonstrated the electrospun patterning of p-type and n-type organic semiconductor nanowire as a component of field-effect transistors (FETs) for the inverter gate arrays (Min et al., 2013). Heating-induced controlled break down of carbon nanowires enables the fabrication of nanogap for molecular circuits (Salazar, Cardenas-Benitez, Pramanick, Madou, & Martinez-Chapa, 2017) and improvement in graphitization could enable nanowires with ballistic transportation.

2.5.3 Supercapacitors and battery electrodes

An exciting area of electrospun carbon nanowires is as electrodes in supercapacitors and next-generation batteries, which are in demand as the world coming to rely on the battery-powered electronic devices. Chen et al. created a hybrid carbon nanotube/ nanofiber electrodes for lithium-ion battery anodes (Y. Chen et al., 2013). Electrospun carbon nanofibers were also demonstrated as electrodes for supercapacitors (B. Wang, Lu, Luo, & Wang, 2016; Z. Zhou et al., 2012). These electrodes have the advantages of high surface area and superior electrochemical performance of carbon and will allow the development of higher capacity fuel cells, supercapacitors, and battery electrodes. Ability to precisely pattern electrospun fiber mats could open new avenues in these applications.

University of Malaya

2.5.4 Nanowire as sensors

One application of suspended carbon nanowire is sensing electrodes for biological and chemical species. Suspended nanowires have advantages over non-suspended ones in that they have reduced electrical interferences from the substrate surface and have a higher accessible area for targeted sensing molecules. Non-suspended nanowire electrodes suffer from substrate influences such as contamination and charge shunting. Suspended electrodes also have the advantage of allowing better mass transport and increased area for sensing, which in turn increases sensitivity and limit of detection. Electrospun polymer nanowires on electrodes can be used as gas sensors (D. Chen, Lei, & Chen, 2011). They can be carbonized to obtain carbon nanowires, and their surface can be modified with a monolayer of sensor molecules. By coating nanowire with specific metal oxides, these nanowire electrodes can be used for gas sensing applications (N. Barsan & Weimar, 2001; N. Barsan & Weimar, 2003; Basu & Basu, 2009; S. Sharma & Madou, 2012; Simon, Bârsan, Bauer, & Weimar, 2001; Chengxiang Wang, Yin, Zhang, Xiang, & Gao, 2010; Xiaodong Wang, Carey, & Yee, 1995).

2.5.5 Nanowire in biosensing

Silicon nanowires with diameters ranging from 20- 150 nm have been commonly fabricated as nanowire FET based biosensor and nanowire electrochemical biosensors using standard CMOS techniques and nanolithography (Abdul Rashid, Abdullah, Yusof, & Hajian, 2013; Pham et al., 2011). Polymeric and metal nanowire sensors have also been fabricated by electrochemical deposition of nanowire suspension on a planar substrate (M. Lin, Hu, Ma, & Chen, 2012; Spain, McCooey, Joyce, Keyes, & Forster, 2015; Zhuang, Tian, Luan, Wu, & Chen, 2016).

In chemiresistive nanowire and FET biosensors, the conductivity of sensor material changes in response to the surface binding. As the dimension of nanowire sensor is in

University of Malaya

chemiresistive sensors are comparable to Debye length, a slight change in surface electrical charges can vary the material's electronic properties significantly (Prakash et al., 2016). Here, sensing took place in sensor substrate and the current doesn't need to flow through the liquid medium. Hence, unlike other electrochemical biosensing platforms, chemiresistors do not require conductive medium and redox species to perform analysis, resulting in a shorter time, simpler assay protocol and reduced reagents. Besides, chemiresistive sensors require simpler instrumentation for analysis as only the conductivity of the substrate needs to be measured (Janata, 2009) making them more suitable for point-of-care diagnosis. Hence, they have been widely applied in biosensing applications such as DNA sensing, protein sensing, and bacteria sensing (Paul K et al., 2017; Prakash et al., 2016; Rajesh et al., 2013). On-site electrospun deposition proposed in this study enables suspension of nanowire sensors to the height of tens of micrometers, which has additional advantages of having better contact with the analyte as target molecules can bind from all sides and reducing electronic interface from the substrate surface (Pramanick, Ibrahim, & Thiha, 2016).

2.6 Detection of pathogenic bacteria

Conventionally, detection and identification of pathogenic bacteria were performed in medical laboratories. Typically, specimens such as food samples, blood and stools are tested using various methods that involve cell culture, staining, biochemical assays, and microscopy. The simplest way is introducing samples to a spectrum of selective culture medium which specifically favors the growth of each bacteria. Then the cultured bacteria are strained to be observed under a microscope. This method has the drawback of taking up to several days.

Molecular detection techniques such as polymeric chain reaction (PCR) allow the detection of genetic materials of bacteria, allowing very specific and sensitive detection

University of Malaya

of pathogens. PCR still requires pre-processing of bacteria and extracting DNA from the cells which remains lengthy and expensive procedure. In addition, nucleic acid amplification by thermal cycling in PCR could take many hours. Hence, a new nucleic detection method such as loop-mediated isothermal amplification (LAMP), which simplifies the amplification step, becomes a popular detection tool for pathogenic bacteria. All these techniques take long processing times, require sample preparation, specialized equipment, and specific reagents. They also require train technicians to perform making the conventional techniques lengthy and costly. Hence, there is a special need for cost-effective, rapid, sensitive, and specific detection of whole bacteria at point-of-care settings.

2.6.1 Biomolecular probes for detection of bacteria

Aptamer-based biosensors (aptasensor) are recent advancements as alternatives for the traditional usage of antibodies as biorecognition elements. Although antibodies were used as a common probe in biosensing areas due to its high affinity and high specificity to a broad range of analytes, some limitations and drawbacks still remain as a barrier for the development of the biosensor (W. Zhou, Huang, Ding, & Liu, 2014). For instance, antibodies are susceptible to chemical modification and high temperatures (K. Han, Liang, & Zhou, 2010). The production of antibodies is also an expensive and complex process as compared to *in-vitro* selection and amplification process of the aptamer (K. Han et al., 2010).

Aptamers are single-stranded nucleic acid strands (DNA or RNA) that interact and bind the target analyte with high affinity, selectivity, and sensitivity (Hamaguchi, Ellington, & Stanton, 2001). Aptamers can be easily tailored and chemically modified to bind with various target analytes such as small molecules, proteins, nucleic acids, cells, tissues and organisms with dissociation constants of aptamer-target complexes ranging

University of Malaya

from picomolar to micromolar (Hamula, Guthrie, Zhang, Li, & Le, 2006). Hence, extensive research and effort have been channeled to the application of aptasensor for foodborne pathogen detection. Besides offering high-stability to chemical modifications, aptamers are also interesting candidates for novel, label-free, and direct detection of whole-cell bacteria using electronic biosensing platforms. Aptamers can interact and undergo conformational changes with the outer membrane protein of bacterial cells to form a unique 3D-structure, thus enable them to discriminate between protein isoforms of another bacterial cell (Davydova et al., 2016; Joshi et al., 2009; Muniandy et al., 2017). Hence, aptamers are suitable for use as probes for whole bacterial cell detection.

2.6.2 *Salmonella* infection and detection

The genus *Salmonella* consists of Gram-negative rod-shaped bacteria belonging to the *Enterobacteriaceae* family. These bacteria have 0.7 to 1.5 μm in diameter and 2 to 5 μm in length (Fàbrega & Vila, 2013). Two species, *Salmonella enterica* and *Salmonella bongori* belong to the genus. Among them, *S. enterica* has been a major source of food-borne diseases in human and animals. On the other hand, S. *bongori* are only found in cold blooded vertebrates. *S. enterica* has six sub-species and over 2600 serotypes, and many of them can cause diseases ranging from simple food poisoning to life-threatening typhoid fever. Among these, *Salmonella enterica* serovar typhimurium (*S.* Typhimurium) and *S. enterica* serovar Enteritidis (*S.* Enteritidis) are most common illness causing serotypes. Infection starts with the ingestion of bacteria contaminated food and when the bacteria reach intestinal lining in sufficient quantity, they trigger salmonellosis (symptomatic *Salmonella* infection). Even infection of nontyphoidal *Salmonella* can cause gastroenteritis that sometimes leads to paratyphoid fever. Typhoidal serotypes can pass through the lymphatic system of the intestine into the bloodstream and other internal organs, secreting endotoxins that can cause life-threatening septic. Both non-typhoidal

University of Malaya

and typhoidal *Salmonella* species contribute to significant morbidity and mortality globally.

Hence, rapid detection of bacteria is essential in early intervention to prevent mortality as well as in controlling the source of an outbreak and identifying the source. Currently, the presence of *Salmonella* is mostly detected by culturing and DNA analysis, which can take up to a week (K.-M. Lee, Runyon, Herrman, Phillips, & Hsieh, 2015). In conventional *Salmonella* detection, the sample is mixed with non-selective pre-enrichment broth (buffered peptone water) followed by selective enrichment in Rappaport-Vassiliadis medium for 24 hr in a plating procedure defined under ISO 6579:2002. The enriched sample can be streaked on *Salmonella* specific plating media. After incubation for 24 hr, plating results can be read. This method can take more than 5 days to obtain results but is widely used food safety analysis in many laboratories due to its low-cost, ease of use and high sensitivity and specificity (Maciorowski, Herrera, Jones, Pillai, & Ricke, 2006).

Nucleic acid assay such as PCR and LAMP and immunology based assays such as enzyme-linked immunosorbent assay (ELISA) offer relatively faster detection time compared to plating method, in some cases down to a single day (S. Chen, Wang, Beaulieu, Stein, & Ge, 2011; Maciorowski et al., 2006). In PCR assay, a single nucleic sequence specific to *Salmonella* can be amplified to one million-fold within 3 h using a thermostable DNA polymerase. The amplified DNA fragments are then detected by gel electrophoresis or real-time PCR measurement systems. LAMP assay simplified nucleic acid amplification and instrumentation required by using a single temperature for amplification using specific nucleic acid primers. In an ELISA assay, antigen present in *Salmonella* is detected by means of antibody specific to that antigen. The forming of

University of Malaya

antigen-antibody complex can be detected by means of color change using ELISA reader machine(K.-M. Lee et al., 2015).

Recently, a number of rapid detection techniques have been introduced that could enable on-chip detection of *Salmonella*, which includes an implementation of LAMP analysis on microfluidic chip (Sayad et al., 2018) and a graphene oxide-based electrochemical detection (Muniandy et al., 2017).

2.7 Summary

In summary, C-MEMS technology has the potential to become the foundation of next-generation electronics and sensors systems. Further miniaturization of C-MEMS to nanodomain can be achieved cost-effectively by combination with electrospinning methods, for example, to produce suspended carbon nanowire structures. Reducing electrospun SU-8 derived carbon nanowire diameters to sub-100 nm is important for chemiresistive biosensing using nanowires. In addition, understanding surface chemistry and functional group present in C-MEMS manufactured carbon structures is essential to realize their potential as a biosensor. Especially, nondestructive, and site-specific surface functionalization techniques are needed for surface modification of carbon structures. In this study, carbon nanowire sensors were demonstrated in the sensing of *Salmonella* Typhimurium, a major foodborne pathogen by observing changes in nanowire conductivity. Aptamer based sensing enables the capture of a whole-cell bacterium, removing cell lysing steps required in conventional detection.

University of Malaya

CHAPTER 3: METHODOLOGY

3.1 Introduction

This chapter outlines the fabrication steps and characterization methods undertaken to realize a suspended carbon nanowire biosensor. First, support structures for nanowires were fabricated by standard C-MEMS fabrication techniques. Then, electrospinning of SU-8 photoresist using both conventional far-field electrospinning and precision electromechanical spinning were performed to fabricate thin and uniform polymer nanofibers. The effects of various electrospinning process parameters on the morphology of SU-8 polymer nanofibers were investigated with the goal of achieving sub-100 nm suspended carbon nanowires after pyrolysis. Nanowire structures are characterized in terms of morphological, chemical and electrical properties. Suspended carbon nanowires fabricated by the C-MEMS process were then modified for biosensing with carboxyl surface functionalization and biomolecular probe immobilization. Carboxyl surface functionalization was performed with acid treatment, electrochemical treatment and plasma direct writing. Microplasma direct writing was emphasized for site-selective carboxyl functionalization of C-MEMS structures at ambient conditions. Carbon nanowire electrodes were then immobilized with *Salmonella* specific aptamer probes for sensing of *Salmonella* Typhimurium bacteria. Electrical characterization of suspended carbon nanowires was carried out at different bacterial concentrations and sensitivity and specificity of biosensor were evaluated.

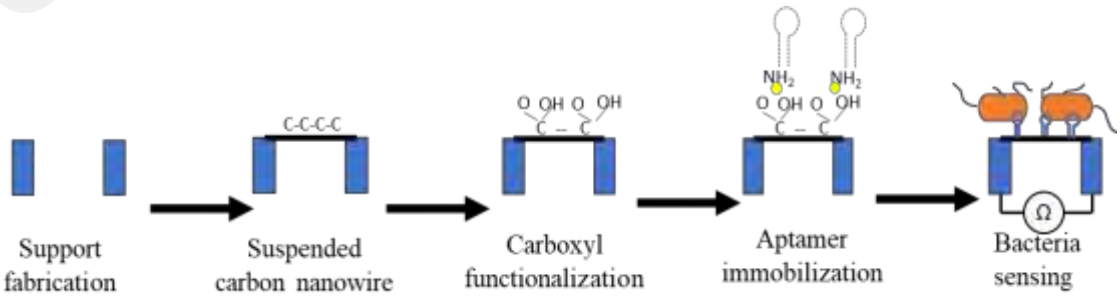

Figure 3.1: Schematic of nanowire aptamer sensor fabrication

University of Malaya

3.2 Flowchart of Research Methodology

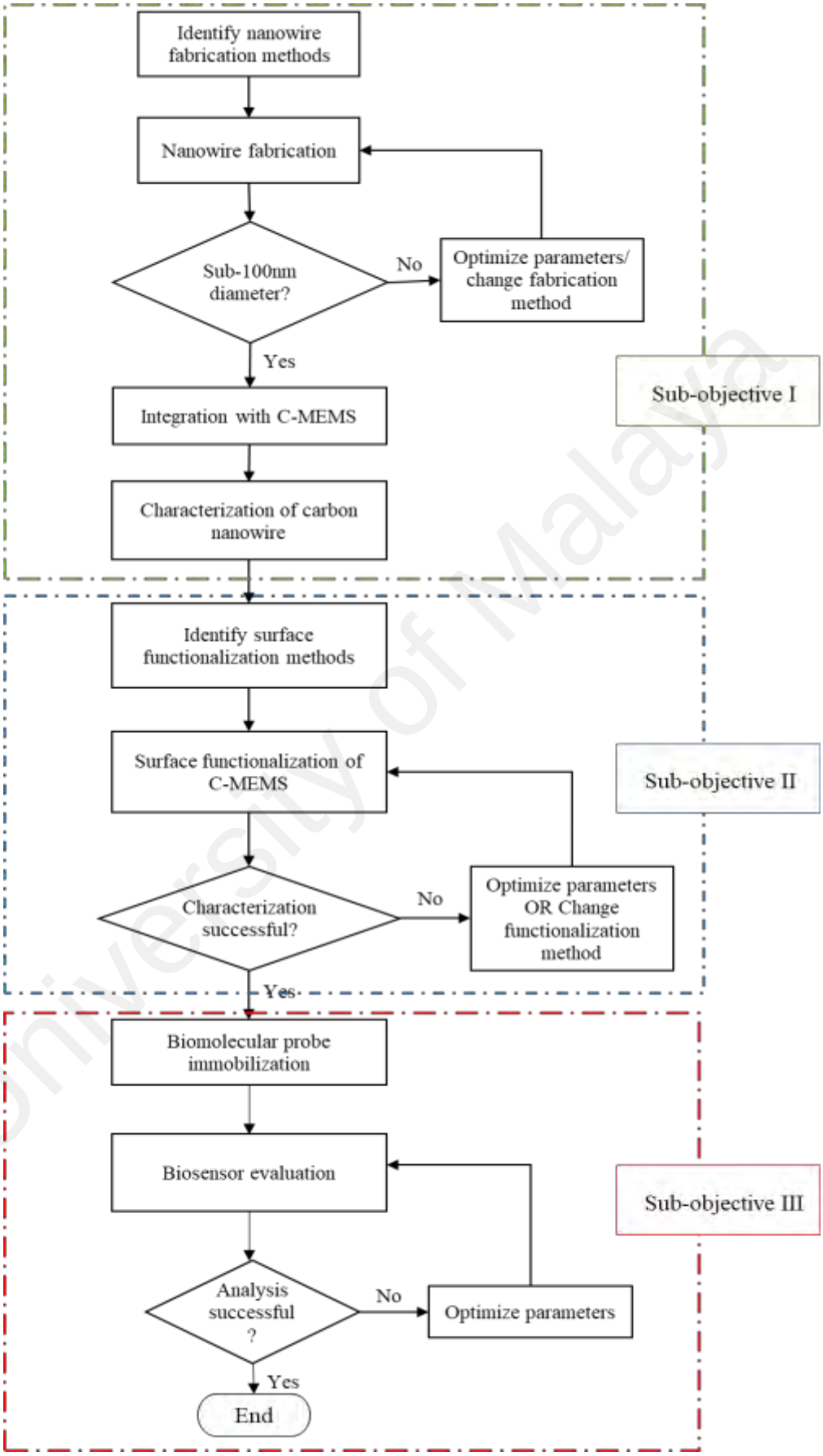

Figure 3.2: Flowchart of overall research methodology

University of Malaya

3.3 Fabrication of suspended carbon nanowires

3.3.1 Fabrication of support structures

Support structures for suspended nanowires were fabricated by the photolithography of SU-8 photoresist. The process involves the following steps. First, a photomask of desired patterns was designed and printed. Then, the photolithography process which involves spin-coating of SU-8, soft-baking, exposure, post-bake, and development were performed on a clean silicon wafer. In each of these steps, process and environmental parameters must be finely controlled to obtain repeatable structures and to ensure successful carbonization.

3.3.1.1 Photomask preparation.

The photomask for support structures was designed using AutoCAD software. Samples of electrode designs used in the experiments are shown in Figure 3.3. Several similar structures were designed to vary gaps from 10 to 40 μm. Since SU-8 is a negative tone photoresist, the intended pattern is needed to be transparent while the rest of the mask is oblique to UV. The designed photomask was printed in high resolution at 500 dpi in the polyester film by JD-photo service (United Kingdom). The photomask film is mounted on a quartz crystal glass slide with a dimension of 125 mm x 125 mm by attaching with Kapton tape.

The fabrication process of the suspended nanowire in this work required two photomasks for two-step photolithography. The first photomask is shown in Figure 3.3(a) provides support structures and electrical contact pads. Electrical contact pads are 1.6 mm wide and have 2 mm center-to-center spacing. A single chip shown in Figure 3.3(a) chip is 10 mm x 10 mm in dimension. Support structures in the center shown in Figure 3.3(b) is 20 μm wide and has 20 μm gap between them. A second photomask was used to crosslink nanowires between these two support structures selectively and it has the

University of Malaya

transparent window only between the support structures. The rectangular pattern dimensions in second photomask are 20 µm in width and 50 µm in length.

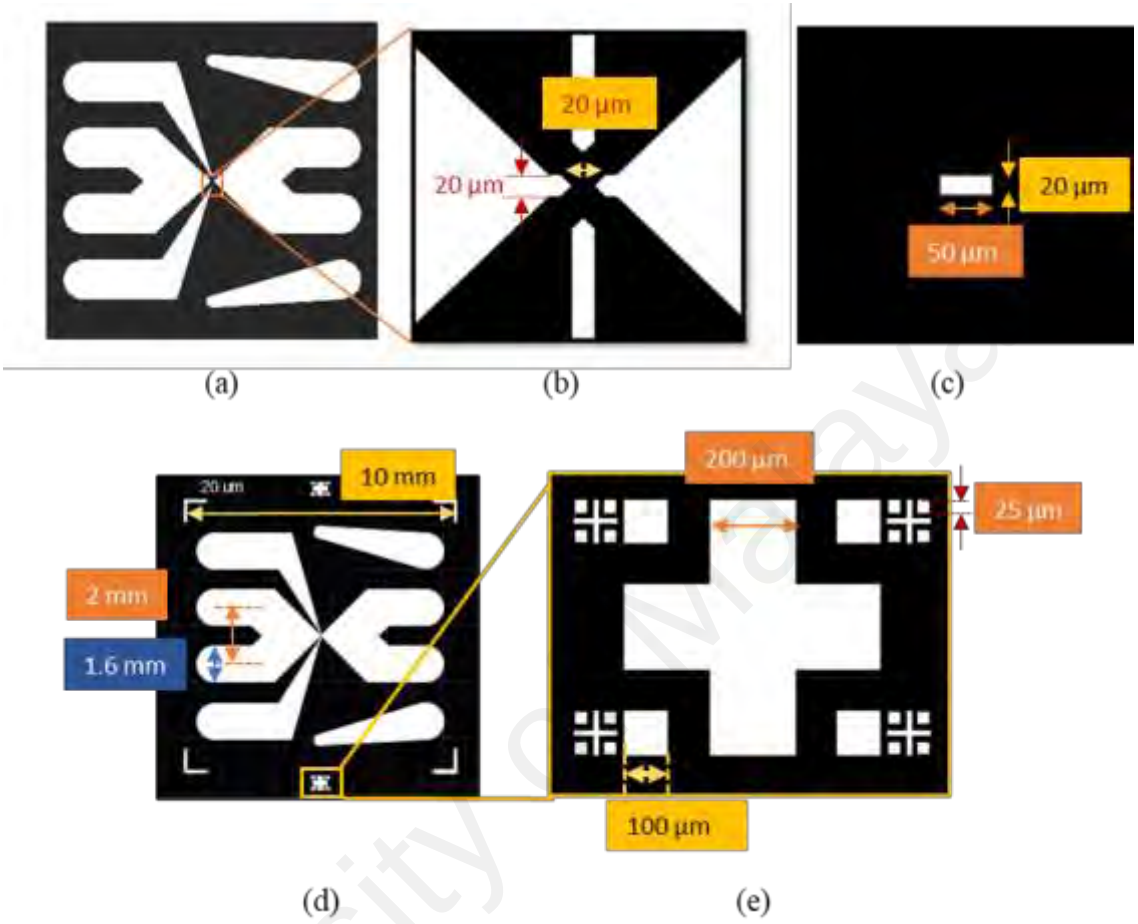

Figure 3.3: A part of final photomask used to fabricate support structures (a) photomask of a single chip with contact . (b) Magnification of the center of chip showing 20 *µ*m gap support structures for nanowire suspension. (c) Secondary photomask for UV exposure suspended nanowire magnified to equal ratio as (b). (d) Photomask with labelled dimensions and alignment marks. (e) Magnified alignment mark with dimensions.

It is important to align the two photomasks down to micrometer dimension to create suspended nanowire. In order to achieve this, alignment marks were embedded in the photomask design on each chip as shown in Figure 3.3(d). The bigger alignment cross mark with 200 µm width was used to roughly align the mask. Then, fine tuning of alignment was done with smaller 25 µm alignment mark with the help of built-in microscope in photolithography machine. The rectangle shapes in alignment mark were used in x and y adjustment while the cross shapes were important for angular rotation of

the mask. In this study, only 4 contact pads at the center were used. The remaining 4 electrode contact pads are intended for the future electrophoretic transport and manipulation of bacteria, which were not described in this manuscript.

3.3.1.2 Silicon wafer preparation

Silicon wafers with a 100 mm diameter, 0.5 mm thickness, and with a passivation film of 500 nm silicon dioxide layer were used as substrates. The silicon wafers are first cleaned with a piranha etch (a mixture containing hydrogen peroxide H_2O_2 and concentrated sulfuric acid H_2SO_4 in 1:4 ratio) and then rinsed thoroughly with de-ionized water, acetone, and isopropyl alcohol (IPA) in this order. After rinsing, wafers undergo a dehydration bake at 200 ˚C for 24 hr. Moisture and containment highly affect the adhesion of the photoresist and success of Carbon MEMS structures and hence, it is crucial that these parameters were controlled.

3.3.1.3 Spin-coating

POLOS spin coater (SPS-Europe, Germany) was used to coat the silicon substrate with thin uniform films of photoresist. The viscosity of photoresist, spinning speed, and time are the main parameters to control the thickness of the polymer deposition layer. SU-8 of different grades were investigated for the fabrication of the supporting structures. In this study, SU-8 2015, SU-8 2025 and SU-8 2050 were experimented to achieve structures with 10 μm, 20 μm, 30 μm, 50 μm thickness. Spin-coating speed was controlled (1500-4000 rpm) according to the manufacturer's specifications (MicroChem Corp.). In depositing highly viscous SU-8 varieties such as 2025 and 2050, particular care must be taken to avoid edge bead formation (build-up of resist at the wafer edges) as it interferes with uniform contact between wafer and photomask, essential for a good outcome of photolithography.

University of Malaya

3.3.1.4 Soft-bake

After the resist was coated on the substrate, the substrate was heated for partial evaporation of the photoresist solvent. This transformed SU-8 into a semi-solid state for UV exposure. A well-controlled soft-bake step increases adhesion, structure uniformity and etch resistance for final structures. The coated substrate was heated using a leveled hotplate with a uniform surface thermal profile. Soft bake parameters (time and temperature) were varied for desired thickness as described in the manufacturer's datasheet. Using an oven in this step instead of hotplate could result in the T-topping of structures as a heated upper layer could dry first and trap the solvent below.

3.3.1.5 UV exposure

The exposure step transfers the mask pattern to the resist-coated wafer activating the photosensitive components of the photoresist. In SU-8 photolithography, UV exposure activates the ions which can initiate crosslinking upon heat treatment. This step was performed using a mask aligner system (MIDAS MDA-400M, Korea). The photomask was aligned with the spin-coated silicon wafer and bring them into physical contact. Then, the vacuum was applied to make contact tighter. This step is essential if the gaps between structures (critical dimension) are smaller than 20 μm.

An important parameter in the exposure step is the amount of UV energy transferred to the photoresist. Required exposure energy depends on the thickness of the film as given in the datasheet. Accordingly, the exposure duration was adjusted based on the pre-set intensity of the UV lamp. For example, recommended exposure energy for SU-8 2015 film with a thickness of 20 μm is 150 mJ/cm^2. Hence, for the UV intensity of 5 mW/cm^2, the exposure duration can be calculated 30 s.

University of Malaya

3.3.1.6 Post-bake

A post-exposure bake was then carried out at 95 ˚C (for SU-8) for 2-10 min depending on the film thickness. SU-8 curing was a multistep process and the heat treatment in post bake crosslink polymer with photo-initiators released during UV-exposure. It is important to slowly raise the temperature to prevent the thermal stress which can reduce adhesion between photoresist and substrate resulting in dislodged patterns after pyrolysis. This step was performed in a convection oven.

3.3.1.7 Development

Wafer after post-bake was cooled to room temperature slowly. The wafer was then submerged in SU-8 developer to remove non-cross-linked SU-8. Submersion time depends on the film thickness. After rising with SU-8 developer, the patterned wafer was then rinsed with isopropyl alcohol (IPA) and dried with a compressed air gun.

3.3.1.8 Hard bake

Hard baking was performed at a temperature of 150 °C for 30 min in a convection oven to increase the attachment of photoresist to substrate preventing detachment of patterns later in the process.

3.3.2 Electrospinning of Su-8 polymer nanofibers

Electrospinning was used to fabricate polymer nanofibers/nanowires which after carbonization will form a sensing component of carbon nanowire biosensor. For biosensing, a nanowire sensor should have diameters of less than 100 nm for it to be within Debye's length of surface molecules and hence, sensitive surface charges. In order to achieve this, electrospun nanofibers should have a range of 100-200 nm before pyrolysis. In this study, both near-field electromechanical electrospinning and far-field electrospinning were investigated to suspend nanofibers on support structures. Electromechanical spinning enables the precision and repeatable deposition of SU-8

University of Malaya

nanofibers while far-field electrospinning allows fabrication of disorderly but much thinner fibers. Electrospinning can produce various morphologies of polymer from droplets, fiber with beads, short strands, and uniform fibers. Hence, fiber morphology must be controlled by meticulously tuning various electrospun parameters. Thus, the following sections will focus on the optimization of the two electrospinning techniques to achieve SU-8 polymer nanofibers of less than 300 nm by optimizing various parameters.

3.3.3 Optimization of electromechanical spinning parameters

Electromechanical spinning allows the deposition of aligned nanowires in programmable patterns. Unlike conventional far-field electrospinning, electromechanical spinning takes place within the near-field region (usually up to 2 mm from the tip of the dispensing nozzle) and much lower voltage (usually less than 1 kV). Near-field electrospinning without mechanical stretching produces the only micron to millimeter-sized fibers. In electromechanical spinning, the substrate is moved in high velocity in order to stretch fibers thinner. Hence, the use of viscoelastic polymer inks is essential for electromechanical spinning.

3.3.3.1 Electromechanical spinning system design and setup

The electromechanical spinning system used was customized system setup designed and developed “in-house” (Figure 3.4). It is composed of a precision syringe pump, an adjustable power supply of up to 1kV and a precision movement stage. The needle to collector distance is in the range of 500 μm to 2 mm. The nozzle used was 25-34 G needle with inner diameters of 150 μm to 80 μm. The syringe was mounted on a syringe pump to dispense the polymer solution at a controlled flow rate.

University of Malaya

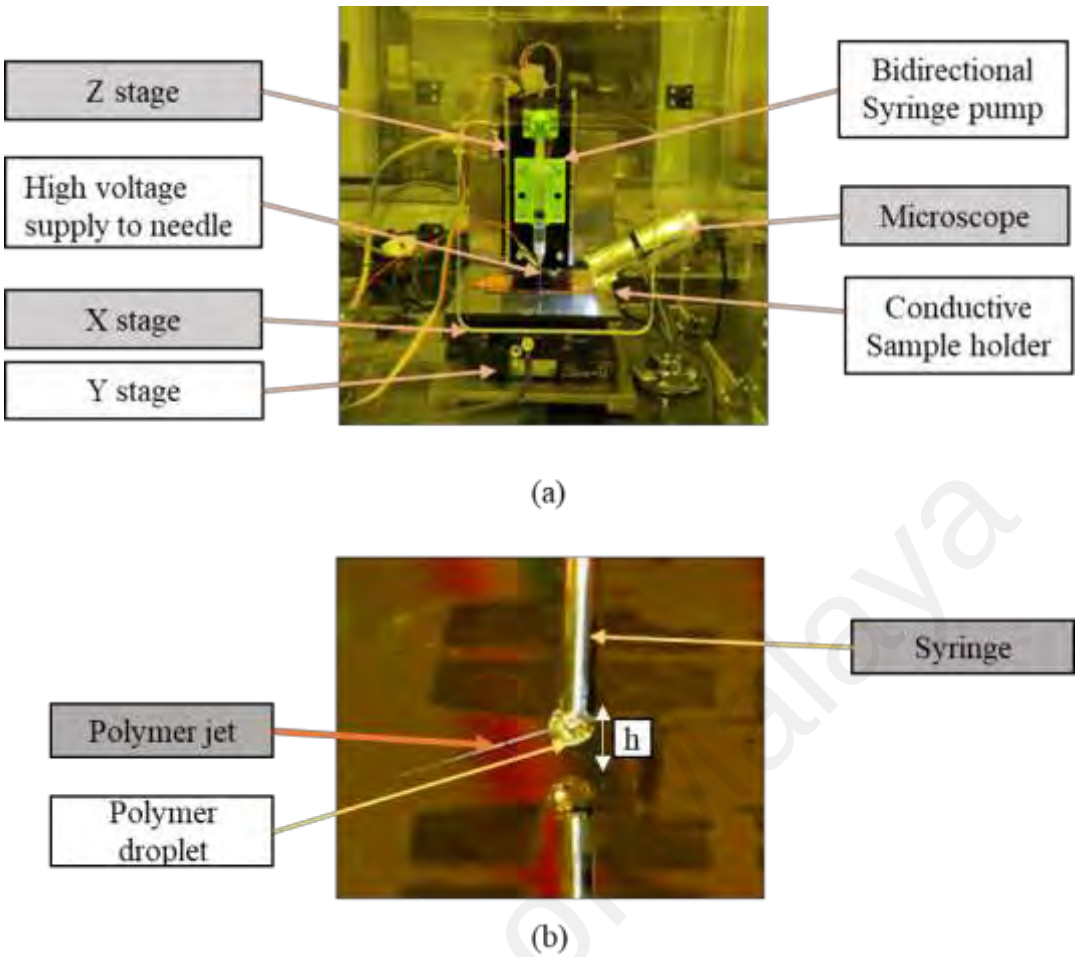

Figure 3.4: (a) Integrated electromechanical spinning setup used in the experiments. (b) Close-up view of nozzle showing polymer droplet and polymer wire. Syringe to substrate distance, h is typically 0.7 mm.

The target substrate can be mounted on an X-Y micro stage which can move in a programmed pattern at a defined speed. Movement resolution is important for positioning of nanowire writing whereas velocity determines thinning of the polymer fiber. For x and y directions, precision piezoelectric motorized stages (Physik Instrumente, Germany) were employed. Piezo motors offer better resolution, accuracy, and repeatability. Also, there is no backlash compared to servo motors because piezo stages lack rotary and screw components. X and Y stages have a resolution of 0.1 µm (100 nm) and a maximum velocity of 350 mm/s. Z stage has a movement precision of 1 µm and a maximum velocity of 20 mm/s. Each component can be controlled through a computer user interface shown in Figure 3.5: Developed user interface to control electromechanical spinning system with video recording showing close-up of the nozzle, control buttons and sequence

University of Malaya

programming in macro mode.. The pattern of polymer deposition can be pre-programmed through macro mode. The power supply was connected between the needle and XY stage to provide high voltage bias.

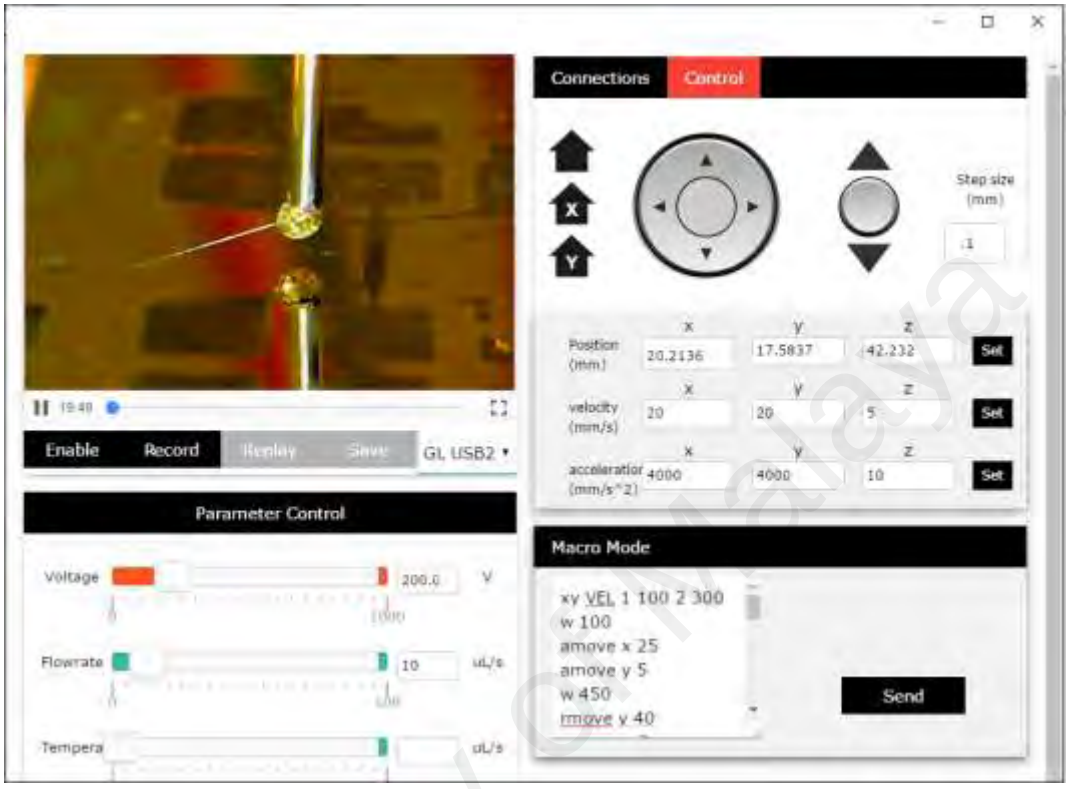

Figure 3.5: Developed user interface to control electromechanical spinning system with video recording showing close-up of the nozzle, control buttons and sequence programming in macro mode.

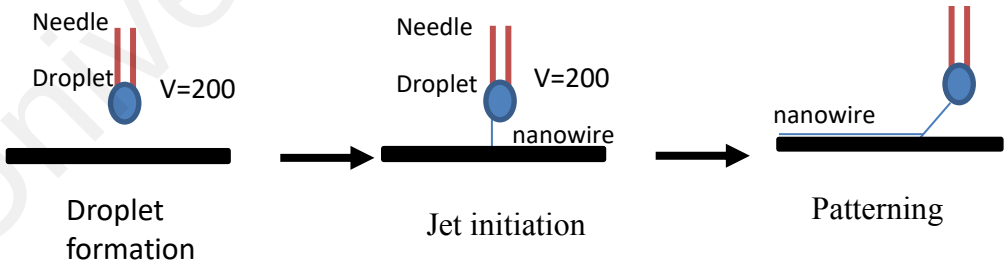

Figure 3.6: Schematic of the electromechanical spinning process.

The polymer solution flows through the needle to form a droplet at the needle tip. In low voltage electromechanical spinning, polymer jet does not self-initiate as the electrostatic force is not strong enough to overcome the surface tension at the droplet-air interface. Hence, it is necessary to introduce artificial disturbance to initiate the jet. This was achieved by poking the polymer droplet with a fine micro-glass tip (10 µm diameter)

University of Malaya

or by applying temporary high voltage in the range of 3-5kV for a millisecond. After the jet is initiated, polymer jet continues to flow as long as the electric field is maintained, and the polymer solution is available. The stage can then be moved to deposit polymer fiber in desired patterns.

3.3.3.2 Materials

As electromechanical spinning requires viscoelastic ink to be able to stretch fibers without breaking, SU-8 polymer was modified to add viscoelasticity. The base ink used in this work was adapted from the previous study (Giulia Canton, 2014). In this composition, high molecular weight poly(ethylene oxide)-PEO (MW = 4000000) (Sigma Aldrich) was added to increase viscoelasticity and a conductive salt, tetrabutylammonium tetrafluoroborate (BS4) of 0.5% weight percentage was added to improve the conductivity of SU8 2002 polymer solution. In addition, various polymer compositions such as PEO concentration of 0.5% and 1% and SU-8 dilutions to 50% and 75% were used to study the effect of polymer viscoelasticity on electromechanical spinning.

3.3.3.3 Experimental Protocol

Various concentrations of PEO were added to SU-8 2002 polymer solution and their effect was observed. Besides the polymer ink, voltage and stage velocity are two main process parameters that controls the diameter of nanofibers. Effects of voltage and stage velocity on fiber diameter were investigated in which voltage was varied from 100 V to 1000 V and stage velocity was varied from 25 mm/s to 300 mm/s.

3.3.4 Optimization of far-field electrospinning parameters

3.3.4.1 Apparatus setup

The far-field electrospinning system was designed and fabricated “in-house”. A precision syringe pump was used to control flowrate. High voltage supply was set up by using a high voltage source with a customized control circuit. The unit has controllable

University of Malaya

voltage from 1k to 30kV. A precision syringe pump was used to supply SU-8 polymer to the needle tip. The needle is connected to high voltage source by crocodile clip as shown in Figure 3.7. An aluminum sheet is used as a grounded collector electrode by connecting to ground electrode of high voltage source. The silicon wafer can be attached to the sheet by means of electrically conductive carbon tapes.

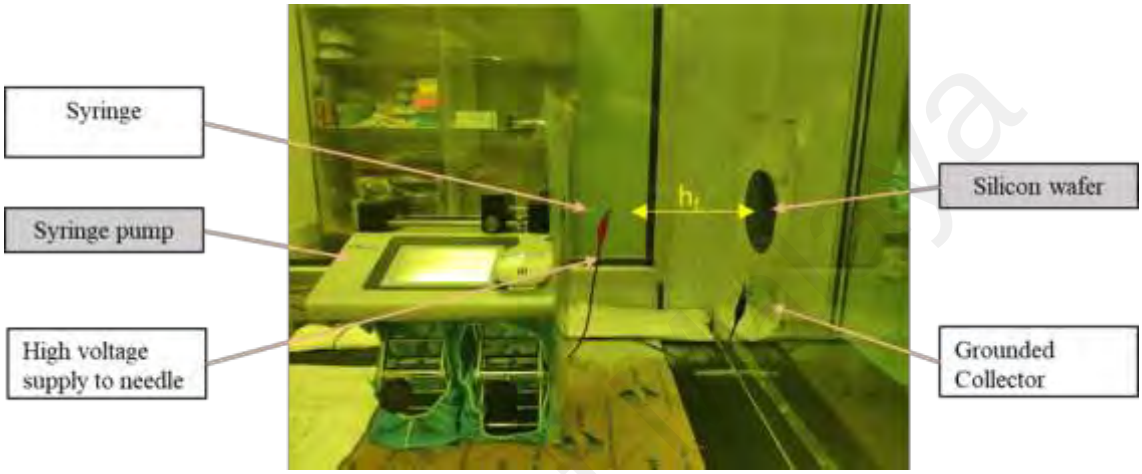

Figure 3.7: Far-field electrospinning setup. Parameters used in the experiments are presented in Table 3.1.

3.3.4.2 Materials

SU-8 2015 (MicroChem, USA) was used in the far-field electrospinning experiment. To find the optimum polymer properties for electrospinning, various compositions with added viscoelastic PEO and conductive BS4 salt were formulated. All solutions were drawn into 1 mL syringes and were placed vertically in a vacuum desiccator to remove gas bubbles before electrospinning. A 100 mm diameter silicon wafer coated with silicon dioxide was used as collector.

3.3.4.3 Experimental protocol

Electrospinning experiments were performed while varying the following parameters: voltage, flow rate, distance, nozzle diameter, solution viscoelasticity and conductivity. Solution viscoelasticity was varied by adding PEO and conductivity was varied by adding

BS4 salt. First, the effects of individual parameters were investigated to identify the range that can generate fibers (as opposed to droplets, beads and short strands). For a parameter under investigation, other parameters were fixed. Parameters under investigation and the corresponding values used are presented in Table 3.1.

Table 3.1: List of variables investigated and corresponding values used in far field electrospinning

Variables	**Values**
Voltage	7, 10, 13, 16 kV
Flow rate	5, 7.5, 10, 15 $\mu Lmin^{-1}$
Needle to collector distance (h_f)	7, 10, 13, 16 cm
Needle diameter	18, 22 ,32 Gauge
Solution viscoelasticity	0%, 0.01%, 0.05%, 0.1% PEO weight percent
Solution conductivity	0%, 0.01%, 0.05%, 0.1% BS4 weight percent

From these results, the desired polymer composition and flow rate were decided, and electrospinning was further optimized based on voltage and distance. The optimal electrospinning parameters obtained were used to fabricate suspended nanofibers on support structures. The fibers were crosslinked by exposing to UV and heat treatment. Silicon wafer pieces were used as the collector for the fibers. All electrospinning experiments were performed under yellow light to ensure that the SU‐8 solutions were not crosslinked.

Samples were inspected with a Scanning Electron Microscopy (SEM) for the morphology analysis. For the final optimization, Field Emission Scanning Electron Microscopy (FESEM) was used to analyze fiber diameters as FESEM provides higher resolution pictures. The resulting micrographs were analyzed, and fiber diameters were

University of Malaya

measured using ImageJ software. For the quantitative analysis of micrographs, two parameters of interest were mean fiber diameter and fiber diameter distribution. The average fiber diameter specifies nanofiber thickness while histogram and a standard deviation of diameter distribution indicate the degree of uniformity.

3.3.5 Fabrication of suspended nanowires on support structures

3.3.5.1 Depositing of fiber on support structures

For the electromechanical spinning, patterned SU-8 chips were diced and place on the conductive plate. Then, a single SU-8 fiber was deposited between support structures using the optimized parameters.

For the far-field electrospinning, whole silicon wafer patterned with support structures were placed on an electrically grounded collector plate with double-sided conductive copper tapes. Electrospinning was performed with the parameters and setup described earlier. The optimized parameters as obtained from experiments in section 3.3 were used. Electrospinning was performed for varying times from 10s to 3 mins to optimize nanofiber deposition on supporting structures.

3.3.5.2 Vacuum drying of fibers

In a standard photolithography process, spin-coated SU-8 was heat-treated to remove the solvent. However, heating non-crosslinked SU-8 nanofibers results in the melting of nanofibers and changed morphology. Hence, vacuum drying is used to remove photoresist solvents in nanofibers partially. The resulting fiber mat on a silicon wafer is then put in a vacuum desiccator for 24 hr to dissipate the remaining solvent.

3.3.5.3 Photolithography of suspended nanowires

A second photomask was used to selectively crosslinked suspended nanowires on support structures (see Figure 3.3 (c)). The photomask used here has a transparent window

University of Malaya

between support structure while the rest is oblique to UV rays. The mask was positioned on patterned support structures using the mask aligner. Suspended nanowires underwent a photolithography process as previously described except for the soft-bake step. Here, the electrospinning process and vacuum drying steps partially removed the photoresist solvent replacing the soft-bake step. UV exposure was performed for 10 s in the mask aligner machine and then, the wafer was heated to 95 °C in an oven. Wafer was then submerged in developer solution to remove non-crosslinked fibers.

3.3.6 Carbonization of polymer structures

Pyrolysis of the electrodes was performed at 900°C in a nitrogen atmosphere in a tube furnace (Nabertherm, Germany). The quartz tube for the furnace has inner diameter of 50 mm and length of 1000 mm. The heating zone length of the furnace is 50 mm. The developed wafer was diced with a diamond cutter to produce individual electrodes as tube diameter is smaller than the wafer diameter The chips were positioned inside the ceramic cubicle. Then, the cubicle was inserted into the furnace and positioned on the heating zone. Nitrogen gas of 99.9995% purity was used for pyrolysis and the gas flow rate was set at 2000 sccm. The temperature ramping rate in the pyrolysis process is crucial to reduce thermal cracks and porosity in pyrolyzed carbon electrodes. In the experiment, a temperature ramping rate of 2 -5°C per minute was used in both heating and cooling steps. An example of a pyrolysis temperature profile was described in Figure 3.8 which shows two-step pyrolysis with an additional hard-baking step of 200 °C at 30 mins during pyrolysis. Nitrogen gas was released into a quartz tube 10 mins before heating was switched on in order to remove all oxygen from the tube. The gas flow was only turned off after the machine has been cool down to 200 °C.

University of Malaya

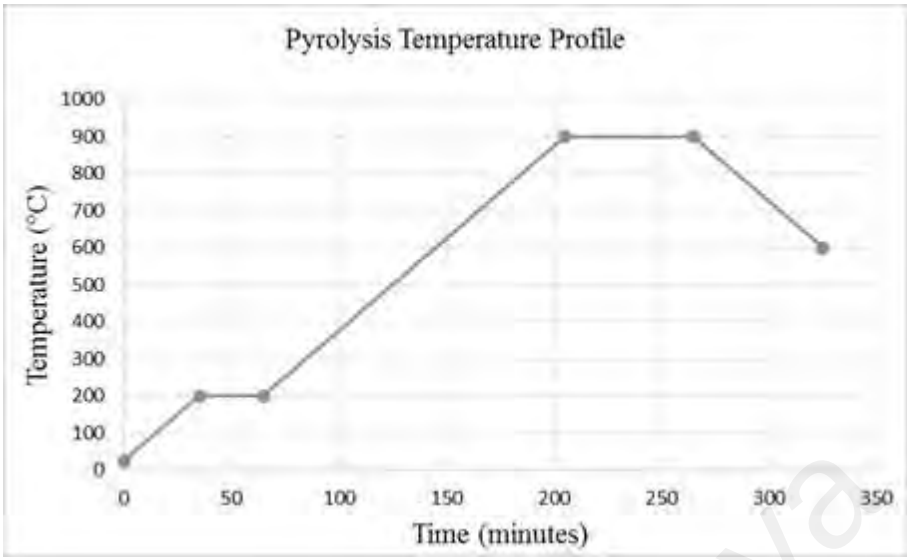

Figure 3.8: Pyrolysis temperature profile to carbonize photoresist polymer patterns. Temperature is ramped up at 5°C per minute from room temperature. Dwell time of 30 min at 200°C and 60 min at 900°C were used. After a controlled cool down to 600°C, the machine is turned off.

3.3.7 Characterization of carbon structures after pyrolysis

The morphological study of carbon structures was performed by optical microscope and field electron scanning electron microscopy (FESEM) (Hitachi SU8030, Japan and Zeiss SIGMA, Germany). The physical dimension of before and after pyrolysis was measured and analyzed from the micrographs. Electrical characterization was carried out by the source-measurement unit (SMU) (Keithley 2400, US) measuring current-voltage (*I-V*) characteristics. SMU probes were positioned on contact electrode pads near support structures. The schematic of electrical testing scheme is shown in the Figure 3.9.

University of Malaya

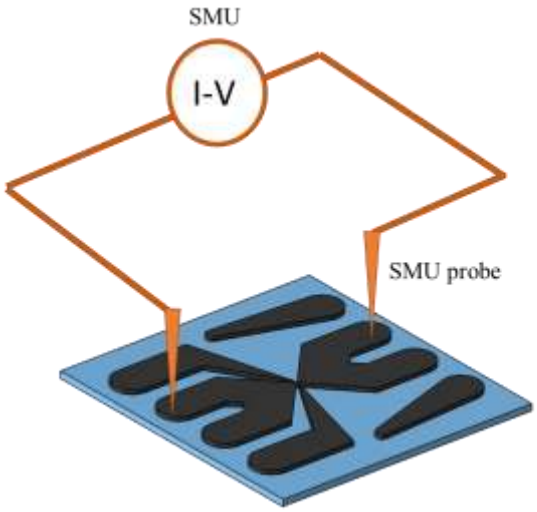

Figure 3.9: Schematic of electrical characterization using source-measurement unit in which current response is measured over a range of voltage (-0.1V to 0.1V).

To study the resistivity of carbon film, a rectangle carbon structure with a defined dimension was fabricated. From the results, the resistivity of support carbon structures and carbon nanowires were calculated. Raman spectrum analysis (Renishaw inVia Raman microscope, UK) and X-ray powder diffraction (XRD) (Bruker d8 ADVANCE, US) analysis were performed to understand the graphitization degree of resultant carbon structures.

3.4 Investigation of surface properties of C-MEMS structures and surface functionalization of carbon electrodes

Carbon electrodes fabricated by the C-MEMS process is known to be chemically inert. This section outlines the study of functional groups on as-pyrolyzed C-MEMS structures and surface functionalization of electrodes with carboxylic groups in order to immobilize biomolecular probes. Conventional surface functionalization techniques such as treatment with strong acids and electrochemical treatment. A new selective surface functionalization using "in-house" developed microplasma direct writing were performed. To investigate surface functionalization, carbon film electrodes were produced using C-MEMS techniques. The surface chemistry was investigated by scanning electron microscopy (SEM), Energy-dispersive X-ray spectroscopy (EDS),

University of Malaya

Fourier transform infrared spectroscopy (FTIR) and x-ray photoelectron spectroscopy (XPS).

3.4.1 Fabrication of Carbon Film Electrodes

Carbon film electrodes were fabricated by standard C-MEMS fabrication techniques. Negative photoresist, SU-8 2015 was spin-coated onto a silicon wafer with 1 μm silicon dioxide layer. Spin coating is performed at 4000 RPM for 30 s to achieve a 13 μm thickness photoresist film. The sample was then soft-baked over hotplate at 95 °C for 3 minutes for solvent evaporation. It was then exposed in UV for 28 s and post-baked at 95 °C for cross-linking. SU-8 developer was used to remove the unexposed photoresist. Obtained polymer photoresist film was converted into conductive carbon film electrodes by pyrolysis with the parameters discussed in section 3.3.6.

3.4.2 Acid treatment

Acid treatments were performed in concentrated acids such as 98% sulphuric acid, 70% nitric acid, and 37% hydrochloric acid (ACS reagents). Carbon electrodes were immersed into acid and incubated for various times ranging from 6hr to 24 hrs. The electrodes were then rinsed with deionized water and dry in the oven at 60 °C for 2 hr.

3.4.3 Electrochemical treatment

Electrochemical oxidation was performed in 1 M sulphuric acid as electrolyte in a conventional three-electrode electrochemical cell setup. Fabricated carbon electrodes were used as working electrodes. A platinum electrode was used as a counter-electrode and Ag/AgCl electrode as a reference electrode. Cyclic voltammetry experiments were performed from -1.5 V to 1.5 V at a scan rate of 0.1 V/s.

University of Malaya

3.4.4 Microplasma direct writing

Microplasma direct-writing enables a simple, low-cost and low-power technique for site-selective plasma patterning of C-MEMS electrodes with oxygen functionalities. In a microplasma writing setup, a high-voltage source generates a microplasma discharge between a microelectrode tip and a target surface. Water vapor acts as an ionic precursor for carboxylation and hydroxylation of carbon surface atoms. Figure 3.10 illustrates a home-build experimental plasma direct writing setup consisting of a 3-axis motion control platform and plasma nozzle. The 3-axis motion platform was modified from the electromechanical spinning system setup described earlier with a plasma generating nozzle replacing the syringe pump. The nozzle is composed of water vapor mist generator and tungsten microelectrodes connected with high voltage supply for generating plasma as shown in Figure 3.10(b). Water vapor mist was generated by a vibrating mesh screen ultrasonic transducer which is in contact with water-soaked sponge.

The mesh with micro size holes was vibrated in ultrasonic frequencies causing water on one side of the surface to be atomized and released as aerosol mist from the other end. Then, the airflow (~500 sccm) serves as a carrier to bring the water vapor mist downstream to a nozzle. Sheath gas (either nitrogen or compressed air) was directed from a second outer nozzle. Sheath gas acts as a concentrating force for water vapor flow and remove deposited mini water droplets on the electrode surface. The flow rate of sheath and carrier gases were experimentally tuned to achieve optimum results. The nozzle housing was fabricated by 3D printing.

University of Malaya

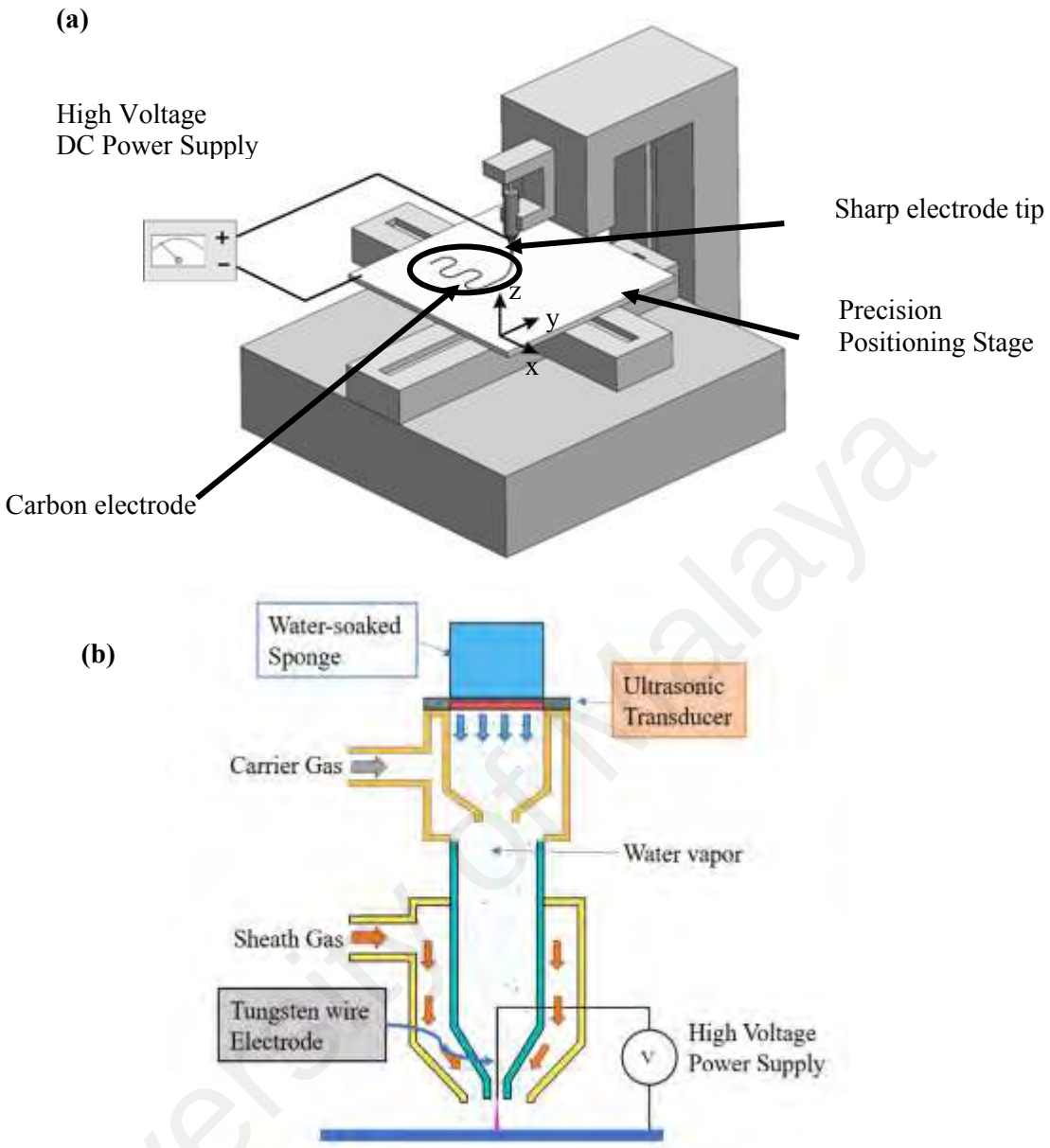

Figure 3.10: Schematic of plasma direct-writing setup. (a) Programmable micro stages for pattern writing. (b) Microplasma generating nozzle.

The tungsten wire electrode of 100 μm diameter was positioned at the center of the nozzle and connected to a high-voltage source. A radio frequency high voltage source of 5kV at 5 MHz was used in the study. A high voltage source is applied between the tungsten wire tip and conductive platform which induces plasma discharge from the needle tip. Plasma discharge occurs when the needle tip is within 4 mm distance from the target carbon electrode. Plasma current was stabilized by high impedance load connected in series with voltage supply in order to prevent streamer from propagation to arc

University of Malaya

discharge. The voltage source can be controlled from a computer over timing and frequency of plasma through a microcontroller. The plasma streamer ionizes water molecules generated from the back of the nozzle creating reactive oxygen species that bombard the target. The nozzle was mounted on 3-axis motion stage which can be numerically controlled by g-code commands through the computer. The surface carboxylic functionalization degree was varied by exposure time over a target area. Direct-writing of the functional groups is demonstrated by patterning on the 10 μm thick SU-8 derived pyrolyzed carbon film fabricated by the carbon MEMS process.

3.4.5 Surface characterization

As-pyrolyzed C-MEMS structures and plasma direct-written structures were investigated for their surface functional groups. After plasma direct writing, a nitrogen air gun was used to remove any water residues on carbon electrodes. Then electrodes were dried in the drying oven at 60 °C for 2 hr. For surface analysis, FESEM units (Hitachi SU8030, Japan and Zeiss SIGMA, Germany) were used for image acquisition and EDS elemental measurement. C/O ratios were calculated from EDS and XPS measurements. FESEM image and EDS elemental maps were used to calculate the resolution of patterning. XPS (PHI Quant era II, Chigasaki, Japan) was used to further verify the presence and percentage of carboxylic and other oxygen functionals on the electrode surface. The water contact angle was examined by self-build apparatus comprising a horizontally mounted zooming camera and droplet dispenser.

3.4.6 Electrochemical measurements

The electrochemical responses from plasma direct written carbon surface and pristine carbon surface were investigated using μStat 400 multi-potentiostat (DropSens-Metrohm, Asturias, Spain). Three-electrode configuration was used with fabricated pyrolyzed carbon electrode as the working electrode, Ag/AgCl a reference electrode and screen-

University of Malaya

printed carbon electrode as a counter electrode. 0.5 M sulphuric acid was used as the electrolyte in evaluating specific capacitances and double layer capacitances. 1mM K_3 [$FeCN_6$] /0.1 M KCL solution was used to evaluate the redox reaction. The solutions were deaerated by bubbling high purity nitrogen gas for 15 min before measurements.

3.4.7 Crosslinking with DNA aptamer probes

In order to examine the immobilization efficiency of biomolecules, amine-modified DNA aptamer probes were immobilized to plasma written surface. Aptamers were dissolved in deionized water to a concentration of 5 μM. The amine-functionalized aptamer was covalently attached to the carboxylic groups with the assistance of sulfo-N-hydroxysuccinimide (sulfo-NHS) and N-(3-dimethylamnopropyl)-N-ethylcarbodiimide hydrochloride (EDC) (sulfo-NHS 0.1 M, EDC 0.4 M) mixed in 0.1 M MES buffer (pH 5.5-5.9) for 30 min. The electrodes were then washed with 0.1M MES buffer to remove the unbound residues and were dried. Then, 5 μL of 5 μM aptamer solution was drop-casted on the chip and incubated for another 30 min and the chips were washed with DI water. The solution containing the complementary aptamer strands with fluorescence tagging was then added to the carbon surface and washed after incubation of 20 min. Fluorescence microscopy was used to observe the immobilization of aptamers.

3.5 Development of a chemiresistive *Salmonella* sensing assay using an aptamer-based carbon nanowire sensor

Suspended carbon nanowire sensors were fabricated by the C-MEMS process of SU-8 photolithography followed by carbonization. For final electrode design, support structures were fabricated to the height of 15 μm. Suspended carbon nanowires were fabricated as discussed in section 3.3. Using the FESEM, a carbon nanowire electrode with less than 100nm diameter nanowires was selected and modified for biosensors. Steps involved in biosensor chip fabrication is described in Figure 3.11.

University of Malaya

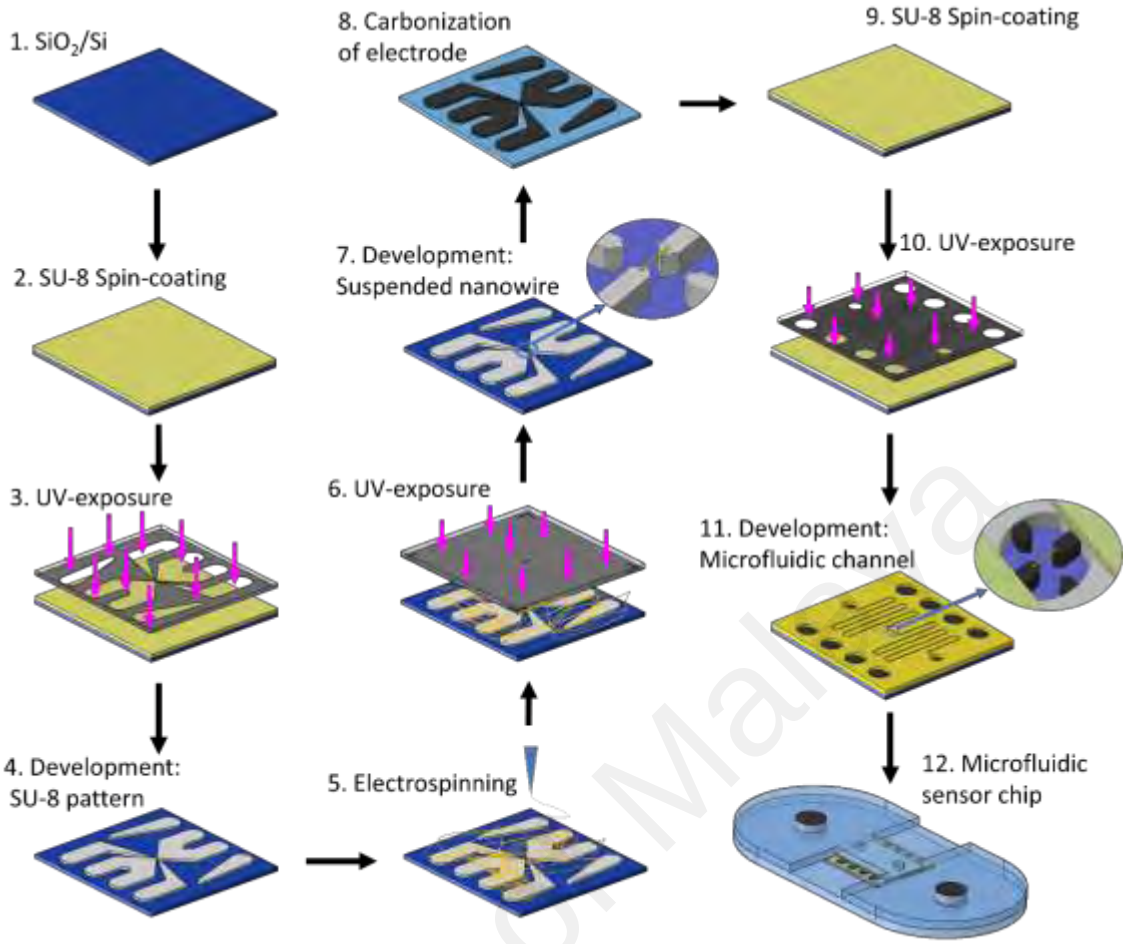

Figure 3.11: Schematic illustration for fabrication steps of carbon nanowire biosensor. Insets show the magnification of suspended nanowire area.

3.5.1 Integration with microfluidics

The base microfluidic structures on sensor chips were fabricated using photolithography of SU-8 photoresist as shown in step 11 of Figure 3.11. This step has the dual purpose of insulating the non-active electrode area and making a microfluidic channel on the chip exposing only the nanowire sensing element. The process involved spin-coating carbonized nanowire electrodes with SU-8 2002 photoresist to a thickness of 2 μm. SU-8 microfluidic pattern was obtained after UV exposure under a designed mask and resist development. As SU-8 structures are hydrophobic, the channels were treated with plasma direct writing. The resultant sensor chips were diced and incorporated into a microfluidic housing made of Poly(methyl methacrylate) (PMMA) fabricated using Computer Numerical Control (CNC) machining. Binding between SU-8 microfluidic

University of Malaya

layer on the sensor chip and PMMA structures was achieved by a pressure-sensitive adhesive layer which was patterned using a cutting plotter (GCC PUMA II, USA).

3.5.2 Immobilization of DNA aptamer probe on carbon biosensor

Salmonella-specific DNA aptamer probe (Joshi et al., 2009) with sequences of (5′ -TATGGCGGCGTCACCCGACG GGGACTTGACATTATGACAG-3′) was modified with amine (-NH_2) group at the 5'end. Aptamers were dissolved in deionized water to a concentration of 5 μM. The amine-functionalized aptamer was covalently attached to the carboxylic groups with the assistance of sulfo-N-hydroxysuccinimide (sulfo-NHS) and N-(3-dimethylamnopropyl)-N-ethylcarbodiimide hydrochloride (EDC) (sulfo-NHS 0.1 M, EDC 0.4 M) mixed in 0.1 M MES buffer (pH 5.5-5.9) for 30 min. The electrodes were then washed with 0.1M MES buffer to remove the unbound residues and were dried. Then, 5 μL of 5 μM aptamer solution was drop-casted on the sensor chip and incubated for another 1 hr. Current-voltage (*I-V*) characterization was used to investigate the conductivity of nanowire in each step of functionalization.

3.5.3 Preparation of Bacteria and Bacterial sensing

To evaluate the biosensing platform, 5 μL volume of bacterial suspensions of different concentrations were introduced to microfluidic chips and incubated for 5 min at room temperature. Serially diluted *Salmonella* Typhimurium cell suspensions with concentrations ranging from 10^8–10^1 CFU mL^{-1} were used in the experiment. Dilutions of bacterial cultures were confirmed by viable plate count. To test the selectivity of the sensing platform, different types of bacteria, namely *Escherichia coli*, Shigella *dysenteriae, Vibrio cholerae* and *Kebseilla pneumoniae* suspensions were prepared. After incubating with the bacterial suspensions for 5 min, the I-V characterizations were carried out for the individual sensor chips.

University of Malaya

Bacterial cultures were obtained from the culture collection of the Biomedical Science Laboratory, University of Malaya, Malaysia. The developed biosensor platform was tested with real food samples. 25 g of beef samples were collected from 6 different markets. The samples were homogenized in 225 mL of Buffer Peptone Water (BPW) for 4 h at room temperature. To compare electronic detection results with plate count, meat homogenate was transferred into Rapport Vassiliadis broth followed by 24 h of incubation at 42 °C. This enriched broth was then serially diluted to obtain a bacterial suspension in a range of 10^8–10^1 CFU mL^{-1}. Bacterial cell densities in diluted suspensions were evaluated by plating onto Brilliance *Salmonella* agar followed by incubating at 37 ºC overnight. Diluted bacterial suspensions were introduced to nanowire electrodes and incubated for 5 min followed by electrical detection. The results were cross-checked with viable plate count method.

3.5.4 Electrical characterization

The fabricated suspended carbon nanowires were electrically characterized before and after functionalization and after incubation with bacteria at different concentrations. The *I-V* characterization was carried out from -0.1 V to 0.1 V at a scan rate of 10 mV/s in AutoLab electrochemical workstation with the setup described in Figure 3.9. Changes in resistance as a percentage were calculated and plotted.

University of Malaya

CHAPTER 4: RESULTS AND DISCUSSIONS

4.1 Introduction

This chapter is organized in three sections discussing the experimental results of the fabrication steps. First, suspended nanowire electrodes were fabricated by a combination of electrospinning and standard C-MEMS techniques. The effects of electrospinning parameters on fiber morphology were investigated on both near field electrospinning and far-field electrospinning with the objective of fabricating thin uniform polymer nanofibers, which can give sub 100 nm nanowires after carbonization. Electrical and chemical properties characterizations were performed on carbon nanowire electrodes. Secondly, carboxyl functionalization of carbon electrodes was performed by plasma direct writing and chemical characterization of functional groups is described. Finally, the nanowire microchips were integrated with microfluidic channels and were evaluated as a biosensor in sensing of *Salmonella* Typhimurium. The sensor chips used aptamers as probes for bacterial cell sensing in which the chemiresistive biosensing mechanism was applied.

4.2 Results of the fabrication of suspended carbon nanowire electrodes

Electrospun polymer fibers should be in the range of 100-200 nm in diameter in order to fabricate sub-100 nm suspended carbon nanowire electrodes. This is because suspended carbon nanowires undergo stretching and thinning reducing diameters to at least 50%. Hence, in this session, optimization of electrospinning parameters was performed to achieve nanowire of this target diameter range. Using the optimized electrospinning parameters, suspended nanowires were electrospun on support structures and selectively crosslinked. Resulting SU-8 structures were then carbonized and resulting morphological changes were observed. The electrical and chemical properties of the suspended carbon nanowires were analyzed.

University of Malaya

4.2.1 Nanofiber fabrication using electromechanical spinning

Patterning of polymer fibers using electromechanical spinning was performed to investigate its ability to pattern sub 100 nm carbon nanowires. Details of equipment setup, operating principles and polymer ink composition are described in the Methodology section 3.3.3. The effects of three main parameters in the electromechanical spinning i.e. voltage, moving stage velocity and polymer composition were investigated. Polymer nanofiber arrays patterned in straight lines with a line gap of 100 µm are shown the Figure 4.1 (a), which demonstrated precision deposition of electromechanical spinning system. However, drawing exact corners in electromechanical spinning remains a challenge as shown in Figure 4.1 (b). There is a time delay of 50-100 ms in execution when the system changes direction at the corner of the patterns. In the meantime, the sustained flow of polymer jet deposition which is repealing itself resulted in flower-like pattern deposition at the corner. Figure 4.1 (c) shows the magnification of a single polymer fiber resulting from electromechanical spinning.

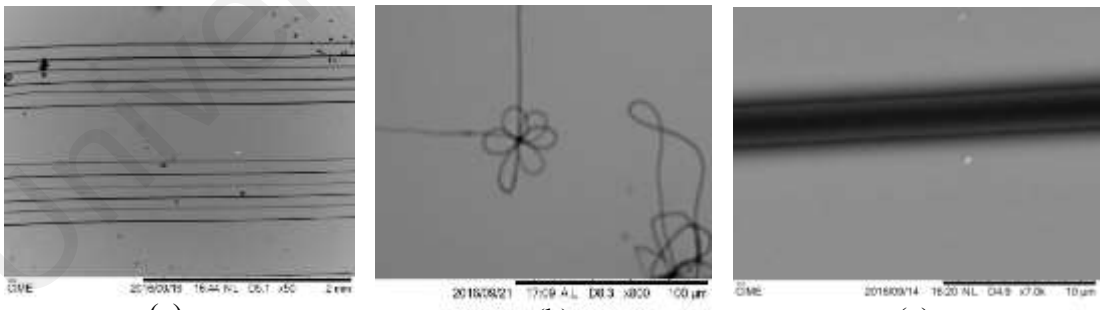

(a) (b) (c)

Figure 4.1: Electromechanical spinning of SU-8 polymer microfibers. (a) Patterned polymer straight lines. (b) Polymer deposition when patterning direction changed. (c) Magnification of an individual polymer fiber.

University of Malaya

4.2.1.1 Effect of voltage on nanofiber diameter

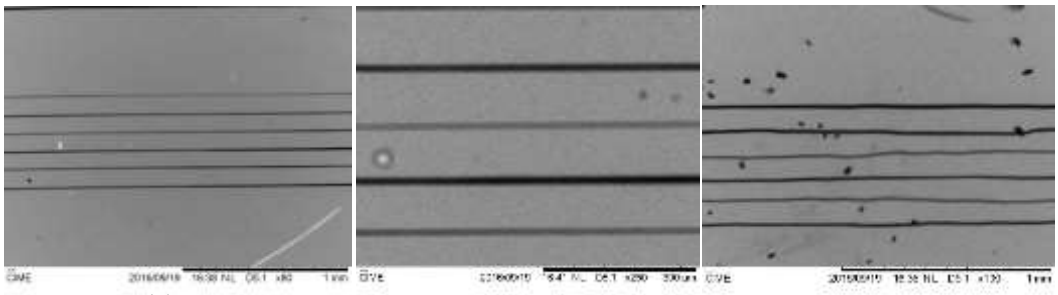

(a) (b) (c)

Figure 4.2: Electromechanical spinning of SU-8 polymer microfibers at different voltages. (a) Fiber deposition at 400V. (b) Magnification of fibers from (a). (c) Jittered deposition at 800V.

Higher voltage operation resulted in an increase in fiber diameter increasing from 9.46 µm at 200 V to 13.05 µm at 800 V. That is opposite to conventional far-field electrospinning in which higher voltage usually gives thinner diameter fibers. Higher voltage produces a higher discharge rate of polymer from the droplet. However, as there is no accompanying a large whipping motion that stretches fibers in the near-field regime, electromechanical spinning at higher voltage resulted in thicker fibers. Moreover, at higher voltage, higher electrostatic repulsion within the polymer jet causes jittering in Figure 4.2 (c). On the other hand, a continuous polymer discharge could not be sustained at a lower applied voltage of 100 V.

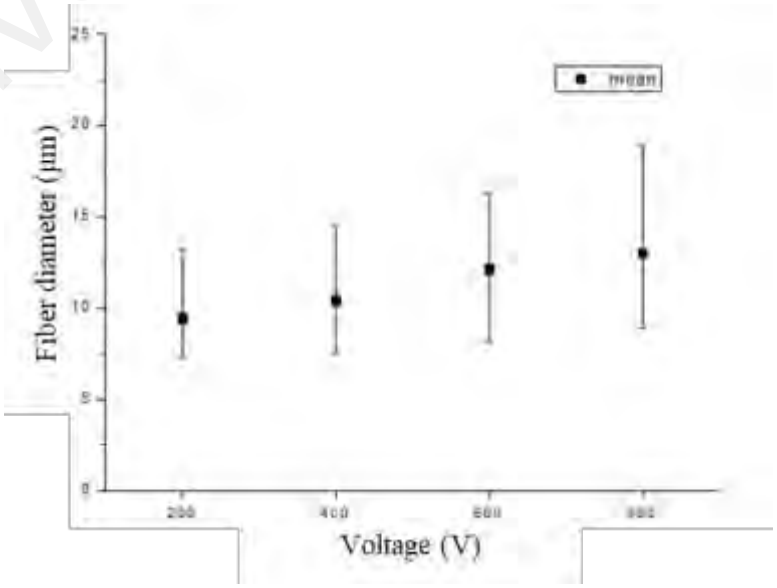

Figure 4.3: Effect of voltage on fiber diameter in electromechanical spinning

University of Malaya

4.2.1.2 Effect of stage velocity on nanofiber diameter

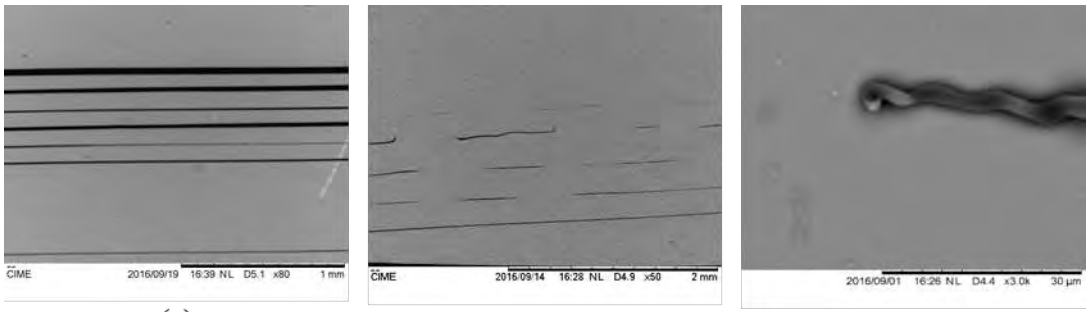

Figure 4.4: Electromechanical spinning of SU-8 polymer microfibers at various stage velocities. (a) Microfiber array where velocity increases from 10 mm/s to 200 mm/s in each successive line from top to bottom. (b) Deposition at a velocity of 300 mm/s (c) magnification of a broken polymer jet at high velocity

Figure 4.4 (a) shows an array of fibers in which each subsequent line has a higher velocity from 10 mm/s to 200 mm/s. The average diameter of fiber reduced from 13 µm to 2 µm as the velocity was increased (Figure 4.5). A moving speed higher than the discharge rate causes the polymer jet to stretch, hence, thinning the fiber in the process. At yet higher velocity, polymer jet broke up as shown the Figure 4.4 (c). The recoil in the broken end of polymer fiber demonstrated that fiber was under a stretching force and undergone plastic deformation. The results showed that the velocity of the moving stage is an effective parameter to obtain thinner fibers in electromechanical spinning.

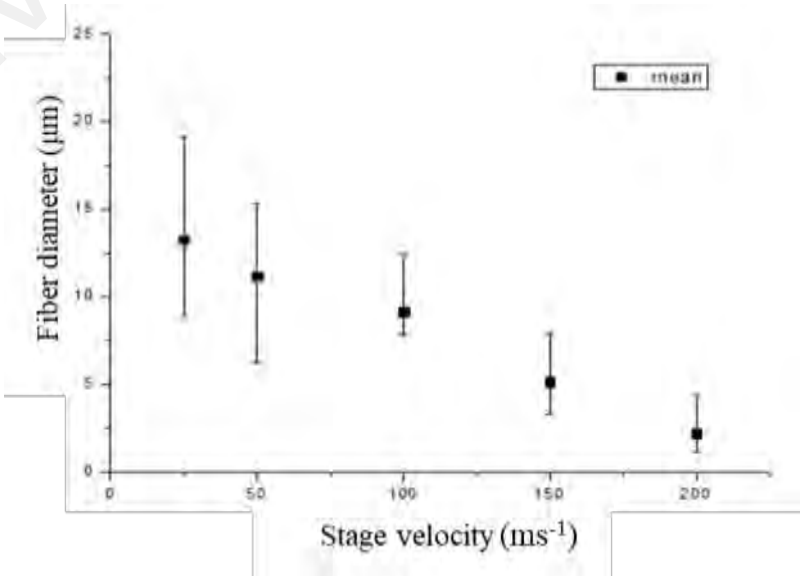

Figure 4.5: Effect of stage velocity on fiber diameter in electromechanical spinning

University of Malaya

4.2.1.3 Effect of polymer ink composition

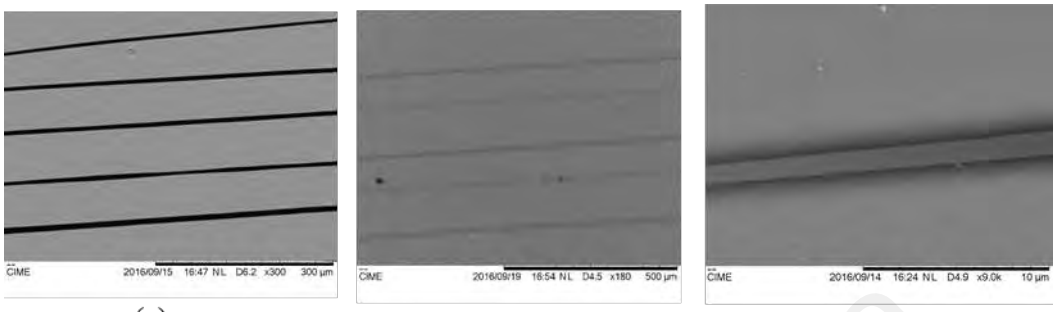

Figure 4.6: Electromechanical spinning of SU-8 polymer microfibers at various polymer composition (a) SU-8 2002 with PEO 0.1% (b) 75% concentration SU-8 2002 with PEO 0.5% (c) a magnified fiber from (b)

As demonstrated above, the stretching of polymer jet is very effective in the thinning of the fiber. As SU-8 has low viscoelasticity, PEO polymer was added to improve viscoelasticity, as higher viscoelasticity could enable higher stretching. In the above experiments, SU-8 2002 with mixed with 0.05% PEO and 0.05% BS4 following the composition developed in a previous study (Giulia Canton, 2014). In this experiment, PEO concentration is increased to 0.1% to enhance viscoelasticity. The experimental results indicate that a higher concentration of PEO results in thicker fibers. Increased stretching in higher velocity did not compensate for the thicker polymer jet discharge from more viscous ink. Hence, a new experiment was carried out on diluted SU-8 formulation. SU-8 was diluted to 75% concentration by mixing it with cyclopentanone solvent. This ink formulation was more promising with fiber diameters reduced to a mean of 1.3 µm from 2 µm in undiluted SU-8. Reducing SU-8 concentration further to 50% made solution viscosity too low to result in fiber deposition.

University of Malaya

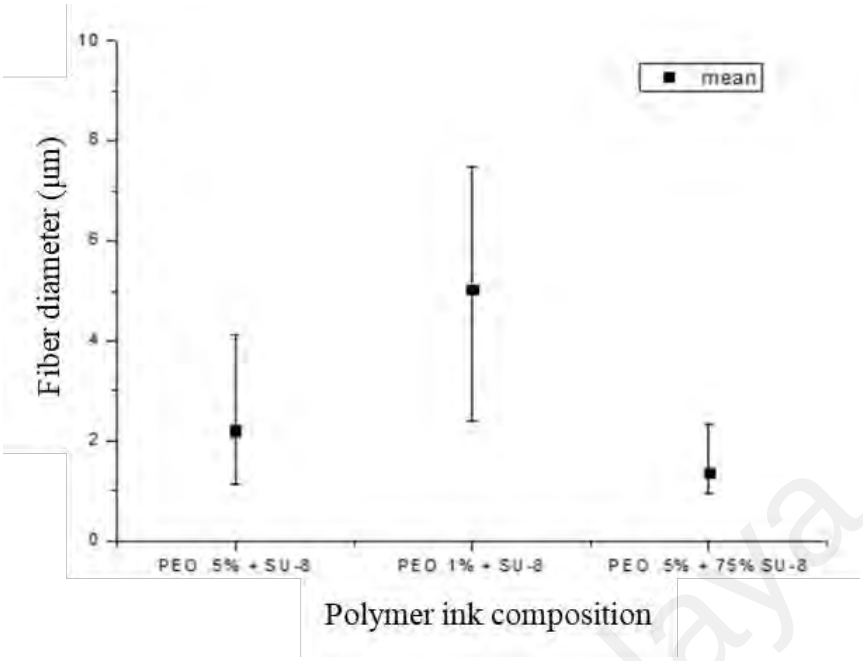

Figure 4.7 : Effect of polymer composition on fiber diameter in electromechanical spinning

4.2.1.4 Integration of electromechanically spun nanofiber on support structures

Using electromechanical spinning, a single fiber was deposited on parallel support structures as shown in Figure 4.8 (a). The polymer fiber was then exposed to UV light for 10 s and then carbonized by pyrolysis and resulting in a 0.97 µm thick fiber was shown in Figure 4.8 (b,c). The thinnest carbon nanofibers obtained using electromechanical spinning was 520 nm in diameter which is more than 218 nm reported previously (Giulia Canton, 2014). Even though this study follows the reported parameters and protocols closely, electromechanical spinning systems used were customized machines with certain key differences. The differences include the syringe pump mechanism (pneumatic syringe pump vs mechanical syringe pump) and polymer jet initiation mechanism (larger diameter of poking tip at 10 µm in this study).

As the electromechanically spun carbon nanofibers did not achieve targeted sub-100 nm range, far-field electrospinning was further investigated for the fabrication of thin carbon nanowires.

University of Malaya

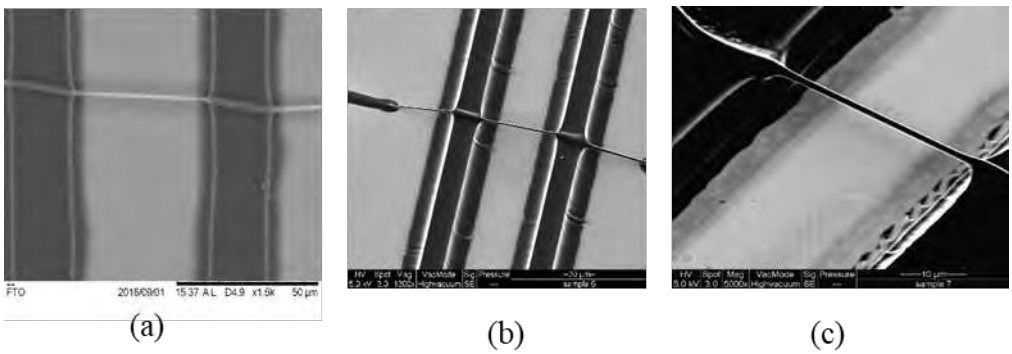

Figure 4.8: A single suspended fiber deposition on support structures from electromechanical spinning. (a) polymer fiber deposition (b) carbon nanofiber after carbonization (c) titled view of nanofiber after carbonization

4.2.2 Nanofiber fabrication using far-field electrospinning

The morphology of polymer fibers resulting from far-field electrospinning can vary widely depending on the electrospinning parameters. The major parameters are process parameters such as needle-to-collector distance, voltage, and flowrate and polymer solution parameters such as solution viscosity and conductivity. First, the effects of individual parameters were investigated by fixing the other parameters as constant. This is to identify the range of electrospinning of SU-8 2015 at various parameters. Based on the results, the best solution parameters were chosen, and process parameters were further fine-tuned in a limited range.

University of Malaya

4.2.2.1 Effect of needle-to-collector distance on fiber morphology

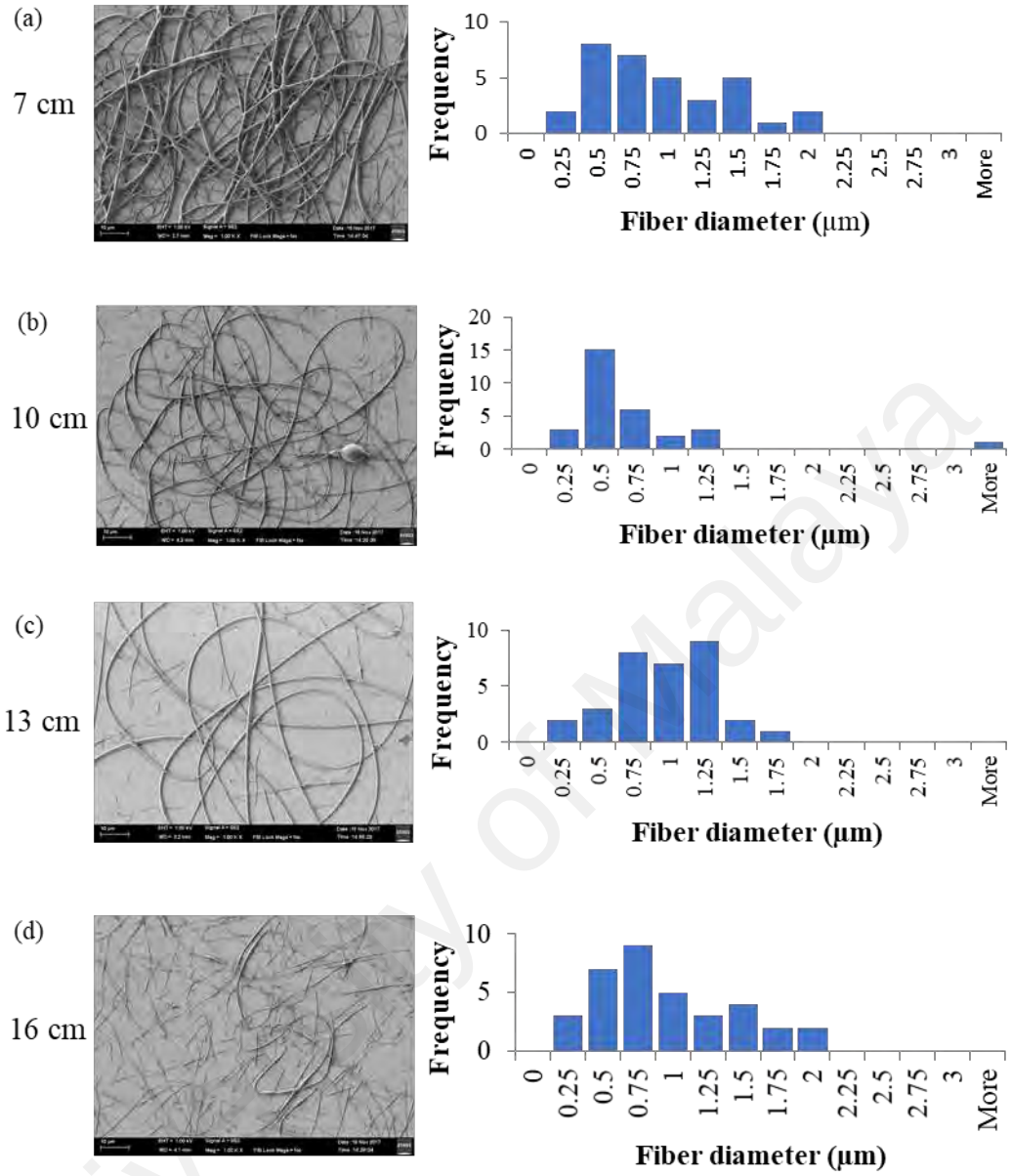

Figure 4.9: Histograms showing fiber diameter distributions at various needle-to-collector distances (a) 7 cm (b) 10 cm (c) 13 cm (d) 16 cm.

The effect of the tip to substrate distance on fiber morphology was investigated by varying the distance to 7 cm, 10 cm, 13 cm, and 16 cm while keeping the voltage and flowrate constant at 8 kV and 12 µL/min, respectively. A 22G diameter needle was used in the experiment. It was found that shorter distance produced thicker and continuous fibers. However, fibers varied in diameters with a combination of thinner and thicker fibers. That is because whipping motion is incomplete at the shorter distances. As the

University of Malaya

distance was increased, the fibers became thinner. However, the deposition of fibers was reduced and hence, the percentage of short strands was increased. This is because heavier thicker fibers were unable to reach the collector plate at a further distance or because longer whipping motion broke up the fibers. At 16 cm, almost all fibers deposited were short strands. As the short strands have spindle shape, the mean and standard deviation of fibers increased.

Table 4.1: Summary of fiber morphology resulting from various distances

Tip to collector distance	Fiber morphology
7 cm	Continuous nanofibers, non-uniform
10 cm	Continuous nanofibers, uniform
13 cm	Continuous nanofibers, uniform
16 cm	Short strands fibers

Table 4.2: Summary of fiber diameter measurement on various needle-to-collector distances

		Tip to collector distance			
		7 cm	10 cm	13 cm	16 cm
Fiber diameter (µm)	Mean	0.831	0.693	0.83	0.832
	SD	0.463	1.104	0.342	0.49
	Min	0.106	0.214	0.204	0.182
	Max	1.783	6.359	1.607	1.994

University of Malaya

4.2.2.2 Effect of voltage on fiber morphology

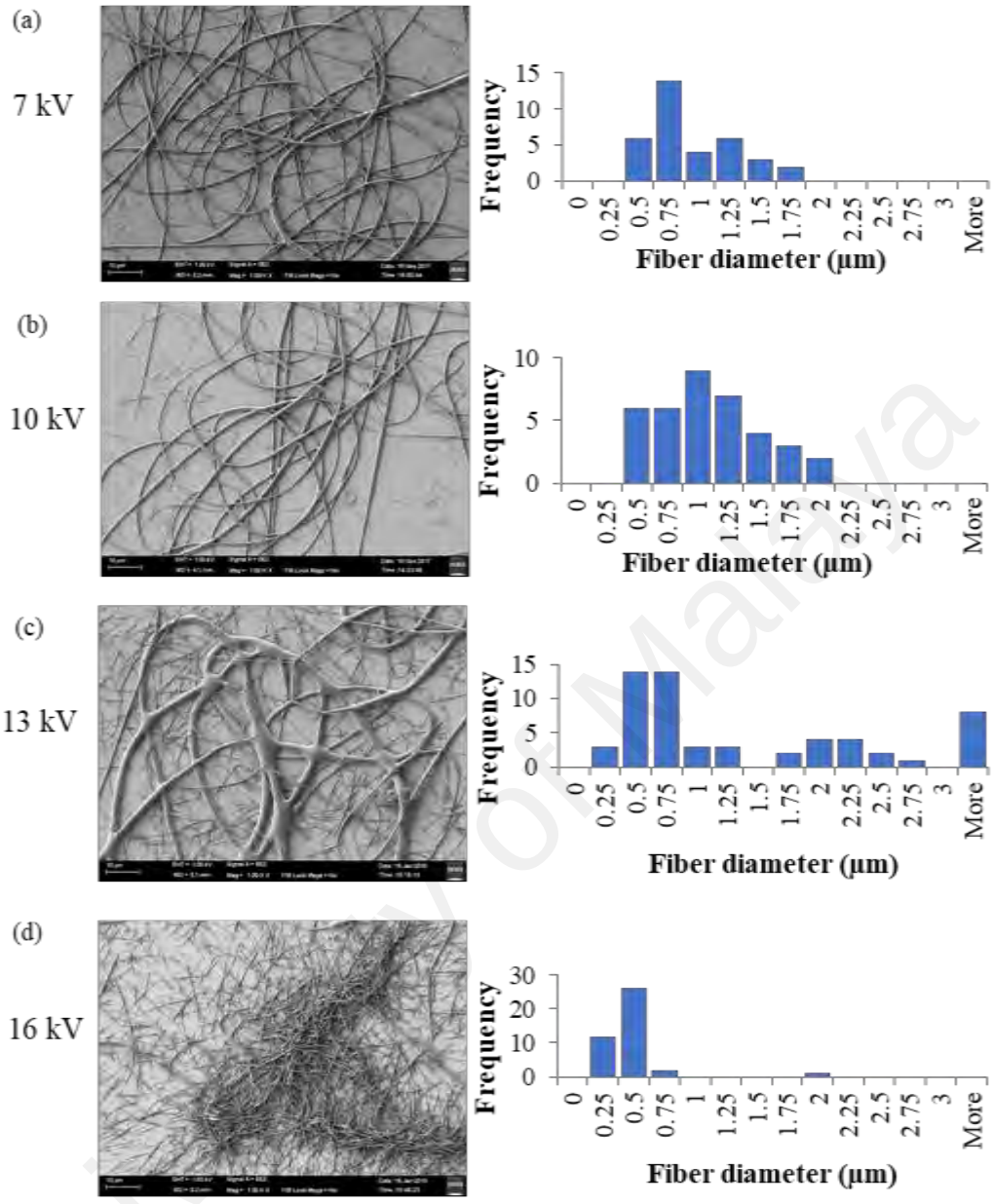

Figure 4.10: Histograms showing fiber diameter distributions at various voltages (a) 7 kV (b) 10 kV (c) 13 kV (d) 16 kV

The effect of voltage is investigated by varying voltage from 7 kV to 16 kV while keeping tip to collector distance at 10 cm and flowrate at 12 µL/min. Distance of 10 cm was chosen based on previous experiment which showed good fiber deposition and fiber dimensions at that distance. A 22G diameter needle was used in the experiment. At 7 kV, deposited fibers are continuous and uniform with most within 500 to 750nm. As the

University of Malaya

voltage increases to 10 kV, fibers increase in diameter and variation, i.e standard deviation increases due to deposition of thin short fiber strands. At 13 kV, variation increases significantly and much thicker fibers with diameter of 2 to 3 μm are found to be interlaced with thin nanofiber short strands of 0.5-1 μm. The variation of fiber diameters observed at higher voltage could be caused by splitting of electrospun jet at higher voltage from two or more Taylor's cones. At 16 kV, only nanofiber short strands were observed. In this case, short strands were formed due to electrostatic repulsion force overcome surface tension that is holding the fiber together.

Table 4.3: Summary of fiber morphology resulting from various voltages

Voltage	Fiber morphology
7 kV	Continuous nanofibers, uniform
10 kV	Continuous nanofibers, uniform
13 kV	Continuous microfibers with beads, uniform nanofibers
16 kV	Short strands nanofibers

Table 4.4: Summary of fiber diameter measurement resulting from various voltages

		Voltage			
		7 kV	10 kV	13 kV	16 kV
Fiber diameter (μm)	Mean	0.8	0.977	1.335	0.374
	SD	0.368	0.425	1.329	0.26
	Min	0.321	0.268	0.143	0.12
	Max	1.744	1.991	7.379	1.825

University of Malaya

4.2.2.3 Effect of flowrate on fiber morphology

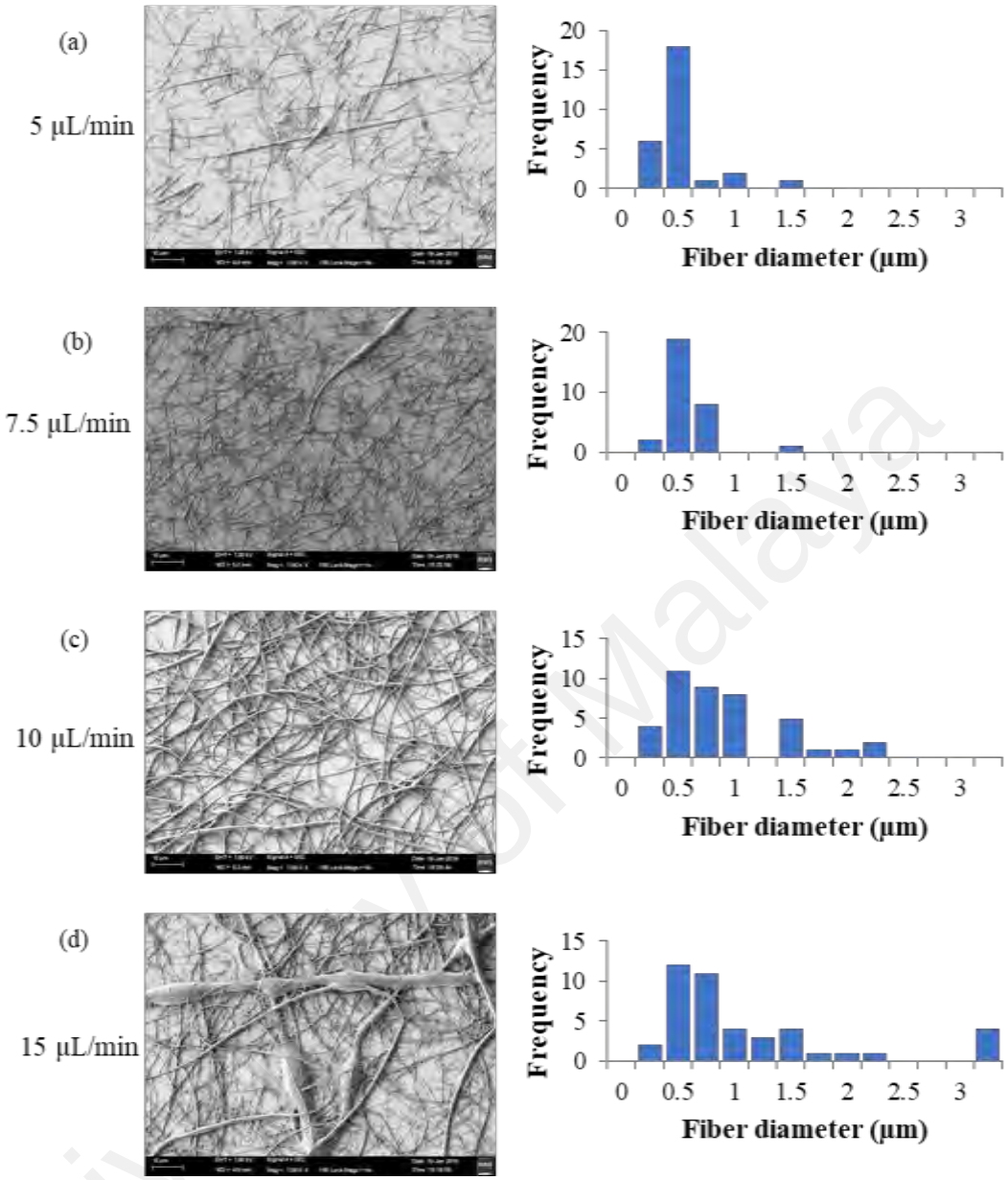

Figure 4.11: Histograms showing fiber diameter distributions at various flowrates (a) 5 µL/min (b) 7.5 µL/min (c) 10 µL/min (d) 15 µL/min.

To study the effect of flowrate on resultant fibers, SU-8 flowrate of 5 µL/min to 15 µL/min was used and fibers were observed for their morphology. Experiments were performed at 10 kV at 10 cm distance as those values were found to produce desired fiber characteristics. A 22G diameter needle was used in the experiment. At low flowrate of 5 µL/min, only short strands of average length of 12 µm were deposited. At 7.5 µL/min, the short strands became longer at average length of 25 µm and diameter of fibers also slightly increased. When the flowrate was increased to 10 µL/min, continuous and

University of Malaya

uniform fibers with increased diameters were deposited. At 15 µL/min, non-uniform micro sized fibers with beads are found to deposit together with thinner fibers. Short strands at lower voltage is caused by a polymer jet ejection rate that is higher than polymer supply rate to Taylor's cone. When the polymer supply rate exceeded the jet ejection rate 15 µL/min, occasional thick fiber jet depositions were obtained.

Table 4.5: Summary of fiber morphology resulting from various flowrates

Flowrate	Fiber morphology
5 µL/min	Short strands nanofibers
7.5 µL/min	Short strands nanofibers
10 µL/min	Continuous nanofibers
15 µL/min	Continuous microfibers with beads, uniform nanofibers

Table 4.6: Summary of fiber diameter measurement resulting from various flowrates

		Flowrate (µL/min)			
		5	7.5	10	15
Fiber diameter (µm)	Mean	0.399	0.449	0.779	1.08
	SD	0.266	0.226	0.491	1.348
	Min	0.163	0.152	0.101	0.248
	Max	1.397	1.418	2.03	6.346

4.2.2.4 Effect of nozzle diameter on fiber morphology

Syringe sizes of 18, 22 and 32 gauge (corresponding to inner diameters of 0.83 mm, 0.41 mm and 0.108 mm respectively) were used in experiments. The experiments were conducted at an operating voltage of 9 kV at 10 cm tip to collector distance for 120 s. The largest diameter of syringe 18 G gives thinnest fibers observed. However, the overall fibers have more variance in size ranging from 0.084 µm to 1.683 µm. The smallest

University of Malaya

diameter nozzle of 32 G syringe gives slightly larger mean diameters at 0.624 μm while 22 G syringe nozzles produce 0.534 μm fibers.

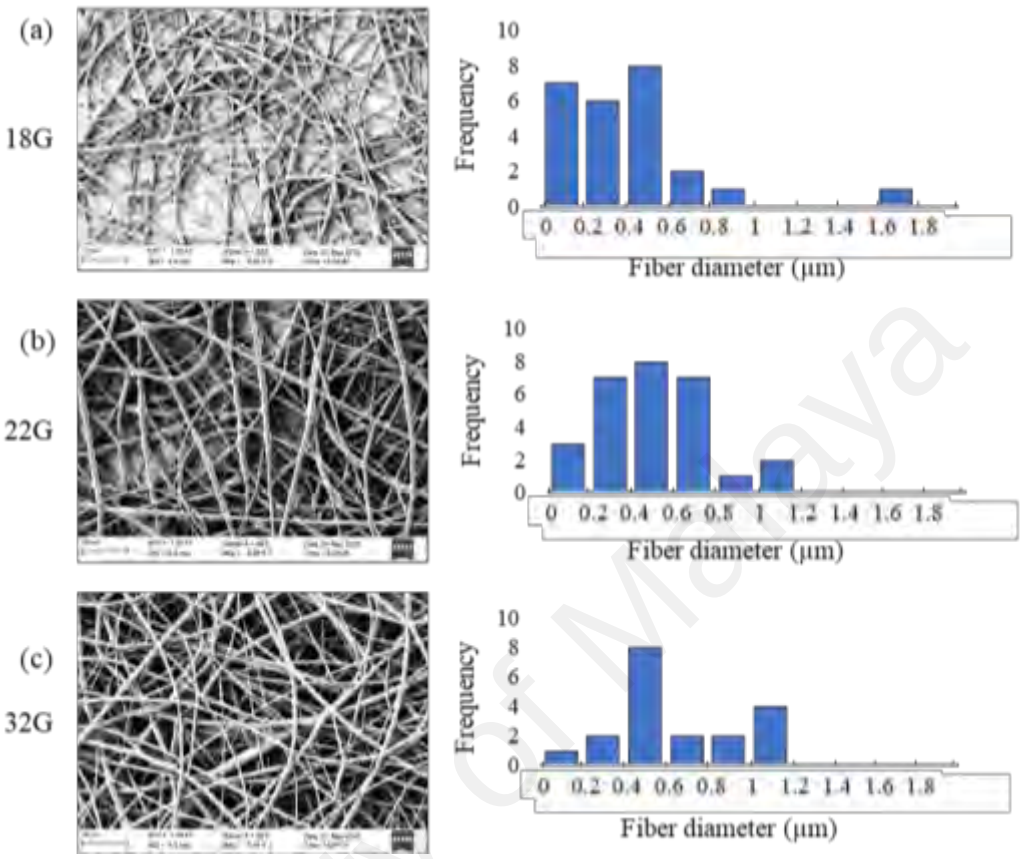

Figure 4.12: FESEM and histograms showing fiber diameter distributions at various syringe diameters (a) 18 G (b) 22 G (c) 32 G

Table 4.7: Summary of fiber morphology resulting from various syringe diameters

Nozzle diameter	Fiber morphology
18 G	Continuous nanofibers
22 G	Continuous nanofibers
32 G	Continuous nanofibers

University of Malaya

Table 4.8: Summary of fiber diameter measurement on various syringe diameters

		Syringe Diameter		
		18G	22G	32G
Fiber diameter (µm)	Mean	0.427	0.534	0.624
	SD	0.33	0.273	0.297
	Min	0.084	0.152	0.181
	Max	1.683	1.197	1.108

4.2.2.5 Effect of solution viscoelasticity

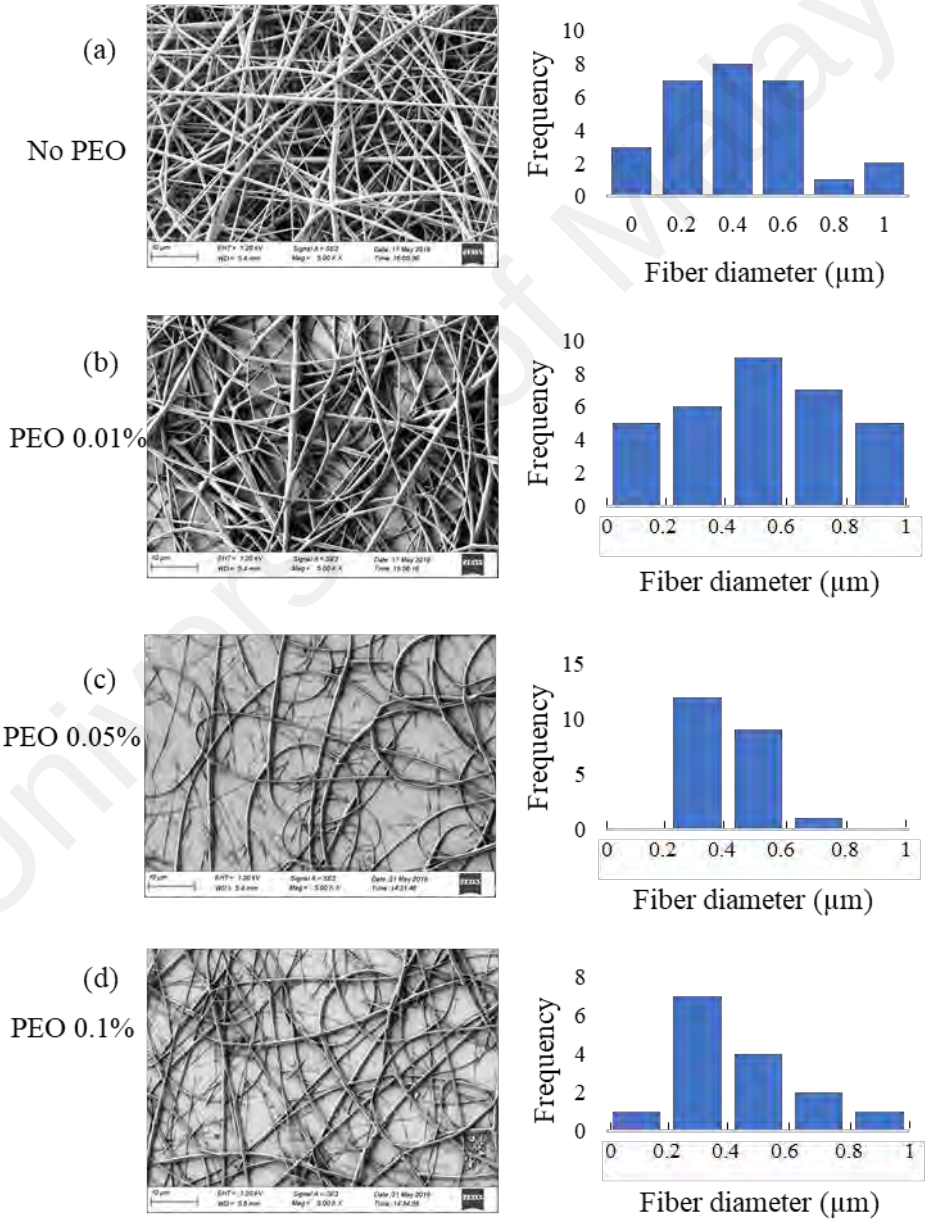

Figure 4.13: FESEM and histograms showing fiber diameter distributions at various PEO concentration (a) no PEO (b) 0.01% (c) 0.05% (d) 0.1%

University of Malaya

The effect of increased viscoelastic properties of SU-8 solution on the resultant fiber diameters was investigated by adding viscoelastic PEO polymer at 0.01%, 0.05% and 0.1 % to SU-8 solution. PEO (400,000 MW) was added to SU-8 2015 and stirred for 24 hr at 45 °C. Experiments were performed at 8 kV at 10 cm distance with a flow rate of 10 µL/min. As the PEO concentration increases, fibers became thinner but spindle-shaped short strands were increasingly produced resulting in decreased uniformity of fibers.

Table 4.9: Summary of fiber morphology resulting from various PEO concentrations

PEO percent	Fiber morphology
No PEO	Continuous nanofibers
PEO 0.01%	Continuous nanofibers, nonuniform
PEO 0.05%	Continuous nanofibers and short strands
PEO 0.1%	Continuous nanofibers and short strands

Table 4.10: Summary of fiber diameter measurement on various PEO concentrations

		PEO percent			
		0	0.01%	0.05%	0.10%
Fiber diameter (µm)	Mean	0.534	0.54	0.39	0.416
	SD	0.273	0.3	0.126	0.181
	Min	0.152	0.106	0.207	0.186
	Max	1.197	1.361	0.636	0.81

4.2.2.6 Effect of solution conductivity

The increased conductivity of the solution is associated with smaller diameters in the literature. Here, the effect of solution conductivity was investigated by adding conductive salt (0.01, 0.5% and 0.1 %) to SU-8 2015. Experiments were performed at 8 kV at 10 cm distance with a flow rate of 10 µL/min. Increased conductivity generally results in thinner

University of Malaya

diameter fibers, but it is found to break up the fibers to short strands (spindles) as shown in the figure. At 0.1% concentration, there is no continuous fiber formation and spindles become shorter. This is because increased electrostatics forces introduced by conductive salts overcomes surface tension that is maintaining polymer in jet form. Hence, the increased conductivity of solution gave results similar to high voltage and is not useful for the fabrication of thinner fibers in SU-8 polymer.

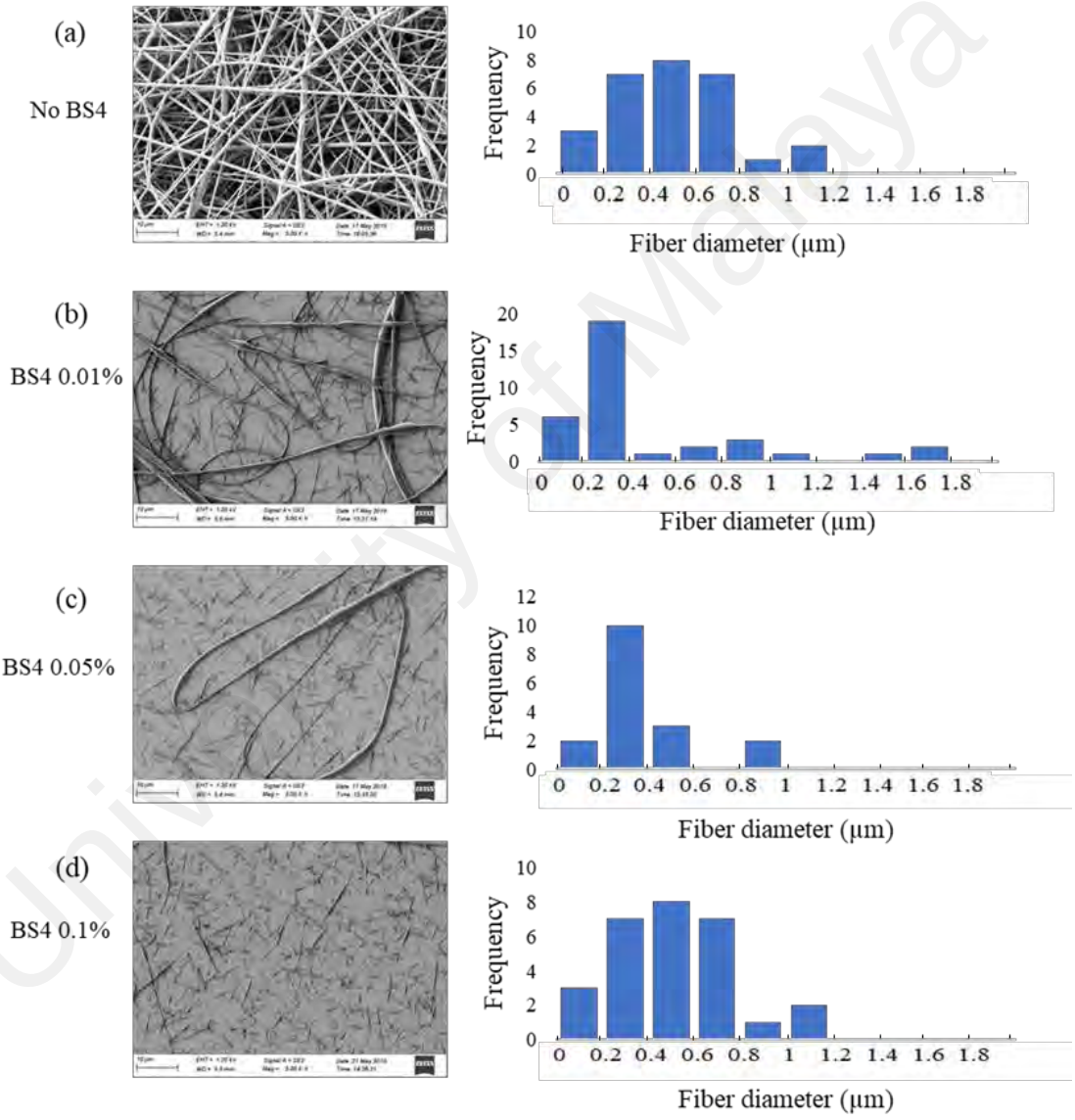

Figure 4.14: FESEM and histograms showing fiber diameter distributions at various BS4 concentration (a) no BS4 (b) 0.01% (c) 0.05% (d) 0.1%

University of Malaya

Table 4.11: Summary of fiber morphology resulting from various BS4 concentrations

BS4 percent	Fiber morphology
No BS4	Continuous nanofibers, uniform
BS4 0.01%	Short strands and continuous nanofibers
BS4 0.05%	Mostly short strands
BS4 0.1%	Short strands

Table 4.12: Summary of fiber diameter measurement on various BS4 concentrations

		BS4 percentage			
		0	0.01%	0.05%	0.10%
Fiber diameter (µm)	Mean	0.534	0.465	0.382	0.274
	SD	0.273	0.434	0.24	0.142
	Min	0.152	0.084	0.107	0.107
	Max	1.197	1.719	0.951	0.552

4.2.2.7 Fine-tuning far-field electrospinning parameters

Using the above results of the individual parameters, further fine-tuning of electrospinning was performed by varying the voltage and distance while keeping flowrate constant. Increasing conductivity and viscoelasticity of SU8-2015 were ruled out as they did not result in thin uniform continuous nanofibers as previously discussed. Syringe needle diameter of 22 G was selected as it gave more uniform and thinner fibers. The flow rate of 10 µL/min was also selected based on the results. Then, the voltage range of 8 kV to 14 kV and the needle-to collector distance range of 7.5 cm to 15 cm were used as variable parameters and results were demonstrated in Figure 4.15 . Needle-to-collector distance less than 10 cm resulted in occasional large polymer droplet depositing on the silicon substrate. A voltage greater than 12kV produced spindle-shaped short strands instead of cylindrical wires. The finest and most uniform nanofibers were

University of Malaya

deposited at a voltage of 12 kV with a needle-to-collector distance of 10 cm at a flow rate of 10 µL/min, resulting in average fiber diameter of 275 nm with a standard deviation of 96 nm. These parameters were used to synthesize suspended nanofibers in subsequent fabrication steps. During the experiments, humidity ranges from 45 to 55 % relative humidity.

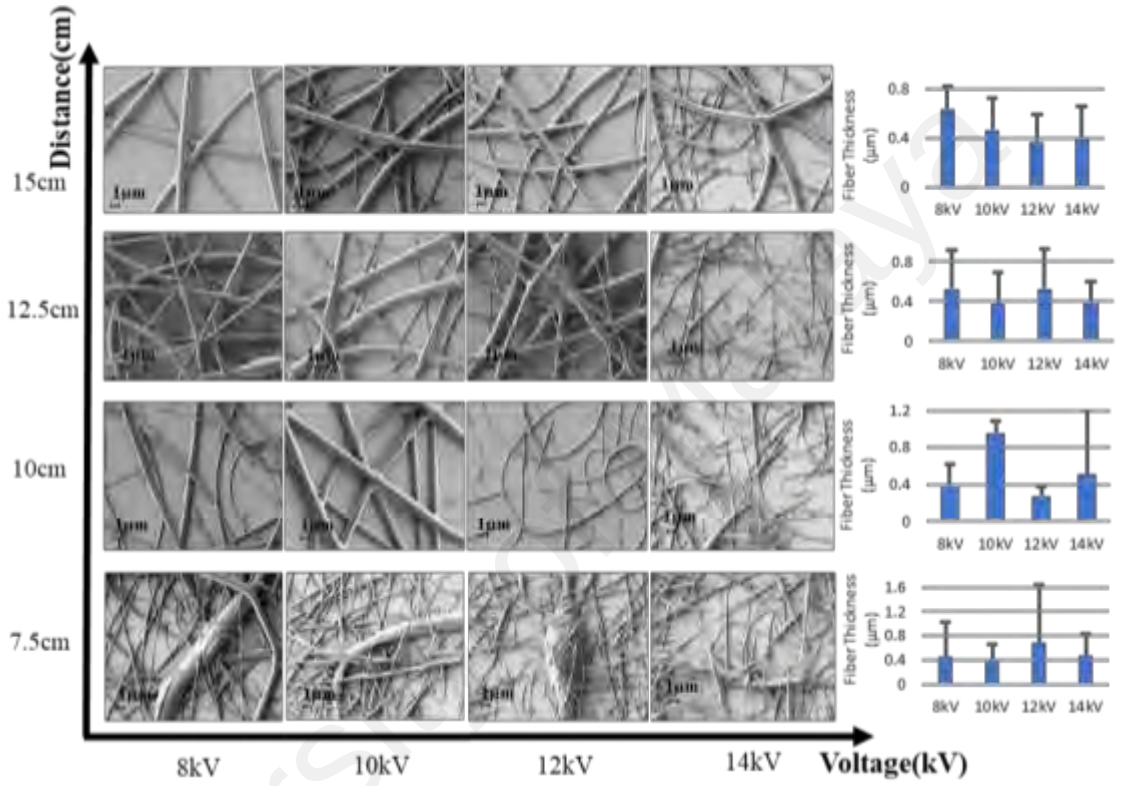

Figure 4.15: Optimization of electrospinning parameters of voltage and distance between needle and collector at the flow rate of 10 µL/min.

4.2.3 Photolithography of SU-8 support structures

SU-8 were spin-coated to various heights 60, 40, 20, and 10 µm by varying rotation speed as described in the manufacturer's datasheet. Then electrode pair support structures were fabricated by photolithography process as described in the methodology. The process has different parameters (e.g. varying pre-bake, exposure and post-bake time) which depend on the spin-coated height and different SU-8 viscosity. UV exposure was performed with vacuum contact mode between the photomask and SU-8 coated wafer. Examples of the pattern after the development process at varying heights is described in Figure 4.16, in which features have a width of 20 µm and a gap of 10 µm between parallel

pairs and between tips. At the height of 60 μm, the gaps did not appear after development with a slight depression trace between the tips. At the height of 40 μm, the gap between tips could be seen. However, the parallel electrodes are fully attached to the side. The gaps appear more prominent at the height of 20 μm, but slightly attached at the base as can be seen in the black region between electrodes. No amount of further developing time or ultrasonication in SU-8 developer increased the resulting gap. This showed that structures are totally crosslinked. Structures of 10 μm height showed complete development with clear gaps both at the side and the top. By varying the photolithography parameters from a recommendation in the datasheet, a clear 10 μm pattern gaps can be obtained to the structure height of 20 μm. To achieve this, soft-bake and post-bake time must be increased by ~15% while reducing exposure time to approximately 20 % of the recommended duration. This experiment showed that even though SU-8 is a high aspect ratio photoresist, the actual resolution and heights that can be produced is limited by photolithography equipment and techniques. Hence, the fine-tuning of photolithography parameters is required for higher structures with narrow gaps.

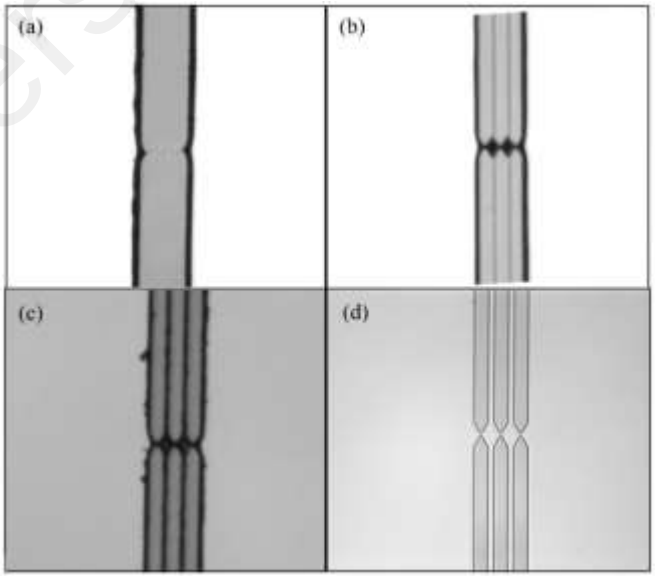

Figure 4.16: Dependence of various spin-coating heights on pattern resolution. (a) 60 μm, (b) 40 μm, (c) 20 μm, and (d) 10 μm.

University of Malaya

4.2.4 Integration of electrospun polymer fibers on support structures

Polymer support structures for suspended nanowires were fabricated on silicon wafers by C-MEMS techniques with each wafer containing 24 chips. Electrospun fiber mat was then deposited on the silicon wafer using optimized electrospinning parameters for 1 min. The wafer was then vacuum dry for 1 hr. Second stage photolithography was then performed with UV exposure at the gap in between support structures to selectively crosslink suspended nanofibers. After heat treatment to complete crosslinking wafers were immersed in SU-8 developer for 1 min followed by rinsing with isopropanol and drying in the oven.

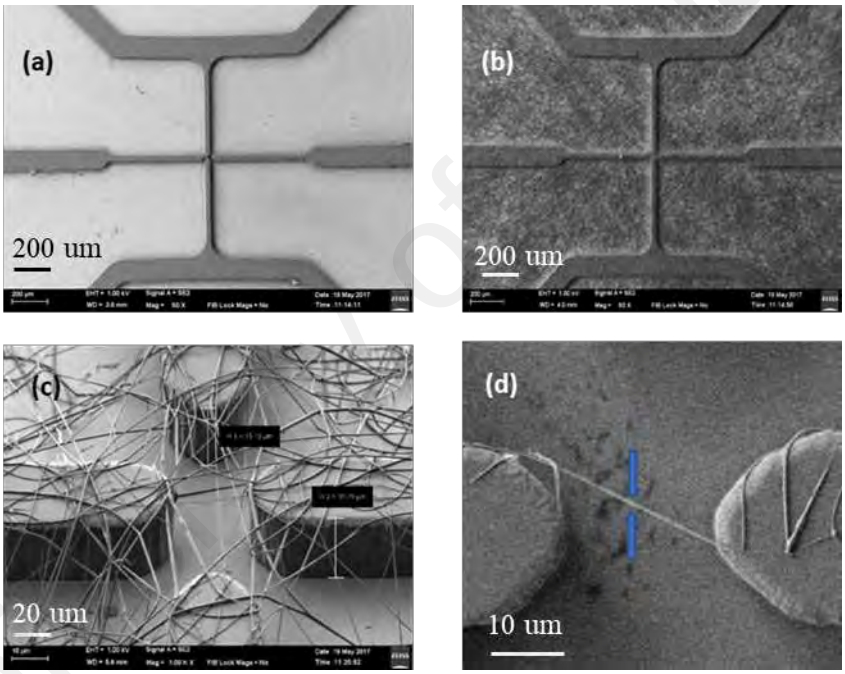

Figure 4.17: Fabrication of suspended polymer nanofibers. (a) Polymer support structure produced by C-MEMS. (b) Electrospun fiber mat on a support structure. (c) Magnification of fiber mat at the center (d) After selective crosslinking of nanofibers between support structure.

When electrospinning was performed on whole silicon wafer, suspended fibers were obtained in 19 to 20 electrodes with patterns on the edge of wafer sometimes failed to receive nanowire deposition. This translates to a yield of approximately 80% of suspended nanowire deposition in 5 repetitions of the experiment. Among these, approximately 20% results in single nanowire suspension, while two to a maximum of

three nanofibers were deposited in the rest. The maximum number of nanowires observed is three. The chips with no usable suspension were discarded.

4.2.5 Support structures after pyrolysis

SU-8 structures undergo considerable deformation and shrinkage after pyrolysis as shown in Figure 4.18. At the bottom of structures, the photoresist is bonded to the silicon wafer substrate, and hence, there is no shrinkage after pyrolysis. Lateral shrinkage occurs maximum at the top resulting in wedge shape carbon structures. A representation of the shrinkage of support structures is shown in Figure 4.18 with the corresponding measurement in Table: 4.13. The support structures resulted in a general lateral offset of approximately 10 μm from all directions resulting in a 50% shrinkage of support structure width.

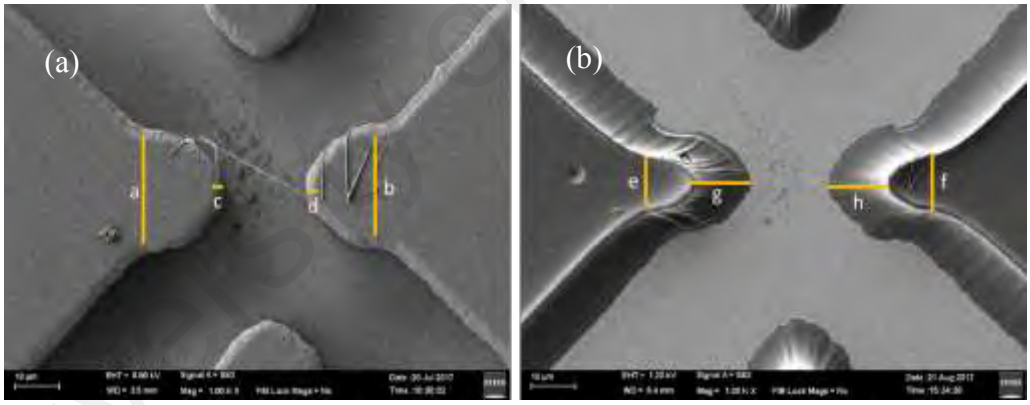

Figure 4.18: SU-8 structures before pyrolysis (a) and Carbon structures after pyrolysis (b). Labels indicate distance measurements described in Table 4.13.

Table 4.13: Measurements of structural dimensions before and after pyrolysis of Figure 4.18

Before Pyrolysis		After Pyrolysis	
Label	**Distance (μm)**	**Label**	**Distance (μm)**
a	21.16	**e**	10.435
b	21.405	**f**	11.304
c	2.174	**g**	13.043
d	1.745	**h**	13.489

University of Malaya

4.2.6 Suspended carbon nanowires after pyrolysis

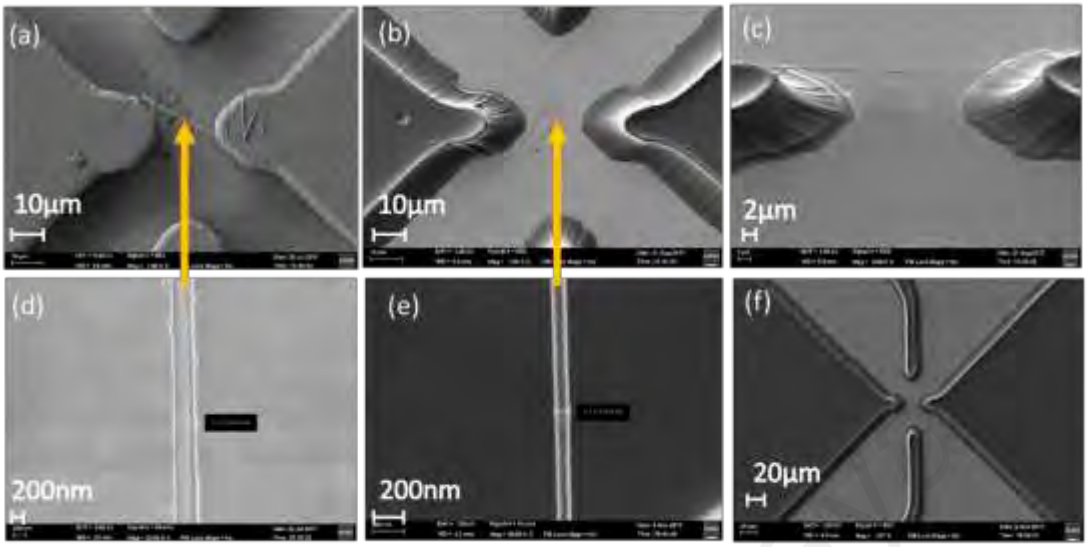

Figure 4.19 (a) SU-8 nanowire suspended on supporting structures before pyrolysis (b) carbon nanowire on supporting carbon structures after pyrolysis. (c) Titled view of structures showing carbon nanowire suspension. (d) an individual SU-8 nanowire (e) carbon nanowire after pyrolysis. (f) Zoomed out view of the electrode.

The evolution of a polymer nanofiber to a carbon nanowire sensor is illustrated in Figure 4.19. Upon pyrolysis, the supporting structures shrank at the top while the bottom retains the original size as can be observed from the tilted view of an electrode. This shrinkage of support structure mechanically stretched nanowire during pyrolysis making it longer and thinner. Suspended nanowire shrank to an average of 67% in diameter during pyrolysis. Diameter shrinkage (D%) is calculated as:

$$D\% = \frac{d_i - d_f}{d_f} \tag{4.1}$$

where d_i is the initial diameter of polymer nanowire and d_f is final diameter after pyrolysis.

The gap between support structures increased from 20 µm to 40 µm after pyrolysis due to shrinkage at the top. This stretches nanowire and its length increased 100% approximately. As fabricated, carbon nanowires are found to have an average diameter of 84 nm ± 29 nm with the height of suspension at 10 µm as measured from the

University of Malaya

micrograph. The smallest diameter observed in this study was 42.95 nm shown in Figure 4.20 (c). From FESEM observation, all suspended polymer nanofibers survive pyrolysis and form carbon nanowires without detaching or breaking.

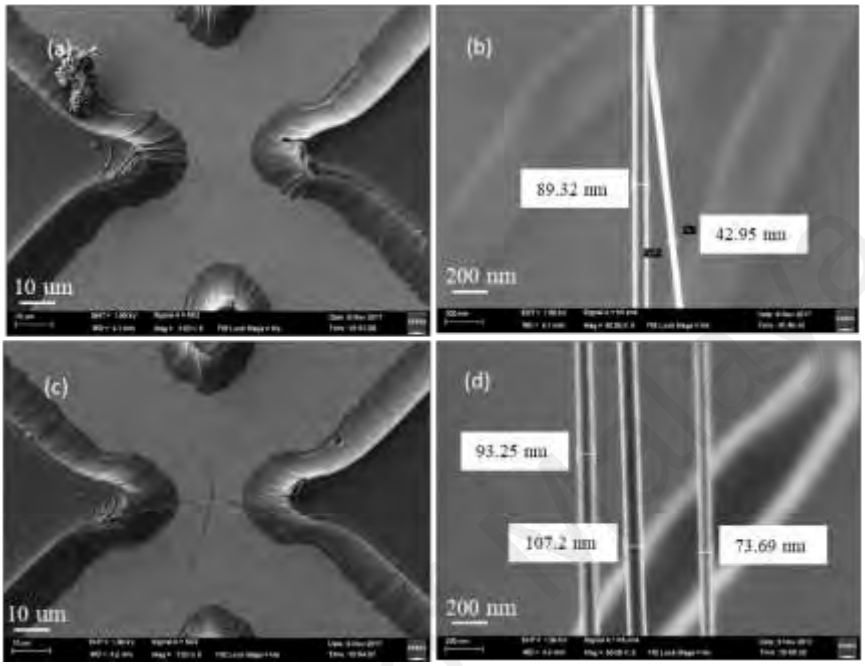

Figure 4.20: Examples of multiple carbon nanowire suspensions (a) and (c) show top view of the nanowires on support structures. (b) and (d) show magnification of nanowires from (a) and (b), respectively.

4.2.7 Electrical properties characterization of suspended carbon nanowires

To study the electrical characteristics of single nanowires, SEM was used to select chips with a single nanowire of sub-100 nm diameter. Source measure unit probes were positioned on support structures near to nanowires. The maximum current is limited to 10 µA to limit Joule's heating on nanowires. The conductivity of nanowires was obtained from the nanowire dimension obtained from micrographs and resistance obtained from current-voltage (I-V) measurement. The nanowires show carbon to carbon ohmic contact with a linear I-V curve as shown in Figure 4.21. The conductivity of nanowire (σ) can be calculated by

$$\sigma = \frac{1}{\rho} = \frac{l}{R \cdot A} \tag{4.2}$$

Where ρ is resistivity, l is the length, R is resistance and A is the cross-sectional area of the nanowire.

The average conductivity of suspended nanowires was 3.48×10^4 S/m $\pm 0.7 \times 10^4$ as measured in 8 samples. In order to calculate resistivity of carbon support structures, flat rectangle carbon structures were fabricated with a width of 0.5 mm, length of 10 mm and thickness of 15 μm. SMU probes were positioned at the wide edge of structures. The conductivity of flat carbon structures was measured to be 1.67×10^4 S/m $\pm$ 0.46×10^4. Hence, nanowires showed higher conductivity than typical C-MEMS structures. This increased conductivity seen in nanowires indicates that there are more graphitic components in the suspended nanowires. It has been previously hypothesized that mechanical stretching of SU-8 polymer fibers during electrospinning and during pyrolysis untangle the carbon chains arranging them into more graphitic sheets (S. Sharma et al., 2012).

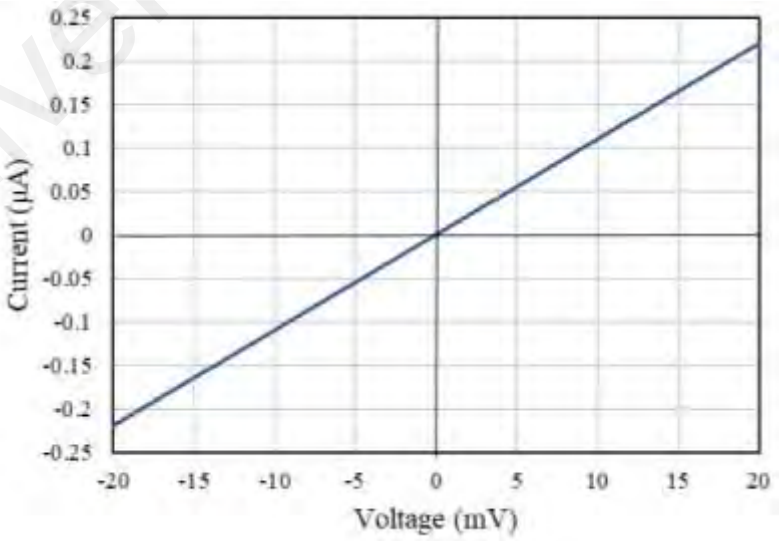

Figure 4.21 : Typical I-V curve of suspended carbon nanowire

University of Malaya

4.2.8 Chemical properties characterizations of pyrolyzed carbon nanofibers

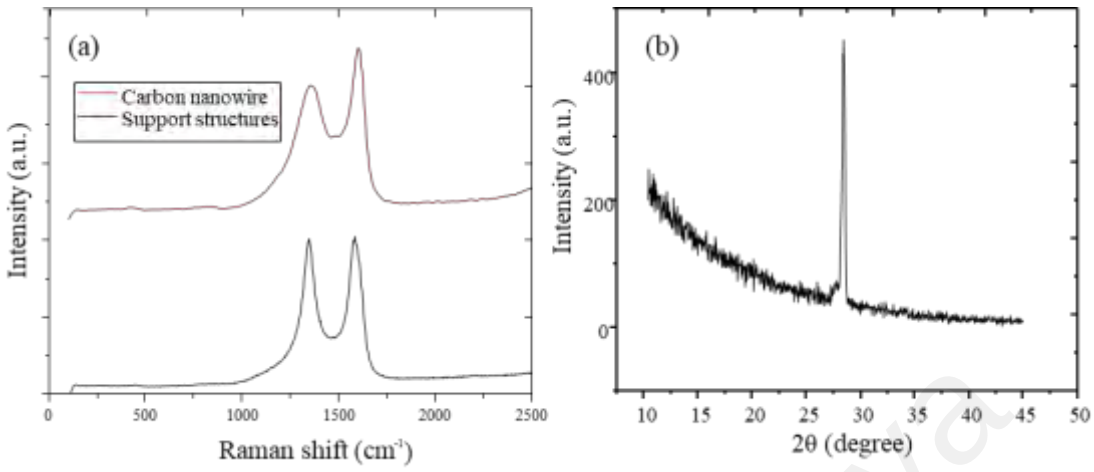

Figure 4.22 : (a) Raman and (b) XRD spectrum of pyrolyzed carbon nanofibers.

Raman measurement was performed on suspended carbon nanowires as well as support structures. XRD measurement was performed on electrospun nanofiber mats on a silicon wafer as the instrument is not capable of targeting microsized suspended nanowires. Raman spectrum displays two main peaks between 1200 and 1700 $cm^{-1,}$ which are characteristic features of graphitic carbons, as shown in Figure 4.22 (a). The peak at around 1600 cm^{-1} is called the graphitic G band. The peak at around 1350 cm^{-1} is called disorder-induced D band and is not observed for single-crystal perfect graphite. The ratio of intensities I_D/I_G in suspended nanowires is 0.77 compared to 0.99 in support structures, indicating increased graphitization of suspended carbon nanowires. The XRD result of nanowires (Figure 4.22 (b)), again, shows a peak at ~28˚ which is typical of (002) plane graphitic carbon. Raman and XRD observations indicated that electrospun nanofibers were composed of semi-graphitic sp2 carbon content. The results observed here showing more graphitic nature of suspended nanowire is in line with recent studies that used stress-induced approach to make pyrolytic carbon more graphitic by aligning polymer chains in nanofibers (Ghazinejad, Holmberg, Pilloni, Oropeza-Ramos, & Madou, 2017; Holmberg et al., 2018). In the aforementioned studies, mechanical force was applied to electrospun fiber mat to stretch the fibers and prevent the polymer chains

University of Malaya

from coiling up and becoming fullerene-like structures. On the other hand, in this research, mechanical force developed on suspended nanowires during pyrolysis process due to shrinkage of support structures.

4.3 Results of the surface functionalization of carbon electrodes

4.3.1 Acid and electrochemical treatments

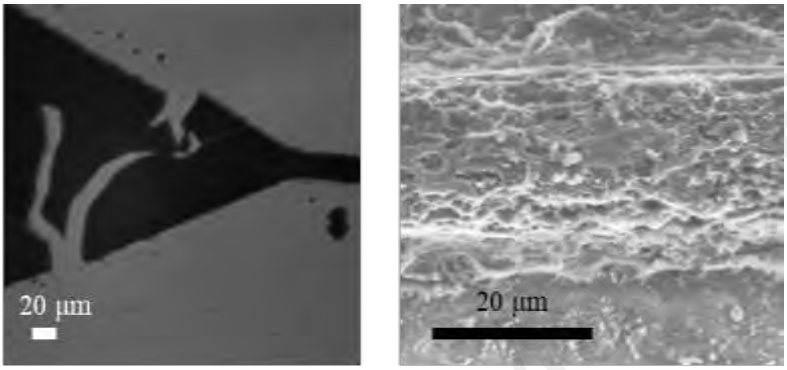

Figure 4.23: Micrograph of C-MEMS structures after (a) strong acid treatment and (b) electrochemical oxidation treatment

Various strong acid and electrochemical oxidation treatments were performed on carbon electrodes with protocols described in Methodology section 3.4. Carbon structures exposed to all the acids either resulted in damage or detached from silicon wafers, as shown in Figure 4.23 (a). On the other hand, electrochemical oxidation resulted in the etching of the surface layer resulting in microporous formation observed under the FESEM micrograph in Figure 4.23 (b). Hence, the electrodes were discarded and were not used in further surface characterization.

Efforts were focused on non-destructive surface functionalization using novel microplasma direct writing. However, the porous nature of electrode surfaces found after electrochemical treatment holds the promise of better electrochemical sensors and energy storage electrodes due to their enhanced surface area.

University of Malaya

4.3.2 Microplasma direct-writing

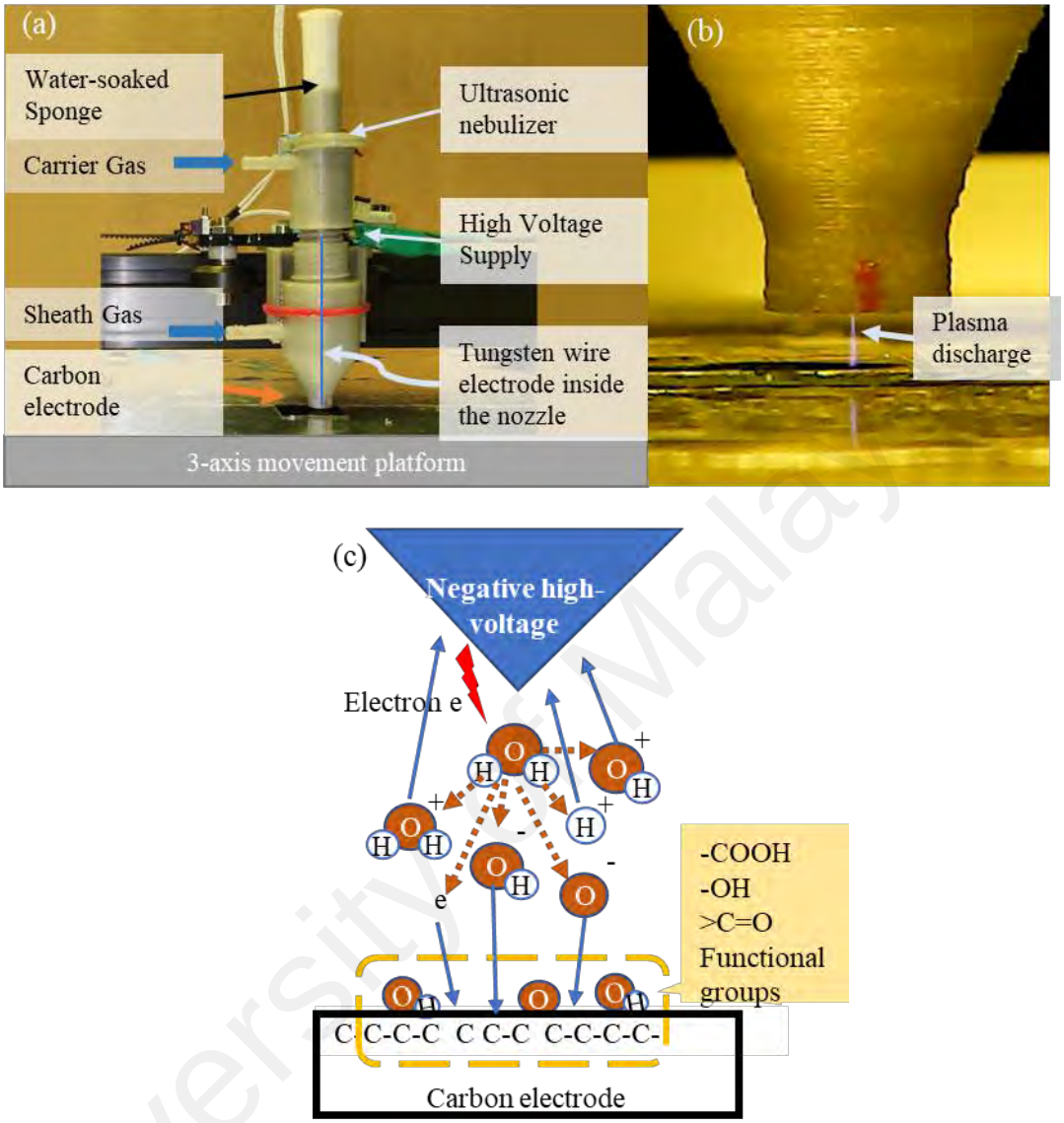

Figure 4.24: Plasma direct-writing system experimental setup. (a) Plasma direct-writing nozzle system. (b) Plasma streamer (filamentary discharge) from the nozzle to a carbon electrode on a silicon wafer. (c) Schematic representation of water molecules ionization mechanism and surface functionalization of carbon electrode.

The experimental plasma direct writing setup is shown in Figure 4.24. It was composed of a tungsten microelectrode tip, a high voltage RF voltage supply, a water atomizer, and a 3-axis motion control platform. The tungsten microelectrode (100 μm diameter) generates a filamentary plasma discharge (plasma streamer) when excited by

University of Malaya

radio frequency high voltage source, while piezoelectric nebulizer provides water vapor source to the plasma streamer. The operational details of the set-up were described in the methodology. A carbon electrode of a 10 μm thick carbon microfilm is positioned on the conductive platform. The plasma discharge ionizes water molecules to H_2O^+, OH^+, H^+, OH^-, O^- and H^- ions (Nakamura et al., 2019; Smyth & Mueller, 1933) . The plasma discharge can be either positive or negative streamers depending on the biasing of the voltage source to the tungsten microelectrode. The resulting ions and electrons bombard the carbon electrode surface, breaking carbon to carbon bonds and creating C-OH and C-O-OH bonds in the process.

Figure 4.25 (a) shows a schematic of the plasma microelectrode movement direction during patterning. An optical image of the pattern on the carbon film electrode is presented in Figure 4.25 (b). From the EDS measurements, positive plasma writing was found to result in a slight increase of oxygen functional groups (from ~5 to ~6 %) on the surface. The EDS analysis also reveals the presence of tungsten (~1%) on the carbon surface, which indicates some decomposition of the tungsten plasma electrode. Tungsten is absent in a negative streamer treated surface. This is because tungsten ionizes into positive ions. Figure 4.25 also shows the comparison between the direct-writing by positive- and negative-plasma streamers on pyrolyzed carbon films. The positive ions treatment resulted in microdots on the carbon surface (Figure 4.25 (c)). Upon higher magnification, those microdots reveal micro flower-like branching patterns (Figure 4.25 (d)), also known as Lichtenberg figures (Merrill & Hippel, 1939). These patterns indicate the dielectric breakdown of the carbon material. It has been shown experimentally that a water plasma contains a much higher density of positive ions (mostly H_2O^+) compared to negative ions (OH^-) (Nakamura et al., 2019; Smyth & Mueller, 1933). Hence, the positive streamer with its higher ion concentration yields higher currents causing the

University of Malaya

electrical breakdown. These patterns were also observed with a negative plasma when the plasma progresses into an arc discharge.

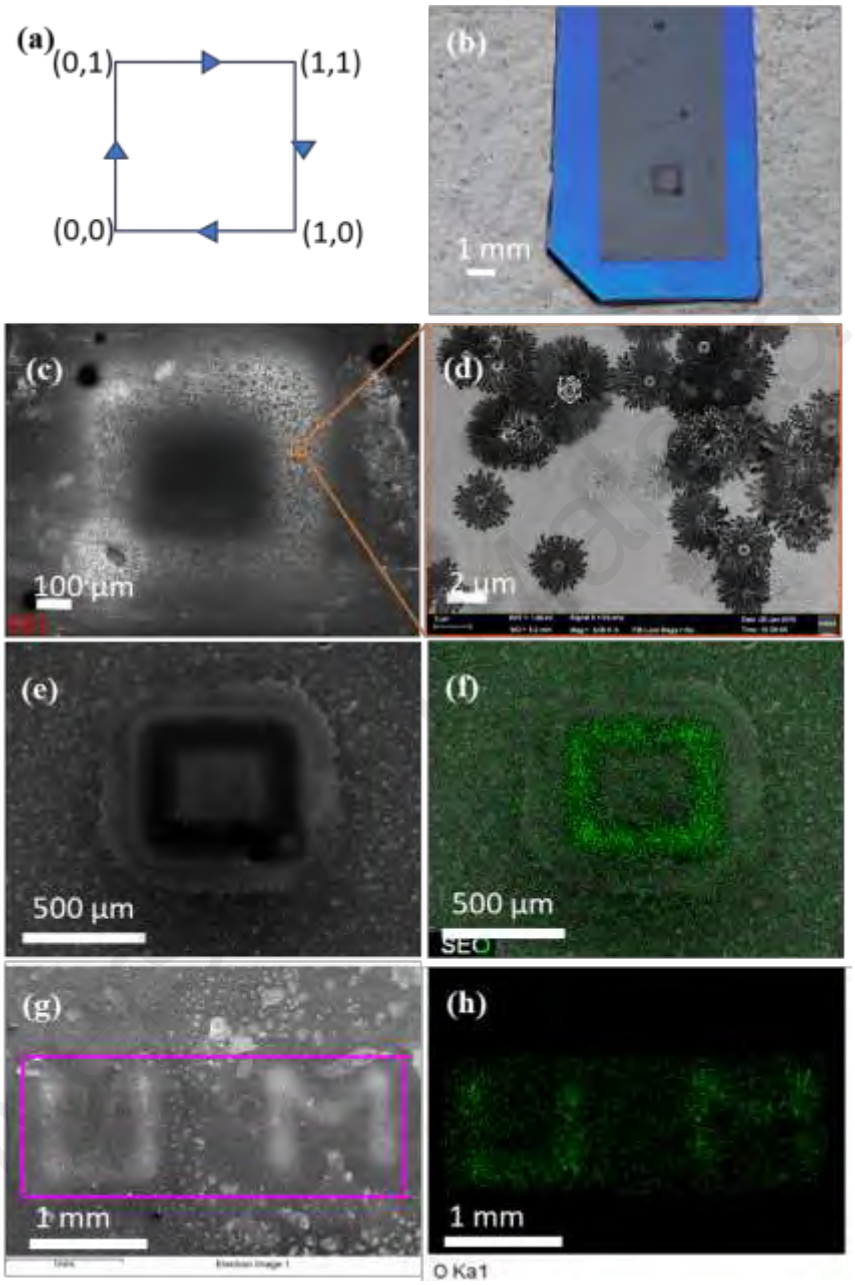

Figure 4.25: FESEM and EDS micrographs of direct-writing patterns. (a) Schematic diagram showing programmed tip movement direction of plasma direct-writing of 1mm square. (b) Optical image of carbon film electrode showing plasma-treated patterns. (c) FESEM image showing direct-writing of a 500 µm square pattern with a positive plasma streamer. (d) Magnification of a treated area from (c) showing flower-like patterns (e) FESEM image showing plasma direct-writing of 500 µm square with a negative plasma streamer. (f) EDS elemental mapping of oxygen superimposed on the image (e) (g) An arbitrary pattern "UM" drawn with negative plasma direct writing. (h) EDS elemental mapping of oxygen from (g)

As the reactivity of the plasma depends on the streamer current density, the high current positive plasma streamers and high current electric arcs have an etching effect on the carbon electrode revealing the underlying silicon substrate. By limiting the plasma current with a high impedance load, the negative corona streamer discharge can be stabilized to prevent it from progressing into an arc discharge. Using negative plasma direct-writing, fine patterns of oxygen groups can be written as shown in Figure 4.25 (e-h)). Accompanying EDS elemental maps confirm the patterns of oxygen functionalities in the plasma direct-written areas.

4.3.3 Improvement of oxygen functionalities

In microplasma direct writing, the plasma streamer passes over a spot many times during a functionalization treatment. Hence, the overall process time does not represent the total exposure time of a treated area, unlike in conventional plasma treatment. Here, the exposure was measured by the number of writing scans during treatment. In all experiments, the plasma scan rate is 400 $mm \cdot min^{-1}$ (6.67 $mm \cdot s^{-1}$). For the 1 mm square pattern shown in Figure 4.26 (a), 100 writing scans theoretically equal 60s of exposure [$100 \times (4\ mm / 6.67\ mm \cdot s^{-1})$]. However, as the 3-axis movement control system has a delay of a few milliseconds between the execution of each machine code command, the total time takes slightly longer. This delay also explains the uneven functionalization of a pattern resulting in more oxidation at the corners of the square pattern as the nozzle remains stationary there for milliseconds before moving on (see Figure 4.26 (a) at 250 repetitions). However, this effect was mitigated in higher exposure time as oxygen groups became saturated.

University of Malaya

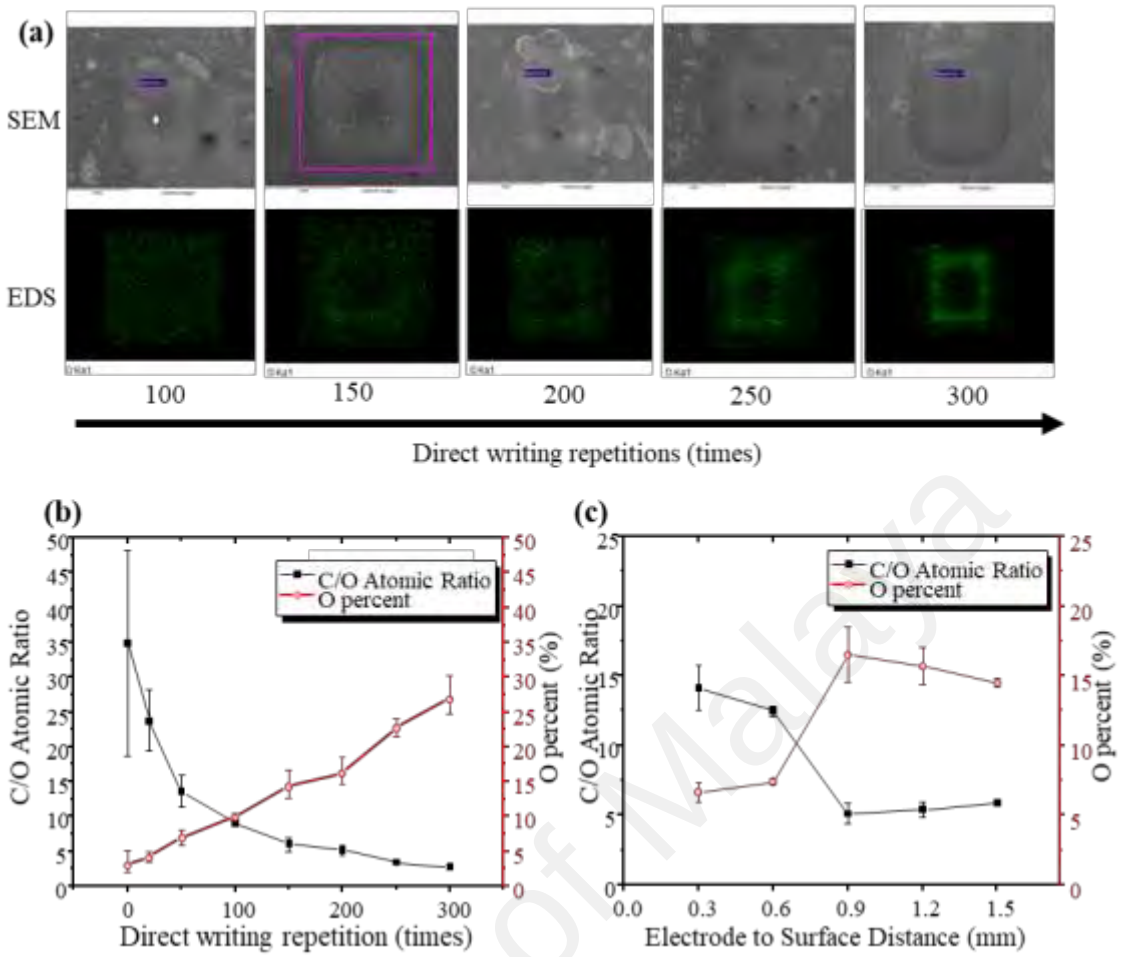

Figure 4.26: Effect of plasma direct-writing parameters on oxygen concentration. (a) FESEM and EDS elemental mapping of O over increasing exposure. The atomic percentage of oxygen and atomic C/O ratio over (b) various plasma direct-writing repetitions at 1 mm tungsten electrode tip to carbon surface distance and (c) various electrode tip to surface distances at 200 writing repetitions (N=3-6).

Figure 4.26 (b), shows a reduction in the C/O ratio, i.e., an increase in oxygen concentration as direct-writing repetitions increase. The C/O ratios were calculated from atomic carbon and oxygen percentage obtained from the EDS spot and area scans. A minimum C/O atomic ratio of 2.75±0.4 (corresponding to 2.06±0.29 by weight ratio) was achieved in these experiments. This result was markedly better than that for surface treatment of SU-8 pyrolyzed carbon using chamber plasma or acid treatment as reported previously (Hirabayashi, Mehta, Vahidi, Khosla, & Kassegne, 2013), where the minimum C/O ratios by weight percentage reported were ~4.9 for both plasma and strong acid

University of Malaya

treatment. Here, maximum surface oxidation achieved is 26.85±3 % by atom percent after 300 passes. The decrease in C/O ratio plateaued as writing repetitions increased further and the carbon surface becomes saturated with oxygen functional groups leaving little room for further functionalization. This phenomenon has been observed in a previous study of the plasma treatment of carbon nanotubes (Merenda et al., 2016). For comparison, the C/O ratio achieved in this study approaches those observed for un-reduced graphene oxide(Xu et al., 2015; J. Zhang, Xu, Liu, Yang, & Liu, 2015). Unlike poorly conductive graphene oxide, pyrolyzed carbon structures remain electrically conductive after surface functionalization (Hirabayashi, Mehta, Vahidi, et al., 2013). Note that the large error bar in the C/O ratio (18 to 48) for the untreated carbon in Figure 4.26 (b) was produced by a minor variation in the amount of corresponding oxygen percent (5 to 2%).

The effect of the distance between the tungsten electrode tip and the carbon surface on the oxygen concentration was also investigated. The graph in Figure 4.26 (c), shows that there is no significant increase in oxygen concentration at the surface when the distance is less than 0.6 mm. The oxygen concentration markedly improves at a distance around 1 mm and then, at yet larger distances, is slightly reduced again. With the smallest electrode gaps, the secondary ion emission from the Townsend avalanche is lower because of lower gas molecules in the discharge path, and this may cause a lower degree of functionalization. On the other hand, as the electrodes' distance becomes further apart, the plasma ion energy is reduced, and this also results in a lower oxygen concentration at larger distance.

In terms of writing resolution, EDS elemental mapping was used to measure the linewidths of the plasma written patterns. Oxygen patterns in elemental maps were only observed once the surface oxygen concentration was higher than ~15%. As such, pattern

University of Malaya

resolutions acquired under 200 writing scans were unable to measure. For the samples that could be measured, it was found that linewidth variations were insignificant at various writing repetitions and various electrode gaps. The linewidth of direct-written patterns averages 141 μm with a standard deviation of 30 μm (N=12). This resolution is in line with the microplasma jet printing of nanomaterials previously reported (Gandhiraman et al., 2014). To understand the aging effect on surface functionalization, the surface oxygen concentration was examined after three months of storage of the patterned carbon samples in normal room conditions. EDS scanning of plasma-treated spots showed that the oxygen concentration decreased an average of 1.9% (N =4) while untreated areas remained the same. High stability of carboxylic functionals is due to their already high oxidation state and their high thermal and electrochemical stability (Y. Han et al., 2017; S. K. Park, Mahmood, & Park, 2013).

4.3.4 Types of oxygen functionalities in plasma direct writing

Although EDS scans can determine the atomic and weight percentages of oxygen and carbon on the electrode surface, it does not reveal the nature of the carbon to oxygen bonding such as in carbonyl, hydroxyl, epoxyl or carboxyl bonding. Hence, XPS was performed to identify the exact nature of the oxygen-containing functional groups on the carbon surface after microplasma direct writing. An area of 3 mm × 2 mm of a carbon film surface was treated by plasma direct writing with the tungsten tip at 1 mm distance from the carbon surface and scan repetitions of 300 times. XPS spectra were taken from pristine and microplasma treated areas of the same carbon film, and the results are illustrated in Figure 4.27. The total atomic oxygen concentration increased from 3.9% in the untreated area to 27.24% in the treated areas (Figure 4.27 (e)). Hence, the atomic C/O ratio was reduced from 24.5 to 2.56 which agrees with the EDS measurements discussed above. The C/O ratio in untreated SU-8 derived pyrolyzed carbon is also in agreement with previous literature data where 3.1% of atomic oxygen was measured using XPS

University of Malaya

measurement(Y. Lim, J.-I. Heo, M. Madou, & H. Shin, 2013). In an XPS survey scan of the treated area, there was also a trace amount of sodium and calcium at 1.04 % and 1.24 % respectively, indicating possible dissolved salts in the water vapor source.

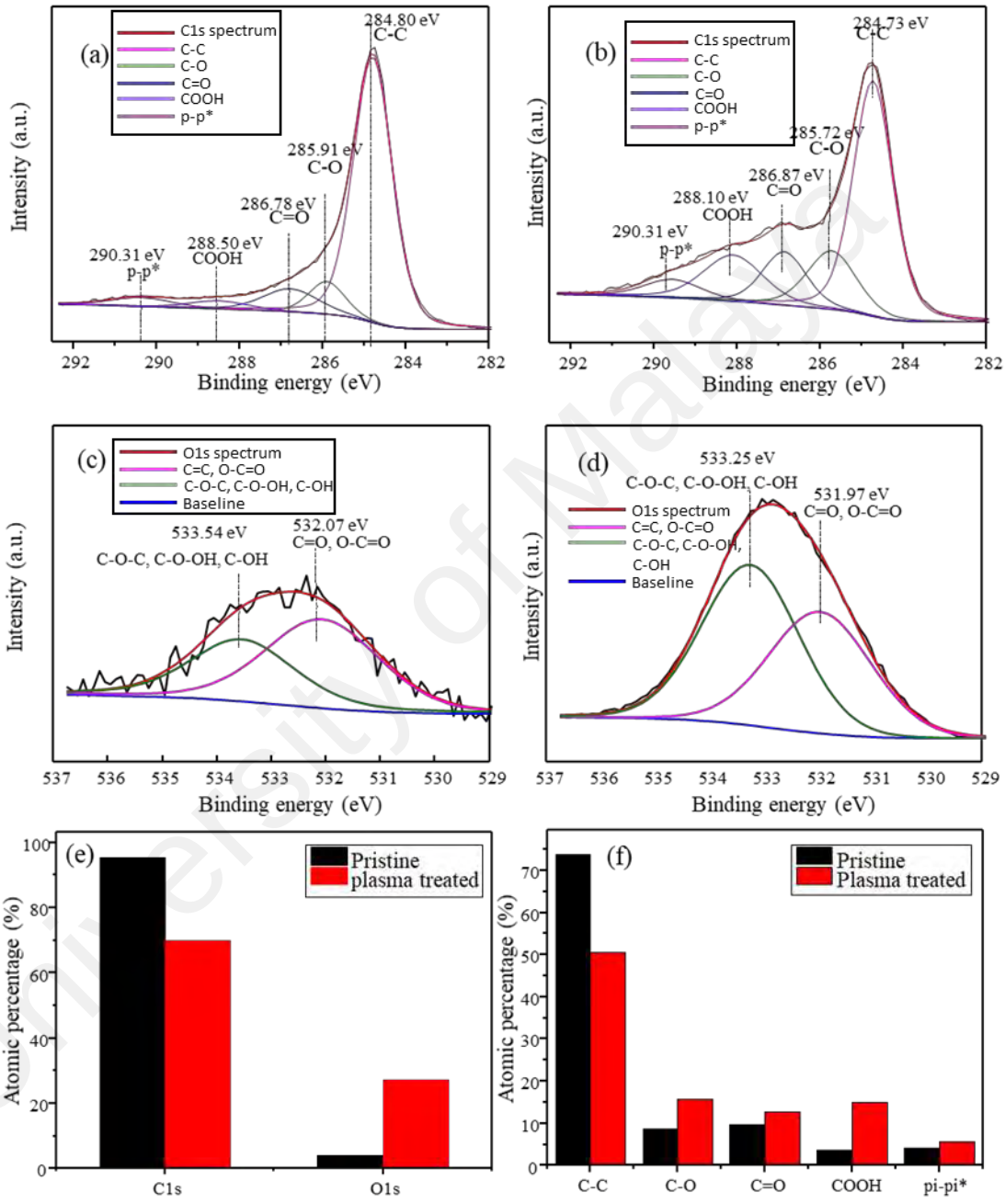

Figure 4.27: **Results of XPS analysis of carbon electrode in pristine and treated areas. High-resolution XPS spectra of C1s of (a) pristine and (b) plasma direct written samples respectively. High-resolution XPS of O1s of (c) pristine and (d) plasma treated sample respectively. (e) Atomic percentage of C1s and O1s as measured by XPS. (f) Relative percentage of oxygen functional groups before and after plasma treatment. Plasma treatment in the graphs were performed at 1mm distance and 300 repetitions.**

University of Malaya

High-resolution XPS spectra were deconvoluted with a nonlinear curve fitting program. The C1s spectra were deconvoluted into five peaks related to carbon atoms in C-C bonds at 284.80 eV, C-O bonds at 285.91 eV indicating possible phenol, hydroxyl, alcohol and ether groups, C=O bonds at 286.78 eV indicating carbonyl, quinone groups and O-C=O groups at 288.50 eV indicating carboxylic groups(Datsyuk et al., 2008). The π–π^* transitions were evident at 290.31 eV. The XPS results indicated that pristine carbon surfaces feature some oxygen groups which may be the remnants of epoxyl and phenol groups initially present in the SU-8 precursor. After plasma treatment, the percentage of oxygen functionalities in the C1s spectra increased while the peaks were slightly shifted left. All the carbon to oxygen bonds increased after treatment as evident from Figure 4.27(f). The most significant change occurs for carboxylic (COOH) groups which showed a 4 times enhancement from 3.68 to 14.92 percent of C1s. The increased carboxylation is important for biomolecules immobilization in the fabrication of carbon MEMS-based biosensors. Deconvolution of the XPS O1s peak resulted in two peaks: one at 533.54 eV and one at 532 eV. The former corresponds to C-O-C and C-OH groups, while the latter indicates C=O groups of carbonyl and carboxylic functional groups(Datsyuk et al., 2008; Kwan, Ng, & Huan, 2015). The increase in hydrophilic functional groups, i.e. hydroxyl and carboxyl, explains the improvement of the hydrophilic characteristics as shown in Figure 4.28. With increased plasma writing repetitions, the water contact angle decreased from ~90° to ~20°.

University of Malaya

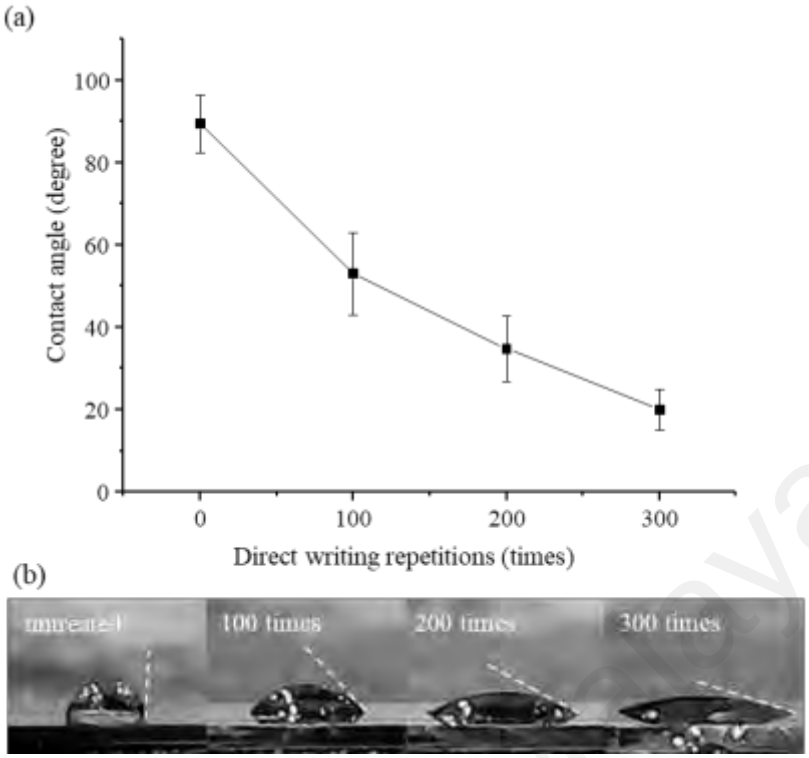

Figure 4.28: Water droplet contact angle analysis. (a) contact angle as a function of plasma direct writing repetitions (N=3). (b) Representative photos of water droplets in various direct-writing times.

4.3.5 Comparison with other functionalization techniques

A comparison of various surface treatments on carbon materials and the resultant reduction in C/O ratio (i.e., increased oxygen percentage) is presented in Table 4.14. The oxidation degree by surface treatment has been described in various forms in the literature, such as by the C/O ratio (Hirabayashi, Mehta, Vahidi, et al., 2013), the oxygen to carbon (O/C) ratio (Yue, Jiang, Wang, Gardner, & Pittman, 1999) and the percentage of oxygen (Datsyuk et al., 2008; Mortensen et al., 2006), making a direct comparison between different data sources difficult. Here, all values were converted to the corresponding C/O ratio for comparison. Among the treatment methods compared, the plasma direct-writing method shows the most significant increase in the oxygen percentage, and it also reduces the treatment time (in small area treatment). In terms of

University of Malaya

carboxylation degree, vacuum UV treatment has the highest carboxylation degree at 15% (Penmatsa et al., 2015). Plasma direct writing produces comparable carboxylation at 14.92%.

Table 4.14: Comparison of the maximum reduction in C/O ratio achieved with various surface oxidation treatment of carbon electrodes

Surface treatment methods	Carbon materials	Treatment times	Analysis	C/O		References
				Untreated	Treated	
Oxygen plasma treatment	Pyrolyzed carbon	300 s	EDS	19*	4.9*	(Hirabayashi, Mehta, Vahidi, et al., 2013)
Acid treatment (Sulfuric, Nitric acids)	Pyrolyzed carbon	15 h	EDS	19*	4.9*	(Hirabayashi, Mehta, Vahidi, et al., 2013)
Vacuum UV treatment	Pyrolyzed carbon	75 min	XPS	14	4.1	(Penmatsa et al., 2015)
Acid treatment (Nitric acid)	Carbon nanotubes	48 h	XPS	24.8	3.44	(Datsyuk et al., 2008)
Oxygen plasma treatment	Carbon fiber	9 min	XPS	16.67	5.68	(Lai & Lo, 2015)
Electrochemical treatment	Carbon fiber	176.7 min	XPS	6.32	3.8	(Yue et al., 1999)
Helium plasma touch	Glassy carbon	300s	XPS	30.25	3.11	(Mortensen et al., 2006)
Plasma direct writing	Pyrolyzed carbon	180 s (300 times)	EDS	25.38*	2.06*	this work
			EDS	34.91	2.75	
			XPS	24.5	2.56	

* represents C/O ratios in weight percent. Unless otherwise noted, C/O ratios are in atomic percent.

4.3.6 Electrochemical properties characterization of plasma direct-written carbon surfaces

The effect of surface-bonded oxygen functional groups on the carbon surface was evaluated using cyclic voltammetry (CV) in a 0.5M H_2SO_4 solution. Double layer charging experiments were carried out in a non-faradaic charging voltage region i.e. 0.3 to 0.5 V at different scan rates from 10 $mV{\cdot}s^{-1}$ to 100 $mV{\cdot}s^{-1}$. The double-layer capacitance (C_{dl}) was calculated by plotting half of the difference between the anodic and cathodic current densities ($\Delta j/2$) at 0.4 V against the scan rate (s). The slope of that plot corresponds to the electrochemical double-layer capacitance (Figure 4.29 (c)). From this

University of Malaya

plot, the double-layer capacitances of pristine carbon surface and plasma direct-written carbon surface were found to be 0.0183 mF/cm^2 and 0.1492 mF/cm^2, respectively. This increase of approximately 8 times indicates that microplasma direct-writing increases the density of phenolic hydroxyl groups which improves the double layer capacitance(L.-x. Li & Li, 2011; Oda, Yamashita, Minoura, Okamoto, & Morimoto, 2006).

CVs of plasma treated samples using a three-electrode cell in Figure 4.27 (d) reveal Faraday's current contribution at a broad peak of 0.1 to 0.4V indicating the development of a pseudocapacitance. The geometric specific capacitance (C_s) of the carbon electrodes were evaluated in a larger potential window from 0 to 1 V. The calculations were based on the following expression (Xiaofeng Wang, Yin, Hao, & You, 2015) :

$$C_s = \frac{\int I(V)dV}{2 \cdot s \cdot \Delta V \cdot A} \tag{4.3}$$

where $\int I(V)dV$ is the total charge obtained by integration of anodic and cathodic currents in a cyclic voltammogram, s is the scan rate, ΔV is voltage range of the CV sweep and A is the active surface area. The specific capacitances of the as-produced and the treated carbon electrodes at a 25 mV·s^{-1} scan rate are 8.82 mF·cm^{-2} and 46.64 mF·cm^{-2} respectively, showing an increase of 5 times across various scan rates (Figure 4.27 (e)) The total improvement in specific capacitance can be credited to the improved electrode hydrophilicity as well as the increased hydroxyl, carbonyl and carboxylic groups which allows faster faradic reactions and increase the pseudocapacitance (Cao et al., 2018; Lai & Lo, 2015; L.-x. Li & Li, 2011; C.-C. Lin & Liao, 2011). The results also indicate that plasma treated electrodes exhibit a hybrid of pseudocapacitance and electrical double layer capacitance properties.

University of Malaya

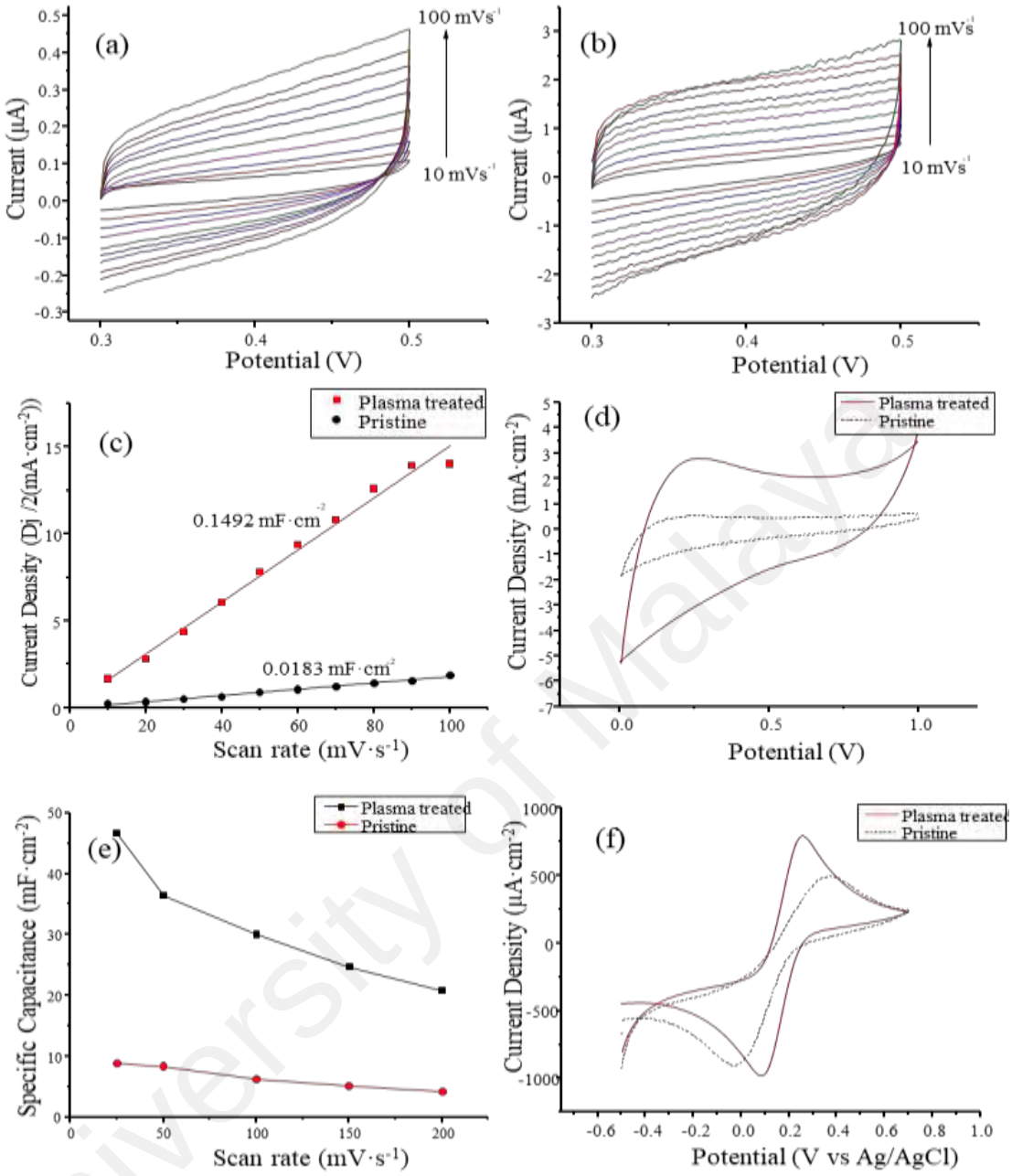

Figure 4.29: Electrochemical characterization results. Cyclic voltammograms (CV) of (a) pristine carbon and plasma direct-write carbon (b) surface in 0.5M H_2SO_4 with scan rates from 10 mV·s^{-1} to 100 mV· s^{-1}. (c) Relationship between scan rate and half of the difference between anodic and cathodic current densities (Δj/2) at 0.4 V. The slope is C_{dl}. (d) CVs of carbon electrodes in 0.5M H_2SO_4 at 50 mV s^{-1} scan rate. (e) The specific capacitance of carbon electrodes at various scan rates. (f) The electrochemical response of electrodes in 1mM K_3 [$FeCN_6$] /0.1 M KCL solution at a scan rate of 10 mV s^{-1}. (All the plasma treatment in the graphs were performed at 1mm distance and 300 repetitions.)

The Faradaic electrochemical performance of carbon electrodes are often evaluated using a ferri/ferrocyanide redox couple in solution (Brownson & Banks, 2014; Mardegan et al., 2013; Pasakon et al., 2019). In the experiments, a three-electrode electrochemical

University of Malaya

cell was used comprising a large carbon counter electrode, an Ag/AgCl reference and a pyrolyzed carbon working electrode in a 1mM $K_3[FeCN_6]$/0.1 M KCL solution. The peak current and the peak to peak potential separation are important indicators of the charge transfer properties of the electrode surface. The anodic peak current density of the plasma-treated carbon electrodes is 790.51 $\mu A \cdot cm^{-2}$, and that of as-pyrolyzed carbon is 497.01 $\mu A \cdot cm^{-2}$. The ratio of the anodic to cathodic peak currents (I_{pa}/I_{pc}) significantly improved from 0.55 in non-treated carbon to 0.98 after plasma direct writing. This improvement approaching 1 indicates a more reversible reaction on the electrode surface after treatment. The peak to peak separation (ΔE_p) of the plasma direct-written surface was found to be 0.17±0.02 mV compared to 0.5±0.12 mV of the untreated electrode also indicating faster electron transport and increased electrochemical reversibility after plasma treatment. This faster charge transfer with a functionalized carbon surface has been attributed to the presence of oxygen-containing groups, especially double-bonded C=O in carbonyl and carboxyl groups (L.-x. Li & Li, 2011). The results show that microplasma direct-writing treatment enhances the electrochemical properties of Carbon MEMS manufactured electrodes by promoting charge transfer and thus, making them more suitable for electrochemical sensor applications.

4.3.7 Immobilization of DNA aptamer probe on carbon biosensor

Amine modified DNA aptamer probe of sequence (NH2-5′ - TATGGCGGCGTCACCCGACG GGGACTTGACATTATGACAG-3′) was used as a probe for *Salmonella* bacteria. This amine-functionalized aptamer was covalently attached to the carboxylic (-COOH) groups by sulfo-NHS and EDC crosslinking mechanism. In order to test the immobilization of the probe sequence on the plasma written surface, a complementary sequence with fluorescent modification was used to hybridize with an aptamer probe and fluorescent microscopy images were taken. High

University of Malaya

fluorescence concentration on the treated area in Figure 4.30 illustrates the successful immobilization of DNA aptamer probes on plasma written pattern.

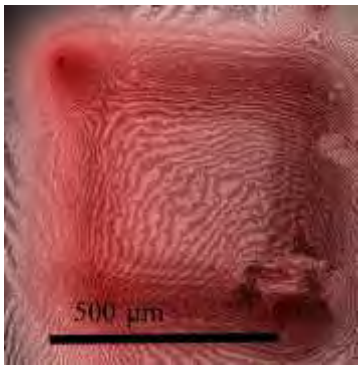

Figure 4.30: Fluorescence microscopy image of plasma written square pattern immobilized with fluorescence tagged aptamer probes.

4.4 Result of chemiresistive *Salmonella* sensing assay

Carbon nanowires with sub-100 nm and suspended 10um from the silicon surface on carbon support structures were fabricated following the steps described earlier. Carbon nanowires are then treated with plasma direct writing for carboxylic functionalization and subsequently crosslinked with *Salmonella* specific aptamer probes. This section discusses the integration of carbon nanowire sensors with a microfluidic structure and evaluating of biosensor performance.

4.4.1 Fabrication of nanowire sensor biochip

The step-by-step evolution of polymer nanowire to a carbon nanowire sensor chip is illustrated in Figure 4.31. Confined UV exposure at supporting structures crosslinks SU-8 polymer fibers between them. After development, non-crosslinked fibers are washed away while retaining crosslinked polymer nanowires. Upon pyrolysis, the supporting structures shrank at the top while the base retained the original size. This shrinkage of support structure mechanically stretched the nanowire during pyrolysis making it longer,

University of Malaya

thinner and more graphitic by rearranging carbon layers under strain (S. Sharma et al., 2012). The suspended nanowires shrank 50%-70% during pyrolysis. The gap between the top of the support structures widens from 20 µm to 44 µm as can be observed from micrographs, extending nanowire to an average 100% of the original length.

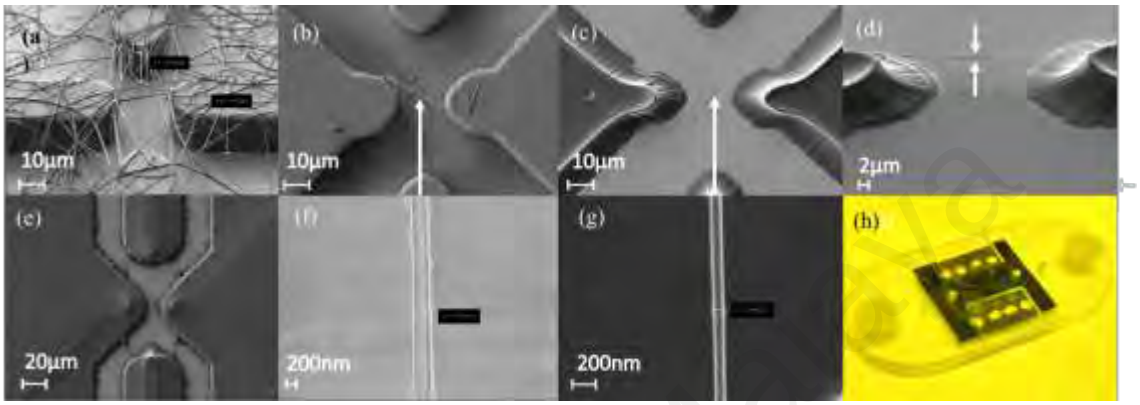

Figure 4.31: Fabrication of a carbon nanowire sensor chip. (a) Electrospun SU-8 nanowire mat on support structures. (b) Single suspended SU-8 nanowire after photolithography and development. (c) Suspended carbon nanowire after pyrolysis. (d) Titled side view of suspended carbon nanowire showing suspension. (e) Nanowire sensor in the SU-8 microfluidic channel. (f) Magnification of SU-8 nanowire from (b). (g) Carbon nanowire after pyrolysis. (h) Suspended carbon nanowire chip inside the microfluidic platform.

As fabricated, carbon nanowires were found to have an average diameter of 84 nm±29 with the height of suspension at 10 µm as measured from the micrograph. This suspension enabled the carbon nanowire to have better contact with bacteria suspended inside the solution while eliminating electronic interferences from the silicon surface. Figure 4.31 (e) shows the sensor chip after insulating with the SU-8 layer. Microfluidic channel exposed the nanowire only while covering supporting carbon structures. This is to avoid unwanted immobilization and chemical reactions at supports, which could affect the analysis. Figure 4.31 (h) shows the as-fabricated sensor integrated with PMMA microfluidic chip. Microfluidic channels have 0.1 mm width and 0.1 mm channel height. Inlet and outlet of channels are 3 mm in diameter. Electrode contact pads were coated with silver paste for better contact with mini-crocodile clip and prevent scratching of the

University of Malaya

carbon layer during the experiments. The silver paste layer also reduced the contact resistance between the clip and sensor giving a more reliable reading of sensor value.

4.4.2 Chemiresistive sensing of bacterial cells

Carbon nanowires showed a reduction in resistance after functionalization with an aptamer probe as shown in Figure 4.32. However, there is no significant change in resistance of the nanowire in the presence of distilled water or phosphate-buffered saline (PBS) solution, which agrees with MWCNT chemiresistors in a previous study (Fu et al., 2017). It was also observed that there is no difference in resistance between wet and dry electrodes after the functionalization step. Hence, bacterial sensing experiments were performed in the wet state of the sensor. This is important as, in some existing chemiresistive sensing reports, electrical measurements were performed only after drying of the sensors which are not practical for a rapid lab-on-chip diagnostic device (Fu et al., 2017; Paul K et al., 2017).

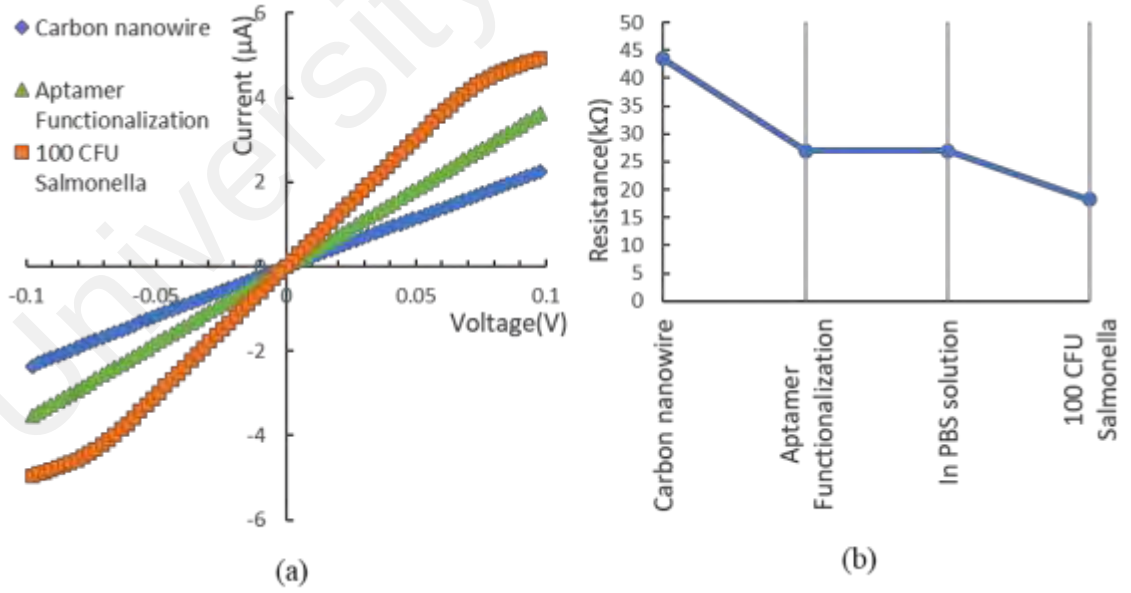

Figure 4.32: Changes in electrical properties of a nanowire sensor during functionalization and detection (a) Current vs. Voltage (*I-V*) characteristics. (b) Corresponding resistance changes.

University of Malaya

4.4.2.1 Sensitivity evaluation

In chemiresistive bacterial sensing, binding of bacteria to nanowire can be determined by measuring changes in the conductivity of the sensor. *I-V* characterization of electrodes was carried out before and after the introduction and incubation with the analyte. After inserting 5 µL of prepared bacteria suspension droplet onto the microfluidic chip, the sensor was incubated for 5 min to allow for binding before recording the second *I-V* characterization. Resistance was obtained from the inverse of the *I-V* curve slope. The percentage changes in resistance after incubation was calculated as $\Delta R/R_0$, where ΔR is the difference between resistance after incubation with bacteria (R) and original resistance (R_0). From the calibration curve correlating bacteria concentration and percentage change from Figure 4.33(a), it can be observed that an increase in *S.* Typhimurium concentration results in a reduction in nanowire resistance. The increase in conductivity can be explained by the fact that *Salmonella* is a Gram-negative bacterium that has lipopolysaccharides on its cell wall contributing strong negative charges. Hence, upon binding with the aptamer, negative charges induce electron holes in the nanowire, making the carbon nanowire more conductive (Hepel, 2012; Kaisti, 2017). This finding agrees with previous reports of *E.* coli sensing on graphene (Huang, Dong, Liu, Li, & Chen, 2011; Mohanty & Berry, 2008).

The lower limit of detection of the bacterial sensor was determined to be ^{10} CFU/mL (Figure 4.33(a)). This is lower than conventional detection methods of *Salmonella* using DNA extraction and colorimetric detection techniques such as polymeric chain reaction (PCR) and loop-mediated isothermal amplification (LAMP). The detection limit is equal to potentiometric aptasensor recently reported (Muniandy et al., 2017). Among point-of-care lab-on-chip systems, the suspended carbon nanowire sensor has a much higher detection limit than recently reported lab-on-Disc microdevice for the foodborne pathogen detection which has the detection limit of 2.7×10^4 CFU/mL (Sayad et al., 2018).

University of Malaya

Moreover, *Salmonella* detection is performed using just 5 µL of sample volume which is less than recent lab-on-chip platforms which require 12.5 to 25 µL for *Salmonella* detection (Oh et al., 2016; Sayad et al., 2018). A comparison of the carbon nanowire sensors with different reported techniques is presented in Table 4.15.

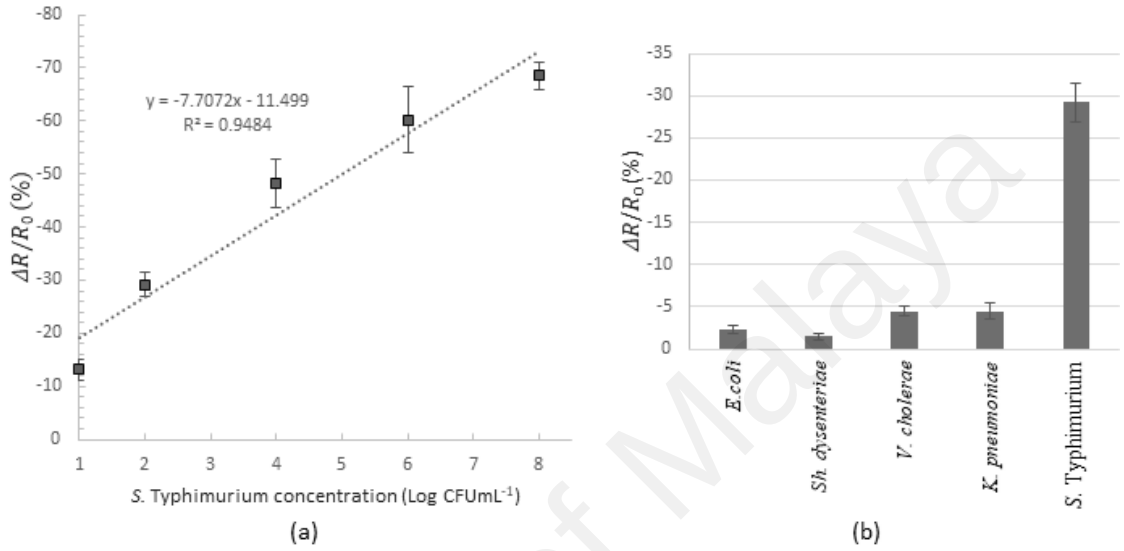

Figure 4.33: Carbon nanowire sensor evaluation for *S.* Typhimurium detection. (a) Bacteria concentration vs. percentage change in resistance of nanowire before and after incubation. (b) Specificity evaluation against various bacteria at a concentration of 100 CFU/mL.

4.4.2.2 Specificity evaluation

The specificity of the nanowire sensor to *S.* Typhimurium was also investigated by incubating with different bacteria (*E. coli*, *Sh. dysenteriae*, *V. cholerae* and *K. pneumoniae)* with 10^2 CFU/mL concentration and *I-V* analysis was carried out after 5 mins of incubation. The sensors showed no significant changes in conductivity for non-*Salmonella* bacteria as shown in Figure 4.33(b). The results demonstrate the fabricated carbon nanowire chemiresistive sensors are highly selective and specific for *S.* Typhimurium detection. The total duration of the assay was estimated to be 5 min, i.e., 5 min of incubation and a few seconds for conductivity measurement. The assay time is

University of Malaya

much shorter than conventional methods and state-of-the-art electrochemical detection methods for *S.* Typhimurium. In addition, this chemiresistive sensing technique provides a simple, real-time one-step measurement without the need for additional electrochemical buffers. Compared to PCR and LAMP techniques, this carbon nanowire-based aptasensor does not require culturing bacteria and DNA extraction steps, which can add days to total analysis time.

Table 4.15: Comparison of various bacterial biosensing techniques with the current study

Detection method	Targeted bacteria	Limit of detection (CFU/mL)	Assay time	Reference
PCR	*Salmonella* spp.	10^3	3 h	(L. Wang, Li, & Mustapha, 2007)
LAMP	*Salmonella* spp.	10^2	3 h	(S. Chen et al., 2011)
CNT FET electronic sensor	*Salmonella* Infantis	10^2	1 h	(Villamizar, Maroto, Rius, Inza, & Figueras, 2008)
Lab-on-Disk LAMP florescent microdevice	*Salmonella* spp.	$2.7x10^4$	1 h	(Sayad et al., 2018)
Potentiometric aptasensor	*S.* Typhimurium	10^1	10 min	(Muniandy et al., 2017)
Carbon nanowire chemiresistive aptasensor	*S.* Typhimurium	10^1	5 min	Current study

4.5 Summary

This chapter illustrates a facile method of fabricating suspended carbon nanowire electrodes and their use as a chemiresistive biosensor platform. Electrospinning of SU-8 2015 nanofibers was successfully demonstrated to various morphological properties and parameters needed for continuous nanofibers with uniform diameters are obtained. The finest and most uniform nanofibers were found to be deposited at a voltage of 12 kV with a needle-to-collector distance of 100 mm at a flow rate of 10 µL/min using far-field electrospinning setup. Sub-100 nm carbon nanowires suspended at 10 µm height between

University of Malaya

two carbon support structures have been fabricated in this study. To functionalize carbon biosensor, microplasma direct writing was introduced as an efficient, rapid, and site-selective surface treatment technique. The negative plasma streamer treatment increased the atomic oxygen content and carboxylic functional groups required for biomolecule immobilization with carboxyl functional groups increasing from 3.68 % to 14.92 % after treatment. The functionalized carbon nanowire sensor was then immobilized with *Salmonella*-specific aptamer and tested for *Salmonella* detection. The sensor platform showed a rapid detection of *S.* Typhimurium, foodborne pathogenic bacteria, in 5 minutes assay time with high sensitivity and specificity while requiring 5 μL of total sample volume for analysis. Hence, this nanoelectronics sensor was able to provide simple, rapid and one-step detection of whole-cell bacteria without the need for DNA extraction or additional analytical reagents required in other detection methods. With the on-chip integrated microfluidic system, this lab-on-chip bacteria testing can be applied as a point-of-care detection device for foodborne pathogens. This sensor platform can also be used to detect various biomolecules by functionalization with other appropriate aptamers.

University of Malaya

CHAPTER 5: CONCLUSIONS AND RECOMMENDATIONS FOR FUTURE WORK

5.1 Conclusions

An all-carbon suspended carbon nanowire biosensor chip for chemiresistive *Salmonella* detection has been developed, fabricated, and tested successfully. The combination of C-MEMS techniques and electrospinning of photoresist with optimized parameters allowed an easy and relatively inexpensive way to fabricate sub-100 nm suspended nanofibers on wafer-scale without using nanolithography techniques. Another major innovation in this work is selective surface functional groups patterning by microplasma direct writing. This allows a mask-less functionalization of carboxylic groups on C-MEMS manufactured carbon structures. This targeted surface treatment can be used for patterning of carbon electrodes with oxygen functional groups at room temperature and atmospheric pressure. The carbon nanowire sensors modified with specific surface receptors could be used as a powerful biomolecule detection platform that has capabilities for direct, label-free, real-time, ultrasensitive and highly selective detection of bacteria.

In addressing the sub-objective, I, the suspended carbon nanowires were produced by the integration of electrospinning and C-MEMS fabrication techniques. Support structures were fabricated by photolithography of SU-8 photoresist. For nanowire fabrication, both far-field and electromechanical spinning methods were investigated. While electromechanical spinning can be used to deposit polymer fibers in the programmed location, it produced an average fiber diameter of ~500 nm after carbonization. On the other hand, far-field electrospinning was able to produce polymer fibers with less than 200 nm with high repeatability with optimized parameters. Upon carbonization, polymer fibers underwent an average of 67% reduction in diameter and hence, sub-100 nm carbon nanowires were obtained. The minimum diameter obtained

University of Malaya

here is 42.95 nm. This is the minimum fiber thickness obtained from electrospinning among the SU-8 derived carbon nanowires. Hence, this work demonstrates the optimization of electrospinning parameters combined with stretching of fibers during pyrolysis could allow the fabrication of sub-100 nm carbon nanowires without needing rotating drum collectors. The characterization of nanowires shows the presence of graphitic components which was reflected in higher electrical conductivity of nanowire compared to support structures.

To address the sub-objective II, the functionalization of carbon electrode surfaces was investigated by acid treatment, electrochemical treatment, and plasma direct writing methods. Acid and electrochemical treatments resulted in the etching of the electrode surface. On the other hand, microplasma direct writing allows site-selective surface treatment and functional group patterning at atmospheric conditions. For microplasma direct writing, the effects of both positive and negative corona plasma streamers were investigated on the functionalization efficiency. The negative plasma streamer treatment increased the atomic oxygen content from ~3 to 27% at 300 scan repetitions (180 s for a 4 mm length). The XPS findings indicate the enhancement of carbonyl, carboxylic and hydroxyl groups for the treated carbon surface with carboxylic functional groups showing the most improvement with an increase from 3.68 % to 14.92%. Consequently, plasma direct writing improves the hydrophilicity and the electrochemical characteristics of the carbon surface. The specific capacitance of the treated area is 46.64 $mF \cdot cm^{-2}$ at a 25 $mV \cdot s^{-1}$ scan rate which shows a 5-fold increase from the non-treated carbon. Furthermore, microplasma treated carbon surfaces also improve the electrochemical reversibility and yield faster electron transfer characteristics. Hence, this technique can be used to enhance bio- and electrochemical sensing performances as well as energy storage efficiencies of carbon micro/nanoelectrodes.

University of Malaya

In addressing sub-objective III, nanoelectronics biosensor's performance towards bacterial sensing was evaluated by functionalization with *Salmonella*-specific aptamer probes. Immobilization of *Salmonella* specific aptamers on carbon surface was performed by EDC/NHS crosslinking mechanism and characterized by fluorescence microscopy. The device was tested with varying concentrations of *Salmonella* Typhimurium to evaluate the sensitivity and with various other bacteria to evaluate specificity. The results showed that the sensor is highly specific and sensitive in the detection of *Salmonella* with a detection limit of 10 CFU/mL. Moreover, this chemiresistive assay has a reduced turnaround time of 5 minutes while requiring the only 5μL of sample volume. This suspended nanowire sensor was able to provide simple, rapid and one-step detection of whole-cell bacteria without the need for DNA extraction or additional analytical reagents needed in other detection methods.

5.2 Summary of major contributions

(i) Wafer-scale production of suspended electrospun carbon nanowires of sub-100 nm diameter was demonstrated. This integration of standard electrospinning and photolithography to confine electrospun fibers in selective sites enable relatively low-cost fabrication carbon NEMS structures without necessitating expensive lithography method.

(ii) Microplasma direct writing of carboxylic functional groups was introduced as a site-selective surface functionalization method. This method enables patterning of functional groups in a simple, fast and cost-effective way and can be applied in atmospheric conditions. Microplasma direct written surfaces have the highest amount of oxygen concentration and carboxyl functional groups compared to other functionalization techniques.

University of Malaya

(iii) Aptamer based electronic biosensing using carbon MEMS structures was demonstrated and tested for sensitivity and selectivity. This aptamer-based capturing of whole-cell bacteria combined with electronic detection enables the rapid detection of S. Typhimurium without needing cell-lysis.

5.3 Limitations and recommendations for future work

The limitations of this study and potential solutions are described as followed.

(i) Far-field electrospinning used in this study produces random deposition. Approximately 20% of the support structure in a silicon wafer do not receive suspended deposition. Hence, only a portion of the wafer is useable. Some of the chips receive multiple fiber depositions. A maximum of three fiber deposition was observed. The randomness of far-field electrospinning can be mitigated by the increased alignment of fibers. This can be achieved with either rotating drum collector or electric field based alignment schemes. Rotating drum collector has been used in suspended nanowire deposition on a single chip scale. The challenge is to scale up to a rotation drum that can accommodate larger silicon wafer. The use of rotating drum also has an advantage in further thinning of nanowire by mechanical stretching. Electrospinning with multiple nozzles as used in industrial scale electrospinning systems could also make fiber deposition uniform and hence, increase the yield of suspended fibers.

(ii) Currently, microplasma direct writing has line width of 141 μm which is larger than required for functionalization of sub-micron electrode. Resolution can be increased by specially designed nozzle with micro sized opening or nozzles with electrostatic repulsion to focus the plasma streamer discharge. Plasma direct writing can be expanded to other potential

University of Malaya

applications by using various plasma sources, e.g., combination of ammonia and noble gases can be used as source gas to pattern NH_2 functional groups which is an important functional group for biomolecule binding. This setup can also be utilized for nanolayer polymer deposition and patterning using plasma polymerization mechanism.

(iii) Continuous monitoring of electrical characteristic of the chip was not performed in the study. Nanowire conductivity depends on temperature with negative temperature coefficient. Hence, continuous monitoring of chips could increase the temperature which could effect the resistivity of nanowire in the process. The continuous monitoring and hence, detection of single bacteria could be enabled by measuring impedance of nanowire to electrolyte interface. Attachment of single *Salmonella* cell would have significant changes in nanowire to electrolyte charge conduction. By using electrochemical techniques such as chronoamperometry on nanowire, one could detect attachment of bacterial cell and improve its limit of detection to single cell domain.

(iv) As *Salmonella* species have negatively charged cell walls, bacteria cell could be theoretically drawn to nanowire electrode by electrophoretic manipulation. This could increase sensitivity of the sensor platform and reduces incubation time. This could also be used to separate bacteria from other particles.

(v) The experiments were performed with pre-processed bacteria suspension in Rapport Vassiliadis broth. To detect bacteria from unprocessed food, a more complete sensor platform could be devised by incorporating the pre-processed steps for bacteria cell extraction in a microfluidic platform.

University of Malaya

REFERENCES

Abdul Rashid, J. I., Abdullah, J., Yusof, N. A., & Hajian, R. (2013). The Development of Silicon Nanowire as Sensing Material and Its Applications. *Journal of Nanomaterials, 2013*, 16. doi:10.1155/2013/328093

Akinwande, D., Huyghebaert, C., Wang, C.-H., Serna, M. I., Goossens, S., Li, L.-J., . . . Koppens, F. H. (2019). Graphene and two-dimensional materials for silicon technology. *Nature, 573*(7775), 507-518.

Andrady, A. L. (2008). *Science and technology of polymer nanofibers*: John Wiley & Sons.

Babel, A., Li, D., Xia, Y., & Jenekhe, S. A. (2005). Electrospun nanofibers of blends of conjugated polymers: morphology, optical properties, and field-effect transistors. *Macromolecules, 38*(11), 4705-4711.

Barhate, R., & Ramakrishna, S. (2007). Nanofibrous filtering media: filtration problems and solutions from tiny materials. *Journal of Membrane Science, 296*(1), 1-8.

Barsan, M. M., Ghica, M. E., & Brett, C. M. (2015). Electrochemical sensors and biosensors based on redox polymer/carbon nanotube modified electrodes: A review. *Analytica Chimica Acta, 881*, 1-23.

Barsan, N., & Weimar, U. (2001). Conduction Model of Metal Oxide Gas Sensors. *Journal of Electroceramics, 7*(3), 143-167.

Barsan, N., & Weimar, U. (2003). Understanding the fundamental principles of metal oxide based gas sensors; the example of CO sensing with SnO2 sensors in the presence of humidity. *Journal of Physics: Condensed Matter, 15*(20), R813-R839.

Basu, S., & Basu, P. K. (2009). Nanocrystalline Metal Oxides for Methane Sensors: Role of Noble Metals. *Journal of Sensors, 2009*, 1-20.

Belmonte, T., Arnoult, G., Henrion, G., & Gries, T. (2011). Nanoscience with non-equilibrium plasmas at atmospheric pressure. *Journal of Physics D: Applied Physics, 44*(36), 363001.

Bisht, G., Canton, G., Mirsepassi, A., Dunn-Rankin, D., Kulinsky, L., & Madou, M. (2011). Novel polymeric inks for precision patterning of carbon micro/nano-fibers using near-field electrospinning. *Proceedings of Technologies for Future Micro-Nano Manufacturing, Napa, CA*.

Bisht, G., Nesterenko, S., Kulinsky, L., & Madou, M. (2012). A Computer-Controlled Near-Field Electrospinning Setup and Its Graphic User Interface for Precision Patterning of Functional Nanofibers on 2D and 3D Substrates. *Journal of Laboratory Automation, 17*(4), 302-308.

Bisht, G. S., Canton, G., Madou, M., Mirsepassi, A., & Dunn-rankin, D. (2012). *Low Voltage Near-Field Electrospinning Method and Device*.

University of Malaya

Bisht, G. S., Canton, G., Mirsepassi, A., Kulinsky, L., Oh, S., Dunn-Rankin, D., & Madou, M. J. (2011). Controlled Continuous Patterning of Polymeric Nanofibers on Three-Dimensional Substrates Using Low-Voltage Near-Field Electrospinning. *Nano letters, 11*(4), 1831-1837.

Bollella, P., Gorton, L., Ludwig, R., & Antiochia, R. (2017). A Third Generation Glucose Biosensor Based on Cellobiose Dehydrogenase Immobilized on a Glassy Carbon Electrode Decorated with Electrodeposited Gold Nanoparticles: Characterization and Application in Human Saliva. *Sensors, 17*(8), 1912.

Brownson, D. A. C., & Banks, C. E. (2014). Interpreting Electrochemistry *The Handbook of Graphene Electrochemistry* (pp. 23-77). London: Springer London.

Bugarski, B., Amsden, B., Goosen, M., Neufeld, R., & Poncelet, D. (1994). Effect of electrode geometry and charge on the production of polymer microbeads by electrostatics. *The Canadian Journal of Chemical Engineering, 72*(3), 517-521.

Canton, G. (2014). *Development of Electro-Mechanical –EMS-Spinning for Controlled Deposition of Carbon Nanofibers*. Retrieved from

Canton, G., Do, T., Kulinsky, L., & Madou, M. (2014). Improved conductivity of suspended carbon fibers through integration of C-MEMS and Electro-Mechanical Spinning technologies. *Carbon, 71*(0), 338-342.

Cao, H., Peng, X., Zhao, M., Liu, P., Xu, B., & Guo, J. (2018). Oxygen functional groups improve the energy storage performances of graphene electrochemical supercapacitors. *RSC Advances, 8*(6), 2858-2865.

Cardenas-Benitez, B., Eschenbaum, C., Mager, D., Korvink, J. G., Madou, M. J., Lemmer, U., . . . Martinez-Chapa, S. O. (2019). Pyrolysis-induced shrinking of three-dimensional structures fabricated by two-photon polymerization: experiment and theoretical model. *Microsystems & Nanoengineering, 5*(1), 38. doi:10.1038/s41378-019-0079-9

Chang, C., Limkrailassiri, K., & Lin, L. (2008). Continuous near-field electrospinning for large area deposition of orderly nanofiber patterns. *Applied Physics Letters, 93*(12), 123111.

Chen, D., Lei, S., & Chen, Y. (2011). A single polyaniline nanofiber field effect transistor and its gas sensing mechanisms. *Sensors, 11*(7), 6509-6516.

Chen, S., Wang, F., Beaulieu, J. C., Stein, R. E., & Ge, B. (2011). Rapid detection of viable salmonellae in produce by coupling propidium monoazide with loop-mediated isothermal amplification. *Applied and Environmental Microbiology, 77*(12), 4008-4016.

Chen, Y., Li, X., Park, K., Song, J., Hong, J., Zhou, L., . . . Goodenough, J. B. (2013). Hollow carbon-nanotube/carbon-nanofiber hybrid anodes for Li-ion batteries. *Journal of the American Chemical Society, 135*(44), 16280-16283.

Conway, B. (1999). The Double Layer and Surface Functionalities at Carbon. In B. Conway (Ed.), *Electrochemical Supercapacitors* (pp. 183-220): Springer.

University of Malaya

Cui, Y., Wei, Q., Park, H., & Lieber, C. M. (2001). Nanowire nanosensors for highly sensitive and selective detection of biological and chemical species. *Science, 293*(5533), 1289-1292.

Datsyuk, V., Kalyva, M., Papagelis, K., Parthenios, J., Tasis, D., Siokou, A., . . . Galiotis, C. (2008). Chemical oxidation of multiwalled carbon nanotubes. *Carbon, 46*(6), 833-840.

Davydova, A., Vorobjeva, M., Pyshnyi, D., Altman, S., Vlassov, V., & Venyaminova, A. (2016). Aptamers against pathogenic microorganisms. *Critical reviews in microbiology, 42*(6), 847-865.

Deitzel, J., Kleinmeyer, J., Hirvonen, J., & Beck Tan, N. (2001). Controlled deposition of electrospun poly (ethylene oxide) fibers. *Polymer, 42*(19), 8163-8170.

DeShon, W. E., & Carson, R. S. (1968). Electric field investigations and a model for electrical liquid spraying. *Journal of Colloid and Interface Science, 28*(1), 161-166.

Dey, A., Lopez, A., Filipič, G., Jayan, A., Nordlund, D., Koehne, J., . . . Meyyappan, M. (2019). Plasma jet based in situ reduction of copper oxide in direct write printing. *Journal of Vacuum Science & Technology B, 37*(3), 031203.

Di Benedetto, F., Camposeo, A., Pagliara, S., Mele, E., Persano, L., Stabile, R., . . . Pisignano, D. (2008). Patterning of light-emitting conjugated polymer nanofibres. *Nature nanotechnology, 3*(10), 614-619.

Du, R., Ssenyange, S., Aktary, M., & McDermott, M. T. (2009). Fabrication and characterization of graphitic carbon nanostructures with controllable size, shape, and position. *Small, 5*(10), 1162-1168.

Dvir, T., Timko, B. P., Kohane, D. S., & Langer, R. (2011). Nanotechnological strategies for engineering complex tissues. *Nature nanotechnology, 6*(1), 13-22.

Fàbrega, A., & Vila, J. (2013). Salmonella enterica serovar Typhimurium skills to succeed in the host: virulence and regulation. *Clinical microbiology reviews, 26*(2), 308-341. doi:10.1128/CMR.00066-12

Feng, J. (2002). The stretching of an electrified non-Newtonian jet: A model for electrospinning. *Physics of Fluids (1994-present), 14*(11), 3912-3926.

Feng, J. (2003). Stretching of a straight electrically charged viscoelastic jet. *Journal of Non-Newtonian Fluid Mechanics, 116*(1), 55-70.

Fu, Y., Romay, V., Liu, Y., Ibarlucea, B., Baraban, L., Khavrus, V., . . . Rümmeli, M. (2017). Chemiresistive biosensors based on carbon nanotubes for label-free detection of DNA sequences derived from avian influenza virus H5N1. *Sensors and Actuators B: Chemical*.

Fujii, T., Sudoh, K., & Sakakihara, S. (2017). Comparison of mechanical characteristics of focused ion beam fabricated silicon nanowires. *Japanese Journal of Applied Physics, 56*, 06GN17.

University of Malaya

Gandhiraman, R. P., Jayan, V., Han, J.-W., Chen, B., Koehne, J. E., & Meyyappan, M. (2014). Plasma jet printing of electronic materials on flexible and nonconformal objects. *ACS Applied Materials & Interfaces, 6*(23), 20860-20867.

Ghazinejad, M., Holmberg, S., Pilloni, O., Oropeza-Ramos, L., & Madou, M. (2017). Graphitizing non-graphitizable carbons by stress-induced routes. *Scientific Reports, 7*(1), 1-10.

Gopal, R., Kaur, S., Ma, Z., Chan, C., Ramakrishna, S., & Matsuura, T. (2006). Electrospun nanofibrous filtration membrane. *Journal of Membrane Science, 281*(1), 581-586.

Hamaguchi, N., Ellington, A., & Stanton, M. (2001). Aptamer beacons for the direct detection of proteins. *Analytical Biochemistry, 294*(2), 126-131.

Hamula, C. L., Guthrie, J. W., Zhang, H., Li, X.-F., & Le, X. C. (2006). Selection and analytical applications of aptamers. *TrAC Trends in Analytical Chemistry, 25*(7), 681-691.

Han, K., Liang, Z., & Zhou, N. (2010). Design strategies for aptamer-based biosensors. *Sensors, 10*(5), 4541-4557.

Han, Y., Hwang, G., Park, S., Gomez-Flores, A., Jo, E., Eom, I.-C., . . . Kim, H. (2017). Stability of carboxyl-functionalized carbon black nanoparticles: the role of solution chemistry and humic acid. *Environmental Science: Nano, 4*(4), 800-810.

He, J. H., Xu, L., Wu, Y., & Liu, Y. (2007). Mathematical models for continuous electrospun nanofibers and electrospun nanoporous microspheres. *Polymer International, 56*(11), 1323-1329.

Heo, J.-I., Lim, Y., Madou, M., & Shin, H. (2012). *Scalable suspended carbon nanowire meshes as ultrasensitive electrochemical sensing platforms.* Paper presented at the Micro Electro Mechanical Systems (MEMS), 2012 IEEE 25th International Conference on.

Hepel, T. (2012). Functional Nanoparticle-Based Bioelectronic Devices *Functional Nanoparticles for Bioanalysis, Nanomedicine, and Bioelectronic Devices Volume 2* (Vol. 1113, pp. 145-180): American Chemical Society.

Hernández, R., Vallés, C., Benito, A. M., Maser, W. K., Rius, F. X., & Riu, J. (2014). Graphene-based potentiometric biosensor for the immediate detection of living bacteria. *Biosensors and Bioelectronics, 54*, 553-557.

Hirabayashi, M., Mehta, B., Khosla, A., & Kassegne, S. (2013). Functionalization of Pyrolyzed Carbon Structures for Bio-Nanoelectronics Platforms. *ECS Transactions, 50*(12), 325-331. doi:10.1149/05012.0325ecst

Hirabayashi, M., Mehta, B., Vahidi, N. W., Khosla, A., & Kassegne, S. (2013). Functionalization and characterization of pyrolyzed polymer based carbon microstructures for bionanoelectronics platforms. *Journal of Micromechanics and Microengineering, 23*(11), 115001.

University of Malaya

Hirabayashi, M., Mehta, B., W. Vahidi, N., Khosla, A., & Kassegne, S. (2013). Functionalization and characterization of pyrolyzed polymer based carbon microstructures for bionanoelectronics platforms. *Journal of Micromechanics and Microengineering, 23*(11), 115001.

Hohman, M. M., Shin, M., Rutledge, G., & Brenner, M. P. (2001). Electrospinning and electrically forced jets. I. Stability theory. *Physics of Fluids (1994-present), 13*(8), 2201-2220.

Holmberg, S., Ghazinejad, M., Cho, E., George, D., Pollack, B., Perebikovsky, A., . . . Madou, M. (2018). Stress-activated pyrolytic carbon nanofibers for electrochemical platforms. *Electrochimica Acta, 290*, 639-648.

Huang, Y., Dong, X., Liu, Y., Li, L.-J., & Chen, P. (2011). Graphene-based biosensors for detection of bacteria and their metabolic activities. *Journal of Materials Chemistry, 21*(33), 12358-12362.

Janata, J. í. (2009). Conductometric Sensors *Principles of Chemical Sensors* (pp. 241-266). Boston, MA: Springer US.

Joshi, R., Janagama, H., Dwivedi, H. P., Kumar, T. S., Jaykus, L.-A., Schefers, J., & Sreevatsan, S. (2009). Selection, characterization, and application of DNA aptamers for the capture and detection of *Salmonella enterica* serovars. *Molecular and Cellular Probes, 23*(1), 20-28.

Juhasz, R., Elfström, N., & Linnros, J. (2005). Controlled fabrication of silicon nanowires by electron beam lithography and electrochemical size reduction. *Nano letters, 5*(2), 275-280.

Kaisti, M. (2017). Detection principles of biological and chemical FET sensors. *Biosensors and Bioelectronics, 98*, 437-448.

Kamath, R. R., & Madou, M. J. (2014). Three-dimensional carbon interdigitated electrode arrays for redox-amplification. *Analytical Chemistry, 86*(6), 2963-2971.

Kessick, R., Fenn, J., & Tepper, G. (2004). The use of AC potentials in electrospraying and electrospinning processes. *Polymer, 45*(9), 2981-2984.

Kim, J., Song, X., Kinoshita, K., Madou, M., & White, R. (1998). Electrochemical studies of carbon films from pyrolyzed photoresist. *Journal of the Electrochemical Society, 145*(7), 2314-2319.

Komuro, A., Matsuyuki, S., & Ando, A. (2018). Comparison of simulations and experiments on the axial distributions of the electron density in a point-to-plane streamer discharge at atmospheric pressure. *Journal of Physics D-Applied Physics, 51*(44), 445204.

Kwan, Y. C. G., Ng, G. M., & Huan, C. H. A. (2015). Identification of functional groups and determination of carboxyl formation temperature in graphene oxide using the XPS O 1s spectrum. *Thin Solid Films, 590*, 40-48.

University of Malaya

Lai, C.-C., & Lo, C.-T. (2015). Plasma oxidation of electrospun carbon nanofibers as supercapacitor electrodes. *RSC Advances, 5*(49), 38868-38872.

Lee, K.-M., Runyon, M., Herrman, T. J., Phillips, R., & Hsieh, J. (2015). Review of Salmonella detection and identification methods: Aspects of rapid emergency response and food safety. *Food control, 47*, 264-276.

Lee, S. W., Liang, D., Gao, X. P. A., & Sankaran, R. M. (2011). Direct Writing of Metal Nanoparticles by Localized Plasma Electrochemical Reduction of Metal Cations in Polymer Films. *Advanced Functional Materials, 21*(11), 2155-2161.

Li, L.-x., & Li, F. (2011). The effect of carbonyl, carboxyl and hydroxyl groups on the capacitance of carbon nanotubes. *New Carbon Materials, 26*(3), 224-228.

Li, W. J., Laurencin, C. T., Caterson, E. J., Tuan, R. S., & Ko, F. K. (2002). Electrospun nanofibrous structure: a novel scaffold for tissue engineering. *Journal of Biomedical Materials Research Part A, 60*(4), 613-621.

Lim, Y., Heo, J.-I., Madou, M., & Shin, H. (2013). Monolithic carbon structures including suspended single nanowires and nanomeshes as a sensor platform. *Nanoscale research letters8*, 492.

Lim, Y., Heo, J., Madou, M. J., & Shin, H. (2013, 16-20 June 2013). *Development of suspended 2D carbon nanostructures: Nanowires to nanomeshes.* Paper presented at the 2013 Transducers & Eurosensors XXVII: The 17th International Conference on Solid-State Sensors, Actuators and Microsystems (TRANSDUCERS & EUROSENSORS XXVII).

Lin, C.-C., & Liao, J.-Y. (2011). Fabrication and Plasma Treatment of Carbon Nanotubes on Sputtered Cobalt for Electrodes of Electrochemical Capacitors. *Electrochemistry, 79*(1), 10-14.

Lin, L., & Wang, Q. (2015). Microplasma: A New Generation of Technology for Functional Nanomaterial Synthesis. *Plasma chemistry and plasma processing, 35*(6), 925-962.

Lin, M., Hu, X., Ma, Z., & Chen, L. (2012). Functionalized polypyrrole nanotube arrays as electrochemical biosensor for the determination of copper ions. *Analytica Chimica Acta, 746*, 63-69.

Long, J. W., Dunn, B., Rolison, D. R., & White, H. S. (2004). Three-dimensional battery architectures. *Chemical Reviews, 104*(10), 4463-4492.

Maciorowski, K. G., Herrera, P., Jones, F. T., Pillai, S. D., & Ricke, S. C. (2006). Cultural and Immunological Detection Methods for Salmonella spp. in Animal Feeds – A Review. *Veterinary Research Communications, 30*(2), 127-137. doi:10.1007/s11259-006-3221-8

Malladi, K., Wang, C., & Madou, M. (2006). Fabrication of suspended carbon microstructures by e-beam writer and pyrolysis. *Carbon, 44*(13), 2602-2607.

University of Malaya

Manuelli, A., Persano, L., & Pisignano, D. (2014). Flexible organic field-effect transistors based on electrospun conjugated polymer nanofibers with high bending stability. *Organic Electronics, 15*(5), 1056-1061.

Mardegan, A., Kamath, R., Sharma, S., Scopece, P., Ugo, P., & Madou, M. (2013). Optimization of carbon electrodes derived from epoxy-based photoresist. *Journal of the Electrochemical Society, 160*(8), B132-B137.

Martinez-Duarte, R. (2014). SU-8 Photolithography as a Toolbox for Carbon MEMS. *Micromachines, 5*(3), 766-782.

Meng, C., Xiao, Y., Wang, P., Zhang, L., Liu, Y., & Tong, L. (2011). Quantum‐Dot‐Doped Polymer Nanofibers for Optical Sensing. *Advanced Materials, 23*(33), 3770-3774.

Merenda, A., Ligneris, E. d., Sears, K., Chaffraix, T., Magniez, K., Cornu, D., . . . Dumée, L. F. (2016). Assessing the temporal stability of surface functional groups introduced by plasma treatments on the outer shells of carbon nanotubes. *Scientific Reports, 6*, 31565.

Merrill, F. H., & Hippel, A. V. (1939). The Atomphysical Interpretation of Lichtenberg Figures and Their Application to the Study of Gas Discharge Phenomena. *Journal of Applied physics, 10*(12), 873-887.

Min, S.-Y., Kim, T.-S., Kim, B. J., Cho, H., Noh, Y.-Y., Yang, H., . . . Lee, T.-W. (2013). Large-scale organic nanowire lithography and electronics. *Nature communications, 4*, 1773.

Mohanty, N., & Berry, V. (2008). Graphene-based single-bacterium resolution biodevice and DNA transistor: interfacing graphene derivatives with nanoscale and microscale biocomponents. *Nano letters, 8*(12), 4469-4476.

Mortensen, H., Kusano, Y., Leipold, F., Rozlosnik, N., Kingshott, P., Goutianos, S., . . . Bindslev, H. (2006). Modification of Glassy Carbon Surfaces by Atmospheric Pressure Cold Plasma Torch. *Japanese Journal of Applied Physics, 45*(10B), 8506-8511.

Muniandy, S., Dinshaw, I. J., Teh, S. J., Lai, C. W., Ibrahim, F., Thong, K. L., & Leo, B. F. (2017). Graphene-based label-free electrochemical aptasensor for rapid and sensitive detection of foodborne pathogen. *Analytical and Bioanalytical Chemistry*, 1-13.

Nakamura, K., Koizumi, H., Nakano, M., & Takao, Y. (2019). Effects of negative ions on discharge characteristics of water plasma source for a miniature microwave discharge ion thruster. *Physics of Plasmas, 26*(4), 043508.

Oda, H., Yamashita, A., Minoura, S., Okamoto, M., & Morimoto, T. (2006). Modification of the oxygen-containing functional group on activated carbon fiber in electrodes of an electric double-layer capacitor. *Journal of Power Sources, 158*(2), 1510-1516.

University of Malaya

Oh, S. J., Park, B. H., Jung, J. H., Choi, G., Lee, D. C., & Seo, T. S. (2016). Centrifugal loop-mediated isothermal amplification microdevice for rapid, multiplex and colorimetric foodborne pathogen detection. *Biosensors and Bioelectronics, 75*, 293-300.

Park, B. Y., Taherabadi, L., Wang, C., Zoval, J., & Madou, M. J. (2005). Electrical properties and shrinkage of carbonized photoresist films and the implications for carbon microelectromechanical systems devices in conductive media. *Journal of the Electrochemical Society, 152*(12), J136-J143.

Park, S. K., Mahmood, Q., & Park, H. S. (2013). Surface functional groups of carbon nanotubes to manipulate capacitive behaviors. *Nanoscale, 5*(24), 12304-12309.

Pasakon, P., Mensing, J. P., Phokaratkul, D., Karuwan, C., Lomas, T., Wisitsoraat, A., & Tuantranont, A. (2019). A high-performance, disposable screen-printed carbon electrode modified with multi-walled carbon nanotubes/graphene for ultratrace level electrochemical sensors. *Journal of Applied Electrochemistry, 49*(2), 217-227.

Paul K, B., Panigrahi, A. K., Singh, V., & Singh, S. G. (2017). A multi-walled carbon nanotube–zinc oxide nanofiber based flexible chemiresistive biosensor for malaria biomarker detection. *Analyst, 142*(12), 2128-2135.

Peng, L.-M., Zhang, Z., & Qiu, C. (2019). Carbon nanotube digital electronics. *Nature Electronics, 2*(11), 499-505. doi:10.1038/s41928-019-0330-2

Peng, L.-M., Zhang, Z., & Wang, S. (2014). Carbon nanotube electronics: recent advances. *Materials Today, 17*(9), 433-442.

Penmatsa, V., Rahim, R. A., Kawarada, H., & Wang, C. (2015). Functionalized carbon microarrays platform for high sensitive detection of HIV-Tat peptide. *RSC Advances, 5*(80), 65042-65047. doi:10.1039/C5RA10214F

Pham, V. B., Pham, X. T. T., Dang, N. T. D., Le, T. T. T., Tran, P. D., Nguyen, T. C., . . . Tong, D. H. (2011). Detection of DNA of genetically modified maize by a silicon nanowire field-effect transistor. *Advances in Natural Sciences: Nanoscience and Nanotechnology, 2*(2), 025010.

Prakash, M. D., Vanjari, S. R. K., Sharma, C. S., & Singh, S. G. (2016). Ultrasensitive, Label Free, Chemiresistive Nanobiosensor Using Multiwalled Carbon Nanotubes Embedded Electrospun SU-8 Nanofibers. *Sensors, 16*(9), 1354.

Pramanick, B., Ibrahim, F., & Thiha, A. (2016). Carbon Nanowire Fabrication: C-MEMS. In M. J. Madou, V. H. Perez-Gonazalez, & B. Pramanick (Eds.), *Carbon: The Next Silicon* (Vol. 1, pp. 151-170). New York: Momentum Press.

Qiu, W., Xu, H., Takalkar, S., Gurung, A. S., Liu, B., Zheng, Y., . . . Liu, G. (2015). Carbon nanotube-based lateral flow biosensor for sensitive and rapid detection of DNA sequence. *Biosensors and Bioelectronics, 64*, 367-372.

Rajesh, Sharma, V., Puri, N. K., Singh, R. K., Biradar, A. M., & Mulchanadani, A. (2013). Label-free detection of cardiac troponin-I using gold nanoparticles functionalized

University of Malaya

single-walled carbon nanotubes based chemiresistive biosensor. *Applied Physics Letters, 103*(20), 203703.

Ramakrishna, S., Fujihara, K., Teo, W.-E., Lim, T.-C., & Ma, Z. (2005). *An introduction to electrospinning and nanofibers* (Vol. 90): World Scientific.

Ranganathan, S., Mccreery, R., Majji, S. M., & Madou, M. (2000). Photoresist ‐ derived carbon for microelectromechanical systems and electrochemical applications. *Journal of the Electrochemical Society, 147*(1), 277-282.

Reneker, D. H., & Yarin, A. L. (2008). Electrospinning jets and polymer nanofibers. *Polymer, 49*(10), 2387-2425.

Reneker, D. H., Yarin, A. L., Fong, H., & Koombhongse, S. (2000). Bending instability of electrically charged liquid jets of polymer solutions in electrospinning. *Journal of Applied physics, 87*(9), 4531-4547.

Rożek, Z., Kaczorowski, W., Lukáš, D., Louda, P., & Mitura, S. (2008). Potential applications of nanofiber textile covered by carbon coatings. *Journal of Achievements in Materials and Manufacturing Engineering, 27*(1), 35-38.

Salazar, A., Cardenas-Benitez, B., Pramanick, B., Madou, M. J., & Martinez-Chapa, S. O. (2017). Nanogap fabrication by Joule heating of electromechanically spun suspended carbon nanofibers. *Carbon, 115*, 811-818.

Sayad, A., Ibrahim, F., Mukim Uddin, S., Cho, J., Madou, M., & Thong, K. L. (2018). A microdevice for rapid, monoplex and colorimetric detection of foodborne pathogens using a centrifugal microfluidic platform. *Biosensors and Bioelectronics, 100*, 96-104.

Schueller, O. J., Brittain, S. T., & Whitesides, G. M. (1997). Fabrication of glassy carbon microstructures by pyrolysis of microfabricated polymeric precursors. *Advanced Materials, 9*(6), 477-480.

Sharma, C. S., Katepalli, H., Sharma, A., & Madou, M. (2011). Fabrication and electrical conductivity of suspended carbon nanofiber arrays. *Carbon, 49*(5), 1727-1732.

Sharma, S. (2013). *Microstructural Tuning of Glassy Carbon for Electrical and Electrochemical Sensor Applications*.

Sharma, S., & Madou, M. (2012). A new approach to gas sensing with nanotechnology. *Philosophical Transactions of the Royal Society A: Mathematical, Physical and Engineering Sciences, 370*(1967), 2448-2473.

Sharma, S., Sharma, A., Cho, Y.-K., & Madou, M. (2012). Increased Graphitization in Electrospun Single Suspended Carbon Nanowires Integrated with Carbon-MEMS and Carbon-NEMS Platforms. *ACS Applied Materials & Interfaces, 4*(1), 34-39.

Sharma, S., Shyam Kumar, C. N., Korvink, J. G., & Kübel, C. (2018). Evolution of Glassy Carbon Microstructure: In Situ Transmission Electron Microscopy of the Pyrolysis Process. *Scientific Reports, 8*(1), 16282. doi:10.1038/s41598-018-34644-9

University of Malaya

Shimizu, K., Fukunaga, H., Tatematsu, S., & Blajan, M. (2012). Atmospheric microplasma application for surface modification of biomaterials. *Japanese Journal of Applied Physics, 51*(11S), 11PJ01.

Shulaker, M. M., Hills, G., Patil, N., Wei, H., Chen, H.-Y., Wong, H.-S. P., & Mitra, S. (2013). Carbon nanotube computer. *Nature, 501*(7468), 526-530.

Simon, I., Bârsan, N., Bauer, M., & Weimar, U. (2001). Micromachined metal oxide gas sensors: opportunities to improve sensor performance. *Sensors and Actuators B: Chemical, 73*(1), 1-26.

Singh, A., Jayaram, J., Madou, M., & Akbar, S. (2002). Pyrolysis of negative photoresists to fabricate carbon structures for microelectromechanical systems and electrochemical applications. *Journal of the Electrochemical Society, 149*(3), E78-E83.

Smyth, H., & Mueller, D. (1933). The ionization of water vapor by electron impact. *Physical Review, 43*(2), 116.

Spain, E., McCooey, A., Joyce, K., Keyes, T. E., & Forster, R. J. (2015). Gold nanowires and nanotubes for high sensitivity detection of pathogen DNA. *Sensors and Actuators B: Chemical, 215*, 159-165.

Stankus, J. J., Guan, J., & Wagner, W. R. (2004). Fabrication of biodegradable elastomeric scaffolds with sub-micron morphologies. *Journal of Biomedical Materials Research Part A, 70A*(4), 603-614. doi:10.1002/jbm.a.30122

Sun, D., Chang, C., Li, S., & Lin, L. (2006). Near-Field Electrospinning. *Nano letters, 6*(4), 839-842.

Tan, X., Shi, T., Lin, J., Sun, B., Tang, Z., & Liao, G. (2018). One-Step Mask-Based Diffraction Lithography for the Fabrication of 3D Suspended Structures. *Nanoscale research letters, 13*(1), 394-394. doi:10.1186/s11671-018-2817-6

Taylor, G. (1964). *Disintegration of water drops in an electric field.* Paper presented at the Proceedings of the Royal Society of London A: Mathematical, Physical and Engineering Sciences.

Taylor, G. (1969). Electrically driven jets. *Proceedings of the Royal Society of London. A. Mathematical and Physical Sciences, 313*(1515), 453-475.

Teh, W., Duerig, U., Drechsler, U., Smith, C., & Guentherodt, H. J. (2005). Effect of low numerical-aperture femtosecond two-photon absorption on (SU-8) resist for ultrahigh-aspect-ratio microstereolithography. *Journal of Applied physics, 97*. doi:10.1063/1.1856214

Theron, A., Zussman, E., & Yarin, A. (2001). Electrostatic field-assisted alignment of electrospun nanofibres. *Nanotechnology, 12*(3), 384.

Villamizar, R. A., Maroto, A., Rius, F. X., Inza, I., & Figueras, M. J. (2008). Fast detection of *Salmonella* Infantis with carbon nanotube field effect transistors. *Biosensors and Bioelectronics, 24*(2), 279-283.

University of Malaya

Viswanadam, G., & Chase, G. G. (2013). Modified electric fields to control the direction of electrospinning jets. *Polymer, 54*(4), 1397-1404.

Wan, Y. Q., He, J. H., Yu, J. Y., & Wu, Y. (2007). Electrospinning of high‐molecule PEO solution. *Journal of applied polymer science, 103*(6), 3840-3843.

Wang, B., Lu, G., Luo, Q.-P., & Wang, T. (2016). Free-Standing Porous Carbon Nanofiber Networks from Electrospinning Polyimide for Supercapacitors. *Journal of Nanomaterials, 2016*, 7. doi:10.1155/2016/4305437

Wang, C., Jia, G., Taherabadi, L. H., & Madou, M. J. (2005). A novel method for the fabrication of high-aspect ratio C-MEMS structures. *Journal of microelectromechanical systems, 14*(2), 348-358.

Wang, C., & Madou, M. (2005). From MEMS to NEMS with carbon. *Biosensors and Bioelectronics, 20*(10), 2181-2187.

Wang, C., Taherabadi, L., Jia, G., Kassegne, S., Zoval, J., & Madou, M. (2004). Carbon-MEMS architectures for 3D microbatteries. *Proceedings of SPIE - The International Society for Optical Engineering, 5455*. doi:10.1117/12.548755

Wang, C., Yin, L., Zhang, L., Xiang, D., & Gao, R. (2010). Metal Oxide Gas Sensors: Sensitivity and Influencing Factors. *Sensors, 10*(3), 2088-2106.

Wang, C., Zaouk, R., & Madou, M. (2006). Local chemical vapor deposition of carbon nanofibers from photoresist. *Carbon, 44*(14), 3073-3077.

Wang, L., Li, Y., & Mustapha, A. (2007). Rapid and simultaneous quantitation of *Escherichia coli* O157: H7, *Salmonella*, and *Shigella* in ground beef by multiplex real-time PCR and immunomagnetic separation. *Journal of food protection, 70*(6), 1366-1372.

Wang, S. C., Chang, K. S., & Yuan, C. J. (2009). Enhancement of electrochemical properties of screen-printed carbon electrodes by oxygen plasma treatment. *Electrochimica Acta, 54*(21), 4937-4943.

Wang, S. Q., He, J. H., & Xu, L. (2008). Non‐ionic surfactants for enhancing electrospinability and for the preparation of electrospun nanofibers. *Polymer International, 57*(9), 1079-1082.

Wang, X., Carey, W. P., & Yee, S. S. (1995). Monolithic thin-film metal-oxide gas-sensor arrays with application to monitoring of organic vapors. *Sensors and Actuators B: Chemical, 28*(1), 63-70.

Wang, X., Yin, Y., Hao, C., & You, Z. (2015). A high-performance three-dimensional micro supercapacitor based on ripple-like ruthenium oxide–carbon nanotube composite films. *Carbon, 82*, 436-445.

Wannatong, L., Sirivat, A., & Supaphol, P. (2004). Effects of solvents on electrospun polymeric fibers: preliminary study on polystyrene. *Polymer International, 53*(11), 1851-1859.

University of Malaya

Wormeester, G., Pancheshnyi, S., Luque, A., Nijdam, S., & Ebert, U. (2010). Probing photo-ionization: simulations of positive streamers in varying N2 : O2-mixtures. *Journal of Physics D: Applied Physics, 43*(50), 505201.

Wu, S., Cheng, W., Huang, G., Wu, F., Liu, C., Liu, X., . . . Lu, X. (2018). Positive streamer corona, single filament, transient glow, dc glow, spark, and their transitions in atmospheric air. *Physics of Plasmas, 25*(12), 123507.

Wu, Y., Lin, X., & Zhang, M. (2013). Carbon Nanotubes for Thin Film Transistor: Fabrication, Properties, and Applications. *Journal of Nanomaterials, 2013*, 627215. doi:10.1155/2013/627215

Xiong, D., Li, X., Shan, H., Zhao, Y., Dong, L., Xu, H., . . . Sun, X. (2015). Oxygen-containing Functional Groups Enhancing Electrochemical Performance of Porous Reduced Graphene Oxide Cathode in Lithium Ion Batteries. *Electrochimica Acta, 174*, 762-769.

Xu, C., Shi, X., Ji, A., Shi, L., Zhou, C., & Cui, Y. (2015). Fabrication and characteristics of reduced graphene oxide produced with different green reductants. *PloS one, 10*(12), e0144842.

Yang, W., Ratinac, K. R., Ringer, S. P., Thordarson, P., Gooding, J. J., & Braet, F. (2010). Carbon nanomaterials in biosensors: should you use nanotubes or graphene? *Angewandte Chemie International Edition, 49*(12), 2114-2138.

Yue, Z. R., Jiang, W., Wang, L., Gardner, S. D., & Pittman, C. U. (1999). Surface characterization of electrochemically oxidized carbon fibers. *Carbon, 37*(11), 1785-1796.

Zhang, J., Xu, Y., Liu, Z., Yang, W., & Liu, J. (2015). Highly conductive porous graphene electrode prepared via in-situ reduction of graphene oxide using Cu nanoparticles for the fabrication of high performance supercapacitor. *RSC Advances, 5*(67).

Zhang, Y., He, X., Li, J., Miao, Z., & Huang, F. (2008). Fabrication and ethanol-sensing properties of micro gas sensor based on electrospun SnO< sub> 2</sub> nanofibers. *Sensors and Actuators B: Chemical, 132*(1), 67-73.

Zhou, F.-L., Hubbard, P. L., Eichhorn, S. J., & Parker, G. J. (2011). Jet deposition in near-field electrospinning of patterned polycaprolactone and sugar-polycaprolactone core–shell fibres. *Polymer, 52*(16), 3603-3610.

Zhou, W., Huang, P.-J. J., Ding, J., & Liu, J. (2014). Aptamer-based biosensors for biomedical diagnostics. *Analyst, 139*(11), 2627-2640.

Zhou, Z., Wu, X.-F., & Fong, H. (2012). Electrospun carbon nanofibers surface-grafted with vapor-grown carbon nanotubes as hierarchical electrodes for supercapacitors. *Applied Physics Letters, 100*(2), 023115.

Zhuang, X., Tian, C., Luan, F., Wu, X., & Chen, L. (2016). One-step electrochemical fabrication of a nickel oxide nanoparticle/polyaniline nanowire/graphene oxide hybrid on a glassy carbon electrode for use as a non-enzymatic glucose biosensor. *RSC Advances, 6*(95), 92541-92546. doi:10.1039/C6RA14970G

University of Malaya

LIST OF PUBLICATIONS AND PAPERS PRESENTED

Journal Articles

Thiha, A., Ibrahim, F., Muniandy, S., Dinshaw, I. J., Teh, S.J., Thong, K.W., Leo, B.F. & Madou, M.J. (2018). Facile fabrication of all-carbon suspended nanowire sensors as a rapid highly-sensitive label-free chemiresistive biosensing platform. Biosensors and Bioelectronics. 107, 145-152.

Thiha, A., Ibrahim, F., Muniandy, S., & Madou, M. J. (2019). Microplasma direct writing for site-selective surface functionalization of carbon microelectrodes. Microsystems & nanoengineering, 5(1), 1-12.

Proceeding

Thiha, A., Ibrahim, F., Abd Hamid S. B. & Madou M. (2016). A new approach for selective surface functionalization of carbon electrodes in biosensing by plasma direct-writing. ECS Transactions, 72 (1) 51-57.

Chapter in Book

Pramanick, B., Ibrahim, F. & **Thiha, A.** (2015). Carbon Nanowire Fabrication: C-MEMS. In: M. J. Madou, V. H. Perez-Gonzalez, B. Pramanick, eds. Carbon: The Next Silicon? New York: Momentum Press. 151-170. ISBN: 1606507230.

Conference presentation

Thiha, A., Ibrahim, F., Abd Hamid S. B. & Madou M. (2016). Plasma direct-writing as a mean for selective surface functionalization of carbon electrodes in biosensing. 229th Electrochemical Society Meeting. San Diego, USA. May 29- June 2, 2016.

Patent

Ibrahim, F., Teh, S.J., Thong, K.W., **Thiha, A**., Leo, B.F., Muniandy, S. & Dinshaw, I.J., (2018) Device for rapid detection of *Salmonella* bacteria, a method of fabrication, and operating thereof. 2018002651. (Patent filed, Dec 2018)

University of Malaya